OPTICAL PROPERTIES AND EXCITATION

DYNAMICS IN 3D AND 2D SYSTEMS

CHEN JIANQIANG

NATIONAL UNIVERSITY OF SINGAPORE

2013

OPTICAL PROPERTIES AND EXCITATION

DYNAMICS IN 3D AND 2D SYSTEMS

CHEN JIANQIANG

(*M.Sc*, NATIONAL UNIVERSITY OF SINGAPORE,

SINGAPORE)

A THESIS SUBMITTED

FOR THE DEGREE OF DOCTOR OF PHILOSOPHY

DEPARTMENT OF ELECTRICAL AND COMPUTER

ENGINEERING

NATIONAL UNIVERSITY OF SINGAPORE

2013

Thesis Declaration

I hereby declare that the thesis is my original work and it has been written by me in its entirety. I have duly acknowledged all the sources of information which have been used in the thesis.

This thesis has also not been submitted for any degree in any university previously.

Chen Jianqiang

14 Auguest 2013

ACKNOWLEDGEMENTS

Over the last four years, many people have help and support me during my Ph.D. study. It would not have been possible to finish this doctoral thesis without the help and support of all kind people around me, to only some of whom it is possible to give particular mention here.

I would like to express my sincere gratitude to my supervisor, Prof. Venky Venkatesan for his support, encouragement, and guidance throughout the course. He has exposed me to a whole new world of research and encouraged me in all my efforts and endeavors. Prof. Venkatesan has always made himself available, patiently resolved my doubts, and imparted considerable knowledge and deep insights whenever I have sought his help. It has been a great honor and privilege for me to work under his supervision through these past four years. I will always cherish these precious working experience with him and all that he has taught me.

I would also like to express my warm and sincere thanks to my supervisor, Prof. Xu, Qing-Hua, for his patient guidance and fruitful suggestions. Prof. Xu has provided me with many opportunities, encouraged me to perform ultrafast optical spectroscopy experiments, and granted me complete freedom to use all the facilities in his lab. Without his support, I do not believe that I would have gained the expertise I possess in the field of optics today.

I should specially thank Dr. Bao Qiaoliang, Dr. You Guanjun, Dr. Xing Guichuan, Dr. Lu Weiming, Dr. Zhen Huang, and Dr. Sankar Dhar, for their patient listening and generous discussions and assistance.

I want to thank Profs. Ariando and A. Rusydi for their tremendous help with

TABLE OF CONTENTS

SUMMARY

This thesis reports the linear and nonlinear optical properties and carrier excitation dynamics in three-dimensional (bulk oxide semiconductor crystals) and two-dimensional (oxide films and graphene) systems. An ultrafast femtosecond laser is used to study the linear and nonlinear optical properties as well as the carrier dynamics of oxide materials (both bulk crystal and pulsed laser deposited films). A single model continuous wave laser is used to study the optical bistability properties of graphene in a Fabry–Perot cavity.

This project starts with a study of the photoluminescence of single-crystal $LaAlO_3$, in which the defect levels within the band gap produce a strong emission spectrum. We then use transient absorption technique to identify these defects levels. Furthermore, the nonradiative carrier relaxation process of these defect levels has also been studied. Through photoluminescence and transient absorption studies, we have mapped these defect levels in the $LaAlO_3$ system.

Then, we continue this study with $SrTiO_3$, which has many physical properties similar to those of $LaAlO_3$. In this case, the strong photoluminescence of $SrTiO_3$ using multi-photon excitation has been obtained at room temperature. In addition, with a combination of above band gap, sub band gap and band edge excitation, the defect states (with their carrier relaxation lifetimes) within the band gap of $SrTiO_3$ have been studied.

From a previous photoluminescence and transient absorption study of $LaAlO_3$ and $SrTiO_3$, we found that the defect levels strongly influence the optical properties of these materials. Then, we studied the effect of manipulating the defect level population. This was demonstrated in the TiO_2 system, where the

defects states were manipulated by two methods: by annealing the film under different oxygen pressures and by electron doping (Ta-substituted TiO_2). It is easier to manipulate the defect in the films; therefore, we have prepared TiO_2 films (with different oxygen vacancies and Ta substitution concentrations) by pulsed laser deposition. It is shown that the lifetime of the defect states (most of which are due to oxygen vacancies) decrease with increase the oxygen vacancies or Ta concentration.

The fruitful results of two-dimensional TiO_2 films led us to continue this study for other two-dimensional materials. Graphene is considered as one of the most important two-dimensional materials, and it has already been demonstrated to show very interesting optical properties. Therefore, we studied the optical properties of graphene. As graphene shows rich nonlinear optical properties such as saturable absorption and giant Kerr nonlinearity, we focused our study on the nonlinear optical applications of graphene. Optical bistability has been demonstrated by placing monolayer graphene into a Fabry–Perot cavity. A clear bistability hysteresis loop was observed in monolayer graphene.

To summarize, this study from the linear to the nonlinear optical viewpoint, investigates the defect carrier dynamics of various oxide materials. Furthermore, the nonlinear optical applications of graphene have been demonstrated through an optical bistability experiment. This study could contribute towards the investigation of materials (oxides and graphene) for realizing faster, smaller, and thinner nanoelectronic, optoelectronics and integrated photonics devices.

LIST OF PUBLICATIONS

1. **J. Q. Chen**, X. Wang, Y. H. Lu, A. R. Barman, S. Dhar, Y. P. Feng, Ariando, Q. -H. Xu, T. Venkatesan, "Defect Dynamics and Spectral Observation of Twinning in Single Crystalline LaAlO3 under Sub-Bandgap Excitation", **Appl. Phys. Lett,** 2011, 98, 041904.

2. X. Wang, **J. Q. Chen**, A. Barman, S. Dhar, Q. -H. Xu, T. Venkatesan, Ariando, "Static and Ultrafast Dynamics of Defects of SrTiO3 in LaAlO3/SrTiO3 Heterostructures", **Appl. Phys. Lett,** 2011, 98, 081916.

3. **J. Q. Chen**, Q. -H. Xu, and T. Venkatesan, "Defect dynamic of the Pulsed Laser Deposition Prepared TiO2 films", (Submitted)

4. Q. L. Bao*****, **J. Q. Chen***, Y. J. Xiang, K. Zhang, S. J. Li, X. F. Jiang, Q. -H. Xu, K. P. Loh and T. Venkatesan " Graphene Nanobubble: A New Optical Nonlinear Material ", (Submitted) **(*Equal Contribution)**

5. **J. Q. Chen**, X. F. Jiang, X. Wang, G. J. You, G. C. Xing, T. C. Sum, S. Dhar, Ariando, Q. -H. Xu, and T. Venkatesan " Dynamics of Defect States in $SrTiO_3$ Revealed by Photoluminescence and Femtosecond Transient Absorption Using Sub-bandgap Excitation ", Ready to Submit

6. **J. Q. Chen**, Y. L. Zhao, N. Mueller, A. Rusydi, Q. -H. Xu, and T. Venkatesan, "Defect dynamic of the $Ta_xTi_{1-x}O_2$ films", (Manuscript in preparation)

LIST OF FIGURES

LIST OF SYMBOLS

R	Resistance	H	Magnetic field
ρ	Resistivity	K	Kelvin
R_s	Sheet resistance	t	Time
σ	Conductivity	V	Voltage
T	Temperature	I	Current
B	Magnetic field	H_c	Coercivity
M	Magnetic moment	μ	Mobility
E_g	Energy band gap	μ_B	Bohr magneton
e	Electronic charge	TiO_2	Titanium dioxide
n	Electron carrier density	PLD	Pulse laser deposition
XRD	X-ray diffraction	UV-vis	Ultraviolet-visible
NIR	Near-infread	LTO	$LaTiO_3$
MR	Magnetoresistance	YBCO	$YBa_2Cu_3O_7$
LAO	$LaAlO_3$	STO	$SrTiO_3$

TA   Transient absorption

TPA   Two photon absorption

TCSPC   Time-correlated single photon counting

2DEG   Two dimensional electron gas

TRPES   Time-resolved photoelectron spectroscopy

AFM   Atomic force microscopy

CVD   Chemical vapor deposition

PMMA   Poly methyl methacrylate

FDTD   Finite-difference time-domain

Chapter 1   Introduction

1.1 Introduction

Semiconductor technology is almost half a century old and the speed of semiconductor chips has grown exponentially according to the Moore's law.[1] The demand for smaller, faster, and more functional chips is expected to rise in the future. However, as device sizes have reduced to the nanometer scale, semiconductor devices have reached the threshold where quantum effects become important and they pose a challenge to scaling down. The hybridization of silicon with other functional materials is expected to grow, leading to increased functionality in chips in addition to speed and reduced size. To meet the demands of technology, new classes of materials with potential semiconductor applications are being investigated.

Recently, complex oxide materials have attracted great interest. Many intriguing physical properties have been observed in these materials, such as high temperature superconductivity, resistivity switching and colossal magnetoresistance (MR).[2-4] Furthermore, with developments in material synthesis technology, device sizes of nanometer scales are being achieved.

In 2002, a high-mobility conducting two-dimensional electron gas (2DEG) at the interface of the two insulators, $LaTiO_3$ (LTO) and $SrTiO_3$ (STO), was reported by Ohtomo and Hwang.[5] This observation attracted significant research of these materials. Numerous studies have thoroughly investigated the electronic, magnetic and optical properties as well as the structures of these oxide materials both in bulk crystals and in heterostructures.[6-13] Superconductivity, ferromagnetism, diamagnetism and paramagnetism have

been observed at these interfaces.[14-18] However, the linear and nonlinear optical properties, such as the multiphoton photoluminescence (PL), transient absorption (TA), pump-probe, and defect carrier dynamics, have not been studied adequately in this system.

Besides this 2DEG in Oxide materials, Graphene is another 2DEG system which has shown great potential for high speed electronic devices. This single-atom-thick carbon atom material shows ultrafast electronic transport properties compared to semiconductors, making it ideally suited for nanometer scale high-speed devices. Indeed Graphene has also been used for optoelectronic applications, especially for nonlinear optics due to its easily-achievable saturable absorption and giant Kerr nonlinearity, which are both essential properties for digital optics based on nonlinear resonators.[19-21] In this study, we demonstrate optical bistability of monolayer graphene in a Fabry–Perot cavity.

In this study, an ultrafast femtosecond laser was used to investigate the linear and nonlinear optical properties of the 3D oxide crystals and a modulated cw laser was used to investigate the nonlinearity in a 2D graphene sheet inside a Fabry Perot resonator. Furthermore, ultrafast spectroscopy analysis of the carrier dynamics of the oxide materials was conducted in the sub-picosecond range. This chapter introduces the general physical properties of the studied oxide materials and the nonlinear optical properties of graphene. The outline of this thesis is presented at the end of this chapter.

1.2 Perovskite oxide

Oxide semiconductors are one of the most important materials in oxide electronics applications. Oxide semiconductor materials have a wide band gap,

and therefore, they may potentially find applications in transparent conducting electronic devices.

The perovskite structure, with a typical chemical formula of ABX_3, is one type of complex oxide material, an example of which is STO. Perovskite was discovered by Gustav Rose and is named after the Russian mineralogist L. A. Perovski (1792–1856).[22]

Perovskite oxide has a cubic or pseudo cubic crystal structure. The cation "A" is generally larger than cation "B," and it is connected to an anion X (generally oxygen). The material has cubic-symmetry structure, where the "B" cation shows 6-fold coordination and is surrounded by an octahedron of "X" anions, and the "A" cation shows 12-fold coordination. The schematic structure of the perovskite crystal is shown in Fig. 1.1, where the light blue spheres indicate "A" cations; the black ones, "B" cations; and the red ones, oxygen.

Perovskite oxides show many interesting and unique properties, such as colossal magnetoresistance, spin-dependent transport, charge ordering, and high-temperature superconductivity. As a result, they have been widely applied to make sensors, catalyst electrodes, and electronic devices.[9,23] In this thesis, two important perovskite oxides—$LaAlO_3$ (LAO) and STO—are studied. These two material systems are introduced.
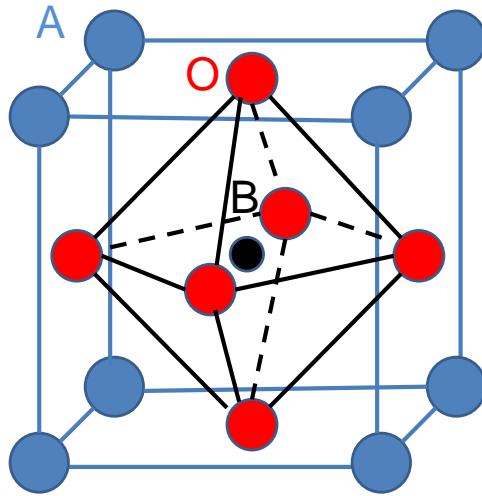
Figure 1. 1. Schematic of perovskite structure.

1.3 Fundamental properties of LaAlO$_3$

LAO is a perovskite-type oxide material with a rhombohedral unit cell.[24] As a result of its large bandgap of 5.6 eV, LAO is transparent in a wide optical range, making it an attractive material for optical applications.[25] Furthermore, owing to its high dielectric constant and low RF/ microwave loss, LAO has been widely used in infrared and microwave devices, where its use enables low tunneling leakage current to be achieved.[26,27] LAO has a lattice constant of 3.791 Å.[28] This lattice constant matches many oxide materials, making LAO as an important substrate for oxide deposition; for example, YBa$_2$Cu$_3$O$_7$ (YBCO), STO and TiO$_2$ can be epitaxially grown on LAO substrate with high quality.[2,29]

At room temperature, LAO has a rhombohedral phase; this structure transforms into a cubic phase at a high temperature near 875 K.[30,31] This phase transition results in twin formation, which is commonly observed in a

lower symmetry structure phase transition system. The lattice phase transition from cubic to rhombohedral causes a lattice distortion that results in the formation of both (100) and (110) twins in the LAO crystal.[32,33] It has been reported that the (100) twin is predominant in LAO single crystals.[34,35]

This lattice distortion of twins in LAO may result in small atomic displacement, which may further affect the physical properties. In this study, we observed doublet splitting in the PL spectrum of LAO crystal. Simulations showed an Al displacement of 0.09 Å in a sublattice, which may be attributable to twinning that adequately explains the spectral splitting. The carrier dynamics of these defect PLs have been studied by a femtosecond TA technique.

1.4 Fundamental properties of SrTiO$_3$

STO is a perovskite-type oxide material with a bandgap around 3.2 eV.[36,37] The lattice constant of STO is 3.905 Å, which is close to that of LAO.[38] As with LAO, STO is widely used for the epitaxial growth of many high-temperature superconductors and oxide thin films.[39] STO can be grown on a silicon substrate without forming silicon dioxide, making it an ideal buffer layer for growing other oxide materials on a silicon substrate.[40] STO has a large dielectric constant (~300) and has been used in high-voltage capacitors and other electronic devices.[41] STO is an insulator at room temperature, and with electronic doping, it can easily show semiconductor, metallic, and even superconducting properties at low temperature. For example, Nb-doped STO is electrically conductive and has been used in field-effect transistors and resistive-switching devices.[42]

STO shows many phase transitions at different temperatures: from cubic to

tetragonal below 105 K; from tetragonal to orthorhombic at around 60 K; and from orthorhombic to rhombohedral at around 30 K.[43,44]

STO has intriguing optical properties that have attracted great interest. STO has been reported to show green emission (~2.4 eV) and blue emission (~2.8 eV).[38,45,46] The former is only observed at low temperatures below 110 K. The latter is observed at high temperatures. Ar$^+$-ion-irradiated La- or Nb-doped STO shows blue emission at room temperature.[37,38] It is known that defects and impurities are common to oxide materials.[47-49] In STO, defects originating from atomic vacancies and interstitials of Sr, Ti, and O lead to defect states inside the band gap.[50,51] These defect states may contribute to PL emission. Among these defects, an oxygen vacancy is the most common one. Furthermore, oxygen vacancies may bind with Sr or Ti related defects or with other oxygen vacancies to form defect complexes. During laser excitation, electrons in these defect levels are promoted to high energy levels, from where they decay to lower energy levels. Some of these excited defect electrons relax through a radiative decay process that produces PL emission.[37,38,45,50-54] However, many of these electrons relax through nonradiative decay processes that cannot be observed by PL techniques. Therefore, other methods are required to detect these nonradiative decay processes. In this study, we investigated one-photon, multiphoton PL, and TA spectroscopy of STO and observed many more defect levels inside the band gap. Furthermore, by using the pump-probe technique, we identified the decay lifetime of these defect states. This study of the defect states in STO may provide a better understanding of the defect mechanism in the materials and lead to potential applications of STO-based devices, especially for high speed applications.

1.5 Fundamental properties of TiO$_2$

TiO$_2$, one of the most important oxide semiconductors, has attracted considerable interest owing to its unique properties. TiO$_2$ has a high dielectric constant, high refractive index, and high photocatalytic activity, as a result of which it has been widely applied to heterogeneous catalysis, solar cells, water splitting, gas sensors, and electric devices.[55-64]

TiO$_2$ exhibits three crystal structures in nature: rutile, anatase, and brookite.[65] The rutile structure is the most stable, well-defined, and commercially available crystal phase, and it has a tetragonal crystal structure. The anatase structure is a metastable form (primarily in bulk but less so in thin films) of TiO$_2$ that also has a tetragonal structure, and it can transform into a rutile structure at a high temperature; the anatase structure has higher catalytic efficiency than the rutile structure owing to its high-mobility carriers.[66] The brookite is the least common phase.

In recent years, TiO$_2$ has attracted increasing attention from the viewpoint of clean energy applications. Most of these applications are based on the photon carriers of TiO$_2$; for example, the photocatalytic reaction and solar cell conversion are based on the photochemical reaction at the TiO$_2$ surface.[67-72] Therefore, the study of photon-excited carrier dynamics is of great importance. Many optical properties of TiO$_2$, such as PL, time-resolved microwave photoconductivity, TA, terahertz spectroscopy, and time-resolved reflectance, have been reported.[73-77] However, few studies have focused on the carrier dynamics of TiO$_2$ films with donor contributions from oxygen vacancy or from a pentavalent dopant, such as Ta or Nb.

Experimental results show that both rutile and anatase TiO$_2$ have band gaps of

3.0 eV and 3.2 eV, respectively.[78,79] Owing to this large bandgap, TiO$_2$ can only absorb UV light. The majority of the solar spectrum is wasted and the efficiency is low for solar cell applications. It has been reported that by doping and introducing defect states inside the bandgap, the absorption of TiO$_2$ can be extended to the visible range, and consequently the solar efficiency can be improved.[64,67-69,71] In this study, we have investigated the carrier dynamics and photocatalytic efficiency of TiO$_2$ films with different oxygen vacancies and doping concentrations.
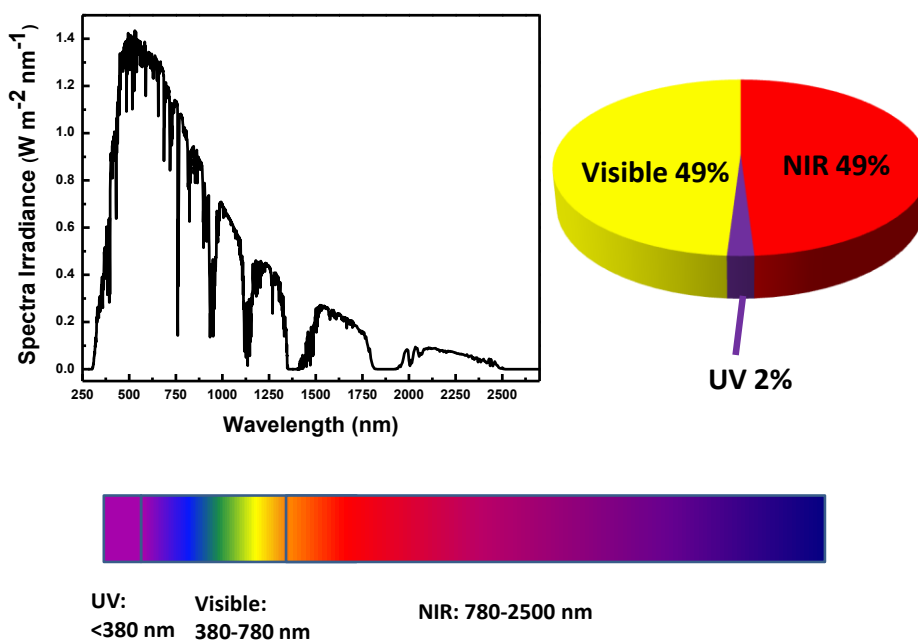
Figure 1.2. In the spectrum of solar radiation UV light falls between 100 and 380 nm and contains 2% of the overall solar energy; visible light falls range between 380 and 780 nm and contains 49% of the overall solar energy; and near-infrared light falls between 780 and 2500 nm and contains 49% of the overall solar energy.

1.6 Fundamental properties of graphene

Graphene, an atomically thick two-dimensional material, has attracted enormous attention in the last few years. Graphene is a flat monolayer of carbon atoms and serves as a basic building block for graphitic materials of all other dimensionalities. Graphene exhibits interesting properties, such as high room-temperature carrier mobility, high optical absorptivity, thermal conductivity, and mechanical strength.[80-83] Owing to these excellent and unique properties, it shows promising applications to solar cells, catalyst supports, sensors, energy storage, field-effect transistors, broadband polarizers, and nanocomposite materials.[84-91]

Graphene has carbon atoms arranged in a regular hexagonal pattern, and it serves as a building block for all graphitic forms. It can be wrapped into 0D fullerenes, rolled into 1D carbon nanotubes, or stacked into 3D graphite.[82] Owing to the linear relation between energy and momentum, graphene has massless charge carriers also known as Dirac fermions. Graphene shows excellent optical properties.[92] For example, under high excitation light, its valence band depletes and conduction band fills, resulting in broadband saturable absorption. This saturable absorption has been used in ultrafast mode-locked lasers. Furthermore, graphene shows a very large nonlinear Kerr effect and nonlinear phase shift, where a giant nonlinear refractive index of 10^{-7} cm^2 W^{-1} was observed.[93]

Owing to its nonlinear optical properties, graphene is considered as a promising optical material, and has potential applications in nonlinear photonics devices. In this study, graphene-based optical bistability was observed in different layers of graphene. The phase shift due to the large

nonlinear Kerr effect of graphene nano-bubbles (to be discussed later) may explain the optical bistability behavior in the graphene system.

2D Graphene

0D Buckyballs **1D Carbon Nanotube** **3D Graphite**
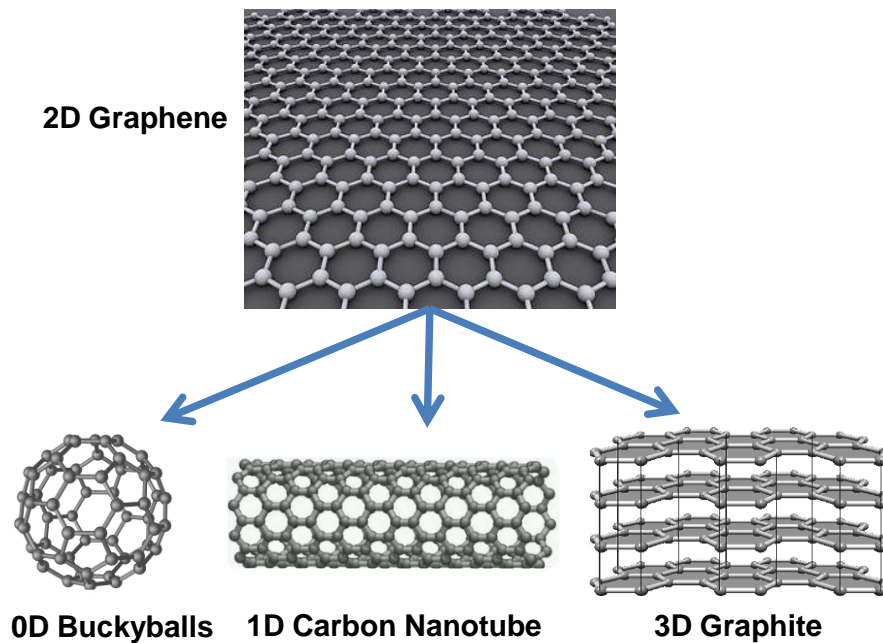
Figure 1.3. 2D graphene—building block for carbon materials such as 0D buckyballs, 1D carbon nanotube, and 3D graphite.

Energy (E)

Dirac point Momentum (K)
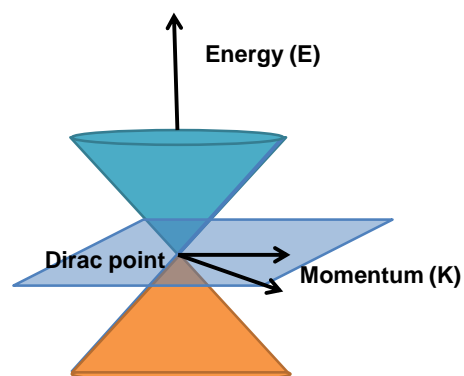
Figure 1.4. Schematic structure of energy bands in 2D graphene.

1.7 Ultrafast spectroscopy

Ultrafast spectroscopy involves recording the absorption or reflection spectrum of a sample with a probe pulse in an extremely short time (variable from nanoseconds to 100 femtoseconds) after its excitation with a pulsed laser (the pump).[94-96] This pump-probe method is used to record the energy states as well as the excited carrier dynamics of the studied materials. Many ultrafast spectroscopy techniques have been developed thus far, such as ultrafast TA, time-correlated single photon counting (TCSPC), and time-resolved photoelectron spectroscopy (TRPES).[97,98] Most of these techniques are applied for time-resolved spectroscopy, which is very useful to study dynamic processes in materials and to determine the mechanism of some physical properties.

For ultrafast spectroscopy, TA is a very important and widely used technique that can be used to study many processes, such as optical gain spectroscopy, chemical reactions, energy transfer, electron transfer, and carrier dynamics.[99-103] In this study, TA spectroscopy and single wavelength pump-probe experiments were mainly used to measure the carrier dynamics. In this experiment, an ultrafast pulse laser is used as the pump light, and the electrons of the studied material are promoted to higher excited states. A wide band probing light, also a pulsed laser, is used to obtain the absorption spectra of these excited states at various delay time following the excitation. This technique can be used to measure the carrier dynamic of both fluorescent and nonfluorescent materials. The time resolution of this technique is limited by the laser pulse duration, and therefore, this technique can detect processes as fast as 100 fs.

In this study, the transient absorption of different oxide materials was investigated. Defect levels as well as electron dynamics mechanisms for both radiative and non radiative processes were studied using TA spectroscopy.

1.8 Thesis outline

Chapter 2 introduces the basic sample preparation and characterization methods. In our study, pulsed laser deposition (PLD) is used to prepare thin films. X-ray diffraction (XRD) and Atomic force microscopy (AFM) are used to identify the structures and surface quality of the prepared films. The linear and nonlinear optical characterization studies, including UV-vis spectroscopy, PL, saturable absorption, reverse saturable absorption, multiphoton PL, Z-Scan, and optical bistability, are introduced here. Transient dynamic characterizations are addressed using pump-probe TA.

Chapter 3 discusses the PL spectrum and defect dynamics of single-crystalline LAO. The PL of LAO consists of a broad spectrum and two sharp peaks that arise from various defect levels within the bandgap. A doublet splitting of roughly 6 nm is seen in these two sharp peaks. An Al displacement of 0.09 Å in the sublattice, which is possible because of twinning, adequately explains the spectral splitting. Femtosecond pump-probe experiments further reveal that many of these defect levels have decay time in the order of a few picoseconds, whereas the lowest defect states have decay time longer than nanosecond to the valence band.

Chapter 4 describes the defect energy levels of STO studied by above bandgap (350nm), just below band edge (400nm) and sub bandgap (800 nm) excitations. The room temperature multi-photon excited PL of STO is observed for the first time by using 800 nm fs excitation. The PL is centered at 2.8 eV and has

a lifetime of 25 ns. A number of new defect levels in STO are resolved by femtosecond TA studies using sub-bandgap excitation. The defect levels with band edge (400 nm) excitation have short (<2 ps) lifetime, those defect levels with above band gap (350 nm) and below band gap (800 nm) excitation exhibit long (>1 ns) lifetime. This long lifetime defect dynamics can help to explain the PL mechanism.

Chapter 5 describes the defect dynamics and applications of TiO_2 and Ta-doped TiO_2. The bulk single crystal shows broadened transient absorption peaks with a long lifetime decay over several nanoseconds. On the other hand, the defect levels in TiO_2 films show fast decay with a lifetime of 180-300 ps. The carrier lifetime is found to increase as oxygen vacancies decrease. Oxygen vacancies and defects in the films may form recombination centers, resulting in an increase in the carrier recombination rate. Ta-doped TiO_2 shows a fast decay of sub-nanoseconds unlike undoped TiO_2, which may be due to the reduction of oxygen vacancies during the Ta-substation process. Slow recombination rate of the TiO_2 films is also used in the photo degradation experiment (where TiO_2 is used as a photocatalyst), where low-oxygen-vacancy TiO_2 films show relatively high efficiency.

Chapter 6 describes the nonlinear Kerr-effect-induced optical bistability. Graphene, a material with a large nonlinear Kerr effect, is used in the experiment. A clear bistability hysteresis loop is observed in monolayer graphene. The device design exploits the strong nonlinear light-matter interactions in graphene and the bistability arises from the combination of optical nonlinearity in graphene and cavity feedback. It is found that monolayer graphene causes $\lambda/2$ optical length change during resonance. The all-optical switching with a time scale of nanoseconds originated from

dispersive optical nonlinearities. This graphene-based optical bistable device could form the building block of future high-speed all-optical circuitry.

Chapter 7 summarizes this thesis relevant outcome and discusses future works.

Bibliography

1. G. E. Moore, "Cramming more components onto integrated circuits," Electronics, 38, 114 (1965).

2. M. K. Wu, J. Ashburn, C. J. Torng, P. H. Hor, R. Meng, L. Gao, Z. J. Huang, Y. Wang and C. Chu, "Superconductivity at 93K in a new mixed-phase Y-Ba-Cu-O compund system at ambient pressure," Physical Review Letters, 58, 908-910 (1987).

3. R. Waser and M. Aono, "Nanoionics-based resistive switching memories," Nature Materials, 6, 833-840 (2007).

4. S. Jin, T. H. Tiefel, M. Mccormack, R. A. Fastnacht, R. Ramesh, and L. H. Chen, "Thousandfold change in resistivity magnetoresistive La-Ca-Mn-O films," Science, 264, 413-415 (1994).

5. A. Ohtomo, D. Muller, J. Grazul and H. Y. Hwang, "Artificial charge-modulationin atomic-scale perovskite titanate superlattices," Nature 419, 378-380 (2002).

6. A. Ohtomo and H. Y. Hwang, "A high-mobility electron gas at the LaAlO3/SrTiO3 heterointerface," Nature 427, 423-426, (2004).

7. S. Thiel, G. Hammerl, A. Schmehl, C. Schneider and J. Mannhart, "Tunable quasi-two-dimensional electron gases in oxide heterostructures," Science 313, 1942 (2006).

8. A. D. Caviglia, S. Gariglio, N. Reyren, D. Jaccard, T. Schneider, M. Gabay, S. Thiel, G. Hammerl, J. Mannhart and J. M. Triscone, "Electric field control of the LaAlO3/SrTiO3 interface ground state", Nature 456, 624-627 (2008).

9. H. Y. Hwang, Y. Iwasa, M. Kawasaki, B. Keimer, N. Nagaosa and Y. Tokura, "Emergent phenomena at oxide interfaces," Nat Mater 11, 103-113 (2012).

10. T. Hasegawa, S. Mouri, Y. Yamada and K. Tanaka, "Giant photo-induced

dielectricity in SrTiO3," Journal of the Physical Society of Japan 72, 41-44, (2003).

11. G. Herranz, M. Basletic, M. Bibes, C. Carretero, E. Tafra, E. Jacquet, K. Bouzehouane, C. Deranlot, A. Hamzic, J. M. Broto, A. Barthelemy and A. Fert, "High mobility in LaAlO3/SrTiO3 heterostructures: Origin, dimensionality, and perspectives," Physical Review Letters 98, (2007).

12. S. Mochizuki, F. Fujishiro and S. Minami, "Photoluminescence and reversible photo-induced spectral change of SrTiO3," Journal of Physics-Condensed Matter 17, 923-948, (2005).

13. S. Thiel, C. W. Schneider, L. F. Kourkoutis, D. A. Muller, N. Reyren, A. D. Caviglia, S. Gariglio, J. M. Triscone and J. Mannhart, "Electron Scattering at Dislocations in LaAlO3/SrTiO3 Interfaces," Physical Review Letters 102, (2009).

14. Ariando, X. Wang, G. Baskaran, Z. Q. Liu, J. Huijben, J. B. Yi, A. Annadi, A. R. Barman, A. Rusydi, S. Dhar, Y. P. Feng, J. Ding, H. Hilgenkamp and T. Venkatesan, "Electronic phase separation at the LaAlO3/SrTiO3 interface," Nat Commun 2, 188 (2011).

15. X. Wang, W. M. Lü, A. Annadi, Z. Q. Liu, K. Gopinadhan, S. Dhar, T. Venkatesan and Ariando, "Magnetoresistance of two-dimensional and three-dimensional electron gas in LaAlO3/SrTiO3 heterostructures: Influence of magnetic ordering, interface scattering, and dimensionality", Physical Review B 84, 075312 (2011).

16. R. S. Singh, X. Wang, W. Chen, Ariando and A. T. S. Wee, "Large room-temperature quantum linear magnetoresistance in multilayered epitaxial graphene: Evidence for two-dimensional magnetotransport", Applied Physics Letters 101, 183105 (2012).

17. Z. Q. Liu, C. J. Li, W. M. Lü, X. H. Huang, Z. Huang, S. W. Zeng, X. P. Qiu, L. S. Huang, A. Annadi, J. S. Chen, J. M. D. Coey, "Origin of the Two-Dimensional Electron Gas at LaAlO3/SrTiO3 Interfaces: The Role of

Oxygen Vacancies and Electronic Reconstruction", Physical Review X 3, 021010 (2013).

18. A. Annadi, Z. Huang, K. Gopinadhan, X. R. Wang, A. Srivastava, Z. Q. Liu, H. H. Ma, T. P. Sarkar, T. Venkatesan and Ariando, "Fourfold oscillation in anisotropic magnetoresistance and planar Hall effect at the LaAlO3/SrTiO3 heterointerfaces: Effect of carrier confinement and electric field on magnetic interactions," Physical Review B 87, 201102 (2013).

19. Q. Bao, H. Zhang, Y. Wang, Z. Ni, Y. Yan, Z. X. Shen, K. P. Loh and D. Y. Tang, "Atomic‐Layer Graphene as a Saturable Absorber for Ultrafast Pulsed Lasers," Advanced Functional Materials 19, 3077-3083 (2009).

20. Z. Sun, T. Hasan, F. Torrisi, D. Popa, G. Privitera, F. Wang, F. Bonaccorso, D. M. Basko and A. C. Ferrari, "Graphene mode-locked ultrafast laser," ACS Nano 4, 803-810 (2010).

21. E. Hendry, P. Hale, J. Moger, A. Savchenko and S. Mikhailov, "Coherent nonlinear optical response of graphene," Phys. Rev. Lett 105, 097401 (2010).

22. http://en.wikipedia.org/wiki/Perovskite_(structure).

23. J. Chakhalian, A. Millis and J. Rondinelli, "Whither the oxide interface. Nature Materials," 11, 92-94 (2012).

24. X. H. Zeng, L. H. Zhang, G. J. Zhao, J. Xu, Y. Hang, H. Y. Pang, M. Y. Jie, C. F. Yan and X. M. He, "Crystal growth and optical properties of LaAlO3 and Ce-doped LaAlO3 single crystals," Journal of Crystal Growth 271, 319-324, (2004).

25. A. Boudali, B. Amrani, M. D. Khodja, A. Abada and K. Amara, "First-principles study of structural, elastic, electronic, and thermal properties of LaAlO3 perovskite," Computational Materials Science 45, 1068-1072, (2009).

26. D. Reagor and F. Garzon, "Dielectric and optical properties of substrates for high-temperature superconductor films," Applied Physics Letters 58,

2741-2743 (1991).

27. Z. M. Zhang, B. I. Choi, M. I. Flik and A. C. Anderson, "INFRARED REFRACTIVE-INDEXES OF LAALO3, AND LAGAO3, AND NDGAO3," Journal of the Optical Society of America B-Optical Physics 11, 2252-2257, (1994).

28. W. L. Wang, C. Y. Peng, Y. T. Ho and L. Chang, "Microstructure of a-plane ZnO grown on LaAlO3 (001)," Thin Solid Films 518, 2967-2970, (2010).

29. A. Lotnyk, S. Senz and D. Hesse, "Epitaxial growth of TiO2 thin films on SrTiO3, LaAlO3 and yttria-stabilized zirconia substrates by electron beam evaporation," Thin Solid Films 515, 3439-3447 (2007).

30. J. Chrosch and E. K. Salje, "Temperature dependence of the domain wall width inLaAlO3," Journal of Applied Physics 85, 722-727 (1999).

31. S. Hayward, S. Redfern and E. Salje, "Order parameter saturation in LaAlO3," Journal of Physics: Condensed Matter 14, 10131 (2002).

32. G. D. Yao, S. Y. Hou, M. Dudley and J. M. Phillips, "Synchrotron x-ray topography studies of twin structures in lanthanum aluminate single crystals," J. Mater. Res. 7, 1847-1855, (1992).

33. G. W. Berkstresser, A. J. Valentino and C. D. Brandle, "Growth of single-crystal of lanthanum aluminate," Journal of Crystal Growth 109, 467-471 (1991).

34. M. G. Norton and R. R. Biggers, "In situ transmission electron microscopy observations of twinning in lanthanum aluminate," Scr. Metall. Materialia 32, 481-485, (1995).

35. C. H. Kim, J. W. Jang, S. Y. Cho, I. T. Kim and K. S. Hong, "Ferroelastic twins in LaAlO3 polycrystals," Physica B 262, 438-443 (1999).

36. J. H. Haeni, P. Irvin, W. Chang, R. Uecker, P. Reiche, Y. L. Li, S.

Choudhury, W. Tian, M. E. Hawley, B. Craigo, A. K. Tagantsev, X. Q. Pan, S. K. Streiffer, L. Q. Chen, S. W. Kirchoefer, J. Levy and D. G. Schlom, "Room-temperature ferroelectricity in strained SrTiO3," Nature 430, 758-761, (2004).

37. Y. Yamada, H. Yasuda, T. Tayagaki and Y. Kanemitsu, "Temperature Dependence of Photoluminescence Spectra of Nondoped and Electron-Doped SrTiO3: Crossover from Auger Recombination to Single-Carrier Trapping," Physical Review Letters 102, (2009).

38. D. Kan, T. Terashima, R. Kanda, A. Masuno, K. Tanaka, S. Chu, H. Kan, A. Ishizumi, Y. Kanemitsu and Y. Shimakawa, "Blue-light emission at room temperature from Ar+-irradiated SrTiO3," Nature Materials 4, 816-819 (2005).

39. P. Berberich, J. Tate, W. Dietsche and H. Kinder, "Low‐temperature preparation of superconducting YBa2Cu3O7− δ films on Si, MgO, and SrTiO3 by thermal coevaporation," Applied Physics Letters 53, 925-926 (1988).

40. R. McKee, F. Walker and M. Chisholm, "Crystalline oxides on silicon: the first five monolayers," Physical Review Letters 81, 3014-3017 (1998).

41. C. Koonce, M. L. Cohen, J. Schooley, W. Hosler and E. Pfeiffer, "Superconducting Transition Temperatures of Semiconducting SrTiO3," Physical Review 163, 380 (1967).

42. A. Beck, J. G. Bednorz, C. Gerber, C. Rossel and D. Widmer, "Reproducible switching effect in thin oxide films for memory applications," Applied Physics Letters 77, 139-141 (2000).

43. F. W. Lytle, "X‐Ray Diffractometry of Low‐Temperature Phase Transformations in Strontium Titanate," Journal of Applied Physics 35, 2212-2215 (1964).

44. E. Tosatti and R. Martoňák, "Rotational melting in displacive quantum paraelectrics," Solid State Commun. 92, 167-180 (1994).

45．L. Grabner, "Photoluminescence in SrTiO3," Physical Review 177, 1315-1323 (1969).

46. L. F. Mattheiss, "Energy Bands for KNiF3, SrTiO3, KMoO3, and KTaO3," Physical Review B 6, 4718-4740 (1972).

47. W. Baer, "Free-Carrier Absorption in Reduced SrTiO3," Physical Review 144, 734 (1966).

48. H. Yamada and G. Miller, "Point defects in reduced strontium titanate," Journal of Solid State Chemistry 6, 169-177 (1973).

49. R. Wild, E. M. Rockar and J. C. Smith, "Thermochromism and Electrical Conductivity in Doped SrTiO3," Physical Review B 8, 3828 (1973).

50. C. Lee, J. Destry and J. Brebner, "Optical absorption and transport in semiconducting SrTiO3," Physical Review B 11, 2299 (1975).

51. J. Rho, S. Jang, Y. D. Ko, S. Kang, D. W. Kim, J. S. Chung, M. Kim, M. Han and E. Choi, "Photoluminescence induced by thermal annealing in SrTiO3 thin film," Applied Physics Letters 97, (2010).

52. Y. Yamada and Y. Kanemitsu, "Band-to-band photoluminescence in SrTiO3," Physical Review B 82, 121103 (2010).

53. A. Rubano, D. Paparo, F. M. Granozio, U. S. di Uccio and L. Marrucci, "Blue luminescence of SrTiO3 under intense optical excitation," Journal of Applied Physics 106, (2009).

54. Y. Yamada, H. Yasuda, T. Tayagaki and Y. Kanemitsu, "Photocarrier recombination dynamics in highly excited SrTiO3 studied by transient absorption and photoluminescence spectroscopy," Applied Physics Letters 95, (2009).

55. A. Fujishima, T. N. Rao and D. Tryk, "TiO2 photocatalysts and diamond electrodes," Electrochimica acta 45, 4683-4690 (2000).

56. J. C. Yu, J. Yu, W. Ho, Z. Jiang and L. Zhang, "Effects of F-doping on the photocatalytic activity and microstructures of nanocrystalline TiO2 powders," Chemistry of Materials 14, 3808-3816 (2002).

57. A. M. Ruiz, G. Sakai, A. Cornet, K. Shimanoe, J. R. Morante and N. Yamazoe, "Cr-doped TiO2 gas sensor for exhaust NO2 monitoring," Sensors and Actuators B: Chemical 93, 509-518 (2003).

58. Y. Wang, G. Du, H. Liu, D. Liu, S. Qin, N. Wang, C. Hu, X. Tao, J. Jiao and J. Wang, "Nanostructured Sheets of Ti-O Nanobelts for Gas Sensing and Antibacterial Applications," Advanced Functional Materials 18, 1131-1137 (2008).

59. B. O'regan and M. Grfitzeli, "A low-cost, high-efficiency solar cell based on dye-sensitized," Nature 353, 24 (1991)

60. J. R. Jennings, A. Ghicov, L. M. Peter, P. Schmuki and A. B. Walker, "Dye-sensitized solar cells based on oriented TiO2 nanotube arrays: transport, trapping, and transfer of electrons," Journal of the American Chemical Society 130, 13364-13372 (2008).

61. Y.-C. Chan, J.-N. Chen and M.-C. Lu, "Intermediate inhibition in the heterogeneous UV-catalysis using a TiO2 suspension system," Chemosphere 45, 29-35 (2001).

62. Y. W. Chen, J. D. Prange, S. Dühnen, Y. Park, M. Gunji, C. E. Chidsey and P. C. McIntyre, "Atomic layer-deposited tunnel oxide stabilizes silicon photoanodes for water oxidation," Nature Materials 10, 539-544 (2011).

63. K. Albertin and I. Pereyra, "Study of reactive sputtering titanium oxide for metal-oxide-semiconductor capacitors," Thin Solid Films 517, 4548-4554 (2009).

64. U. Gesenhues, "Al-doped TiO2 pigments: influence of doping on the photocatalytic degradation of alkyd resins," Journal of Photochemistry and Photobiology A: Chemistry 139, 243-251 (2001).

65. F. Grant, "Properties of rutile (titanium dioxide)," National Bureau of Standards, Washington, DC, 1959.

66. M. Murakami, Y. Matsumoto, K. Nakajima, T. Makino, Y. Segawa, T. Chikyow, P. Ahmet, M. Kawasaki and H. Koinuma, "Anatase TiO2 thin

films grown on lattice-matched LaAlO3 substrate by laser molecular-beam epitaxy," Applied Physics Letters 78, 2664-2666 (2001).

67. L. Mi, P. Xu, H. Shen and P.-N. Wang, "Recovery of visible-light photocatalytic efficiency of N-doped TiO2 nanoparticulate films," Journal of Photochemistry and Photobiology A: Chemistry 193, 222-227, (2008).

68. X. Chen, L. Liu, P. Y. Yu and S. S. Mao, "Increasing Solar Absorption for Photocatalysis with Black Hydrogenated Titanium Dioxide Nanocrystals," Science 331, 746-750, (2011).

69. H. Y. Song, H. F. Jiang, X. Q. Liu and G. Y. Meng, "Efficient degradation of organic pollutant with WOx modified nano TiO2 under visible irradiation," J. Photochem. Photobiol. A-Chem. 181, 421-428, (2006).

70. S. Senthilkumaar, K. Porkodi and R. Vidyalakshmi, "Photodegradation of a textile dye catalyzed by sol-gel derived nanocrystalline TiO2 via ultrasonic irradiation," J. Photochem. Photobiol. A-Chem. 170, 225-232, (2005).

71. R. Asahi, T. Morikawa, T. Ohwaki, K. Aoki and Y. Taga, "Visible-light photocatalysis in nitrogen-doped titanium oxides," Science 293, 269-271, (2001).

72. M. R. Hoffmann, S. T. Martin, W. Y. Choi and D. W. Bahnemann, "Environmental applications of semiconductor photocatalysis," Chemical Reviews 95, 69-96, (1995).

73. C. Colbeau-Justin, M. Kunst and D. Huguenin, "Structural influence on charge-carrier lifetimes in TiO2 powders studied by microwave absorption," Journal of materials science 38, 2429-2437, (2003).

74. R. Katoh, M. Murai and A. Furube, "Electron-hole recombination in the bulk of a rutile TiO2 single crystal studied by sub-nanosecond transient absorption spectroscopy," Chem. Phys. Lett. 461, 238-241, (2008).

75. A. Furube, T. Asahi, H. Masuhara, H. Yamashita and M. Anpo, "Charge carrier dynamics of standard TiO2 catalysts revealed by femtosecond

diffuse reflectance spectroscopy," J. Phys. Chem. B 103, 3120-3127, doi:10.1021/jp984162h (1999).

76. E. Hendry, F. Wang, J. Shan, T. F. Heinz and M. Bonn, "Electron transport in TiO2 probed by THz time-domain spectroscopy," Physical Review B 69 (2004).

77．Y. Yamada and Y. Kanemitsu, "Blue photoluminescence of highly photoexcited rutile TiO2: Nearly degenerate conduction-band effects," Physical Review B 82, 113103 (2010).

78. J. Pascual, J. Camassel and H. Mathieu, "Fine structure in the intrinsic absorption edge of TiO2," Physical Review B 18, 5606 (1978).

79. W. Zhang, M. Zhang, Z. Yin and Q. Chen, "Photoluminescence in anatase titanium dioxide nanocrystals," *Applied Physics B* **70**, 261-265 (2000).

80. A. K. Geim, "Graphene: status and prospects," Science 324, 1530-1534 (2009).

81. C. N. R. Rao, A. K. Sood, K. S. Subrahmanyam and A. Govindaraj, "Graphene: The New Two-Dimensional Nanomaterial," Angewandte Chemie International Edition 48, 7752-7777, (2009).

82. A. K. Geim and K. S. Novoselov, "The rise of graphene," Nat Mater 6, 183-191 (2007).

83. M. Segal, "Selling graphene by the ton," Nat Nano 4, 612-614 (2009).

84. K. Novoselov, A. K. Geim, S. Morozov, D. Jiang, Y. Zhang, S. Dubonos, I. Grigorieva and A. Firsov, "Electric field effect in atomically thin carbon films," Science 306, 666-669 (2004).

85. M. D. Stoller, S. Park, Y. Zhu, J. An and R. S. Ruoff, "Graphene-Based Ultracapacitors," Nano Letters 8, 3498-3502, (2008).

86. X. Wang, L. Zhi and K. Mullen, "Transparent, Conductive Graphene Electrodes for Dye-Sensitized Solar Cells," Nano Letters 8, 323-327, (2007).

87．L. Ponomarenko, F. Schedin, M. Katsnelson, R. Yang, E. Hill, K.

Novoselov and A. Geim, "Chaotic Dirac billiard in graphene quantum dots," Science 320, 356-358 (2008).

88. Y. Si and E. T. Samulski, "Exfoliated Graphene Separated by Platinum Nanoparticles," Chemistry of Materials 20, 6792-6797, (2008).

89. F. Schedin, A. K. Geim, S. V. Morozov, E. W. Hill, P. Blake, M. I. Katsnelson and K. S. Novoselov, "Detection of individual gas molecules adsorbed on graphene," Nat Mater 6, 652-655, (2007).

90. S. Stankovich, D. A. Dikin, G. H. Dommett, K. M. Kohlhaas, E. J. Zimney, E. A. Stach, R. D. Piner, S. T. Nguyen and R. S. Ruoff, "Graphene-based composite materials," Nature 442, 282-286 (2006).

91. Q. Bao, H. Zhang, B. Wang, Z. Ni, C. H. Y. X. Lim, Y. Wang, D. Y. Tang and K. P. Loh, "Broadband graphene polarizer," Nature photonics 5, 411-415 (2011).

92. Z. B. Liu, X. L. Zhang, X. Q. Yan, Y. S. Chen and J. G. Tian, "Nonlinear optical properties of graphene-based materials," Chin. Sci. Bull. 57, 2971-2982, (2012).

93. H. Zhang, S. Virally, Q. Bao, L. Kian Ping, S. Massar, N. Godbout and P. Kockaert, "Z-scan measurement of the nonlinear refractive index of graphene", Optics Letters 37, 1856-1858 (2012)

94．S. K. Sundaram and E. Mazur, "Inducing and probing non-thermal transitions in semiconductors using femtosecond laser pulses," Nat Mater 1, 217-224 (2002).

95. J. Q. Chen, X. Wang, Y. H. Lu, A. R. Barman, G. J. You, G. C. Xing, T. C. Sum, S. Dhar, Y. P. Feng, Ariando, Q.-H. Xu and T. Venkatesan, "Defect dynamics and spectral observation of twinning in single crystalline LaAlO3 under subbandgap excitation," Applied Physics Letters 98, 041904 (2011).

96. X. Wang, J. Q. Chen, A. R. Barman, S. Dhar, Q.-H. Xu, T. Venkatesan and Ariando, "Static and ultrafast dynamics of defects of SrTiO3 in LaAlO3/SrTiO3 heterostructures," Applied Physics Letters 98, 081916

(2011).

97. R. W. Boyd, "Nonlinear optics," (Academic press, 2003).

98. P. P. Banerjee, "Nonlinear Optics: Theory, Numerical Modeling and Applications" Vol. 86 (CRC Press, 2003).

99. V. Klimov, A. Mikhailovsky, S. Xu, A. Malko, J. Hollingsworth, C. Leatherdale, H.-J. Eisler and M. Bawendi, "Optical gain and stimulated emission in nanocrystal quantum dots," Science 290, 314-317 (2000).

100. K. Wynne and R. Hochstrasser, "Anisotropy as an ultrafast probe of electronic coherence in degenerate systems exhibiting Raman scattering, fluorescence, transient absorption and chemical reactions," Journal of Raman Spectroscopy 26, 561-569 (1995).

101. A. R. Holzwarth, G. Schatz, H. Brock and E. Bittersmann, "Energy transfer and charge separation kinetics in photosystem I: Part 1: Picosecond transient absorption and fluorescence study of cyanobacterial photosystem I particles," Biophysical journal 64, 1813-1826 (1993).

102. F. D. Lewis, T. Wu, Y. Zhang, R. L. Letsinger, S. R. Greenfield and M. R. Wasielewski, "Distance-dependent electron transfer in DNA hairpins," Science 277, 673-676 (1997).

103. W. Choi, A. Termin and M. R. Hoffmann, "The role of metal ion dopants in quantum-sized TiO2: correlation between photoreactivity and charge carrier recombination dynamics," The Journal of Physical Chemistry 98, 13669-13679 (1994).

Chapter 2 Sample preparation and characterization methods

2.1 Sample preparation: pulsed laser deposition (PLD) technique

PLD is a thin-film preparation technique that involves physical vapor deposition.[1-6] A high-power pulsed laser beam is used to vaporize the target material, and the vapor is then deposited onto the substrate. The advantage of the technique is the preservation of the stoichiometry of the target in the film under the proper conditions. Deposition can occur in the presence of different background gases. Oxygen is the most commonly used gas for oxide material deposition.

Oxygen-vacancy-dependent oxide films are deposited by a PLD system as described below. As shown in Fig. 2.1, a 248-nm excimer laser (Lambda Physik excimer KrF UV laser) with pulse duration of 30 ns, maximum repetition rate of 30 Hz, and energy density of 2 J/cm^2 was used for deposition. The laser strikes the target material; the material then vaporizes under the high energy of the laser, as indicated by the plasma plume. This plume containing the target material is deposited onto the substrate. The substrate is attached to a heater (using silver paint), through which the substrate temperature can be controlled properly. The target-to-substrate distance can vary from 5 to 10 cm. By using a turbo molecular pump, a low background vacuum level of 10^{-7} Torr can be achieved. During deposition, the pressure can be controlled by filling in different gases, such as O_2, N_2, H_2, and Ar. The deposition laser energy density, laser repetition rate, substrate-to-target distance, substrate temperature, and deposition pressure can affect the film quality. By choosing

proper deposition parameters, good quality films can be obtained.[7,8]
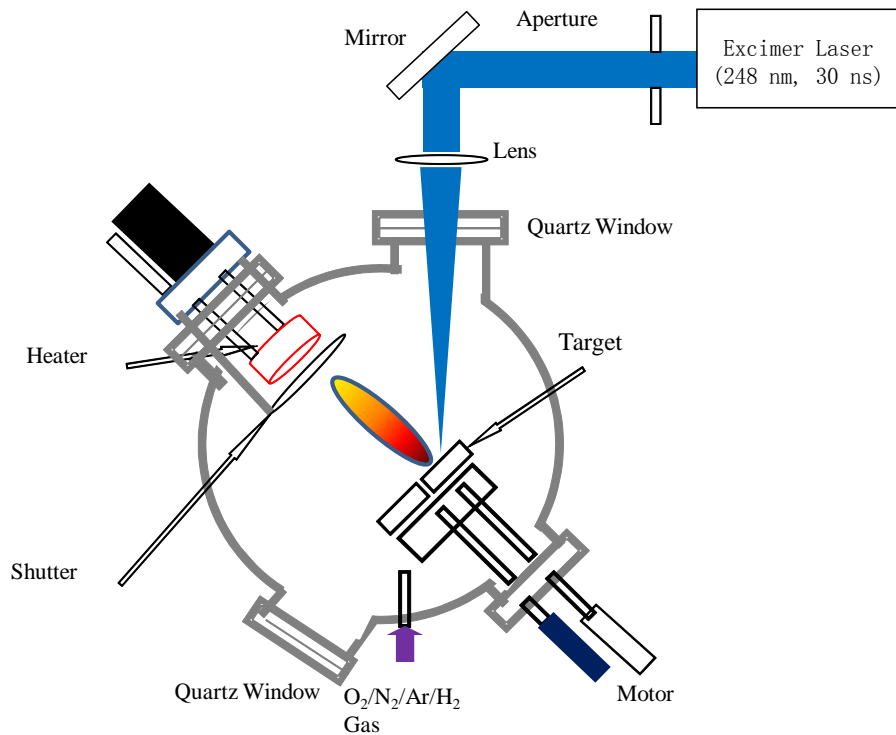
Figure 2. 1. Schematic of pulsed laser deposition setup.

2.2 Structure characterization technique

2.2.1 X-ray diffraction (XRD)

XRD is the most commonly used technique for crystal structure characterization measurements.[9,10] Figure 2.2 shows the Bruker D8 Discover XRD model used in our experiment. The X-ray is generated from the Cu Kα source operated at 40 kV and 40 mA, and a VÅNTEC-2000 2D detector is

used to collect the diffracted beam. The diffraction spectrum contains information about the crystal structure as well as the lattice constant. By comparing this data with the XRD database, we can obtain the desired information.

As shown in Fig. 2.3, the working principle of XRD is based on Bragg's Law.[11] When the incident X-ray and the lattice distance satisfy the following equation, constructive interference occurs.

$$2d\sin\theta = n\lambda, \tag{2.1}$$

where d is the lattice space; θ the angle between the incident X-ray and the lattice plane; n the order of diffraction; and λ the wavelength of the X-ray.
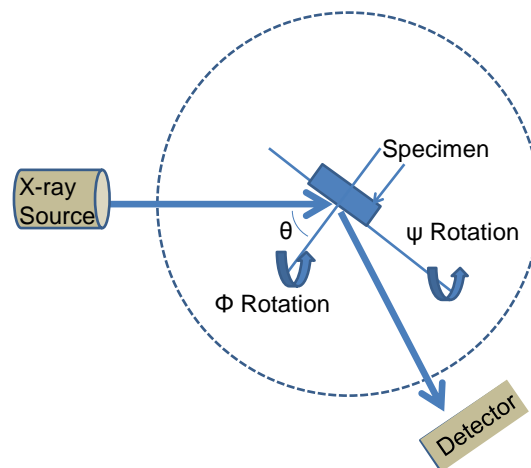
Figure 2.2. Schematic graph of X-ray diffraction experimental setup.
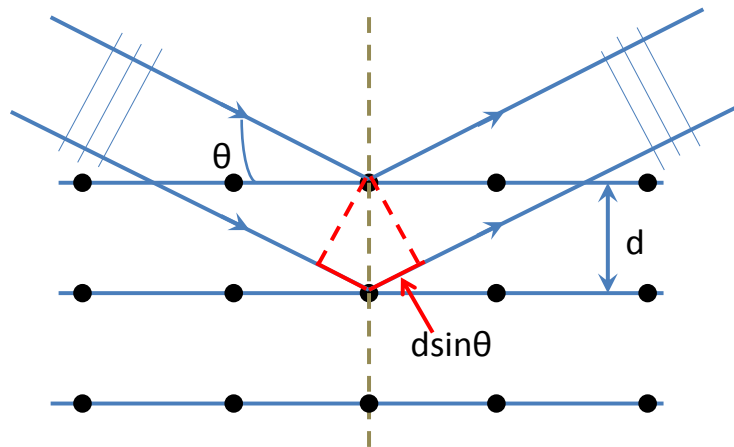
Figure 2.3. Working principle of X-ray diffraction**.**

2.2.2 Atomic force microscopy (AFM)

AFM is a type of scanning probe microscopy having a very high resolution in the nanometer range.[12,13] A sharp tip with a radius of a few nanometers is used to scan the sample surface. According to Hooke's law, when the tip approaches the sample surface, the forces between the tip and the sample cause cantilever deflection. This deflection can be detected by using a photodiode array to measure information about the sample surface. A schematic of the AFM experimental setup is shown in Fig. 2.4 below.
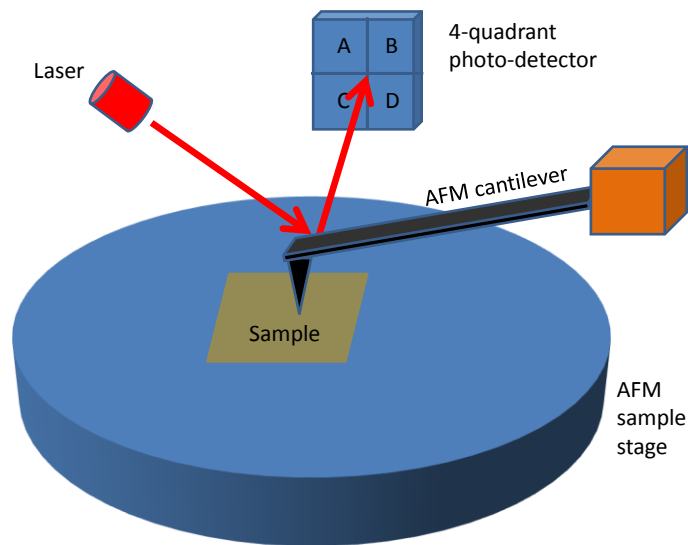
Figure 2.4. Schematic of experimental setup for AFM.

2.3 Optical characterization techniques

Optical measurement is a common but important method used for understanding the basic properties of materials, such as direct and indirect bandgaps, spectral absorption and transmission, and defect emission properties.[14-16]

2.3.1 Ultraviolet-visible spectroscopy

UV-visible transmission spectroscopy is a powerful method that is used to measure the absorption as well as the band gap of a material. In this technique, incident light is absorbed by valence band electrons, and as a result, the transmission reduces. The bandgap structure of the test material can then be identified from the transmission spectrum.

The experimental setup for UV-vis transmission spectroscopy is shown in Fig. 2.5. The incident beam is split into two parts: one part passes through the

sample, and the other part act as a reference. Light is absorbed by the sample and leads to transmission T. The reference part has transmission T_0. By comparing T and T_0, we can identify the absorption of the test sample, and thus the nature of the band, direct or indirect. UV-vis transmission spectroscopy can also be used to observe some defect state absorption.
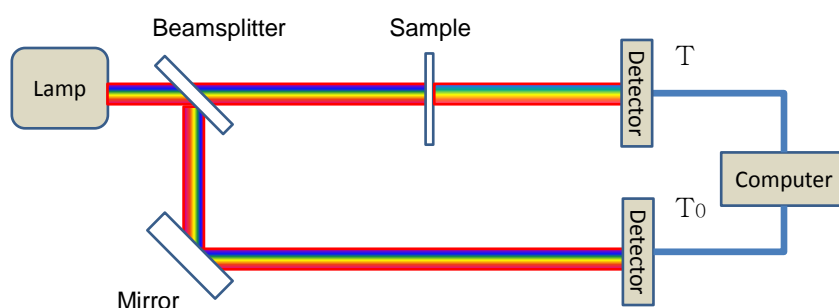
Figure 2.5. Schematic of experimental setup for UV-vis transmission spectroscopy.

2.3.2 Photoluminescence

PL is a technique used to measure the radiative properties of materials.[17,18] Valence band electrons are promoted to the excited state upon absorbing incident light, from where the excited electrons relax to low levels through radiative or non-irradiative decay processes. During radiative decay, the excited electron loses energy in the form of a photon which we call PL. This PL emission is fundamental to light-emitting diodes and lasers. From the PL spectrum, the energy level and the lifetime of the excited state from where the emission occurs can be estimated. The emission properties of a material can help in identifying defects, impurities, and the band structure of a material. In many materials, theorists are able to predict the positions of various defect levels and the experimental correlation with theory can enable us to

understand the nature of these defects.

Figure 2.6 shows a schematic of the experimental setup for PL. The light emitted from the laser source is used as the excitation source. The power of the excited light can be tuned by using a neutral density filter. One lens focuses light onto the sample, and another collects the emission light generated by the sample. The second filter is used to cut-off the excited light. The collected emission light spectrum can be obtained by using a spectrometer equipped with a CCD. From the PL spectrum, we can determine the carrier dynamics of the radiative process of the materials.
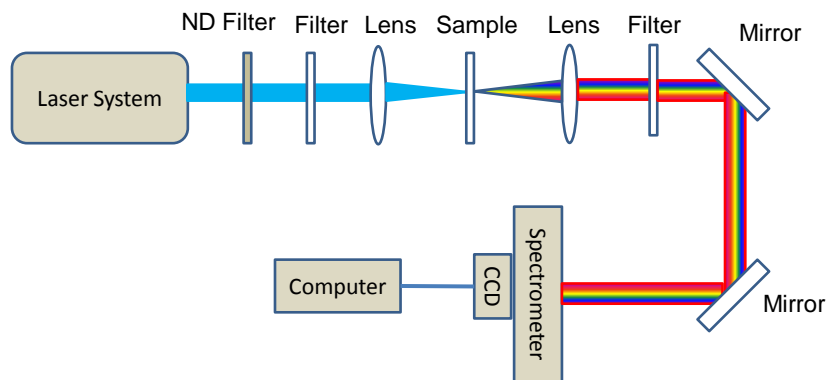
Figure 2.6. Schematic of experimental setup for photoluminescence.

2.4 Transient dynamic characterization techniques

Time-resolved spectroscopy of the excited carrier dynamics is one of the most important ways to understand the carrier dynamic mechanism of materials. This is because most important processes occur in a very short time scale in the order from a few picoseconds to nanoseconds.[19]

Figure 2.7 shows the timescale of the electron relaxation process after

excitation using the ultrafast laser. Initially, after laser excitation, the material absorbs the incident photons and the electrons are excited to a higher excited state (hot electrons) within a few femtoseconds. Thermalization is the next step, in which carrier-carrier scattering and carrier-phonon scattering dominate. Both these types of scattering occur in the sub-picosecond range after the excitation. The most interesting part is carrier removal, in which carrier recombination and diffusion are the main processes. Most optical properties of materials can be observed in this carrier removal part. After electron recombination, the recombination energy is transferred to the lattice. Subsequently, ablation, evaporation, thermal diffusion, and resolidification occur within nanosecond to microsecond range.
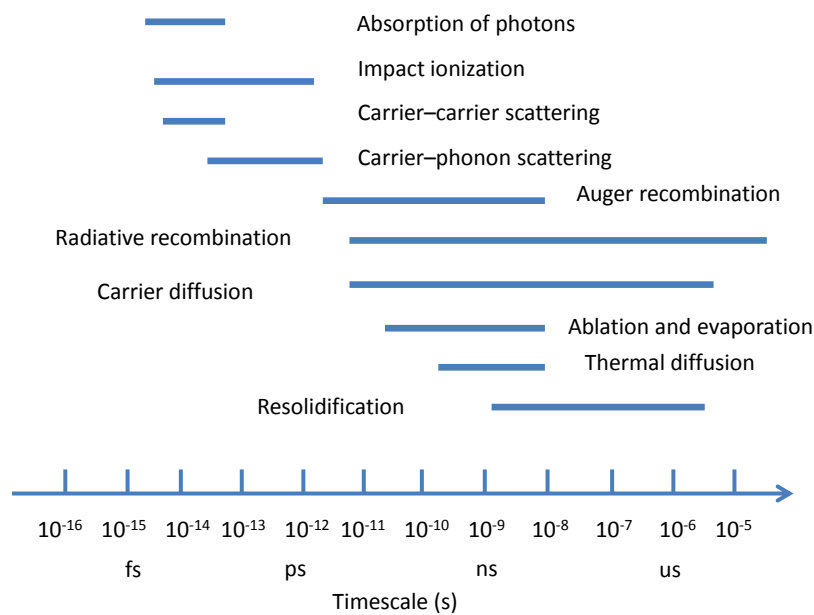
Figure 2.7. Schematic of electron relaxation upon excitation using an ultrafast laser pulse.

2.4.1 Pump-probe transient absorption spectroscopy

The defect level as well as the band structure can be studied through a TA experiment. A TA experiment can be used to determine the induced absorption or the excited state absorption, from which the defect state in the band gap can be observed. TA can also help in measuring the decay time of these defects, through which we can identify the recombination process. Furthermore, the TA spectrum can provide defect information as a function of the relaxation time over a range of probe wavelengths (broad band). On the other hand, a single-wavelength pump-probe can show the electron relaxation dynamics at a given wavelength, from which the lifetime of the electron relaxation process can be studied in finer details.

Figure 2.8 shows a typical optical setup for a pump-probe experiment using a Spectra-Physics femtosecond Ti:sapphire laser system. The laser pulses are generated using a mode-locked Ti:sapphire oscillator seeded regenerative amplifier with a pulse energy of 2 mJ at 800 nm and a repetition rate of 1 kHz. The laser beam is split into two portions. The larger portion of the beam passed through a BBO crystal to generate a 400 nm pump beam through frequency doubling. The intensity of the pump beam is attenuated using a neutral density filter and modulated using an optical chopper at a frequency of 500 Hz. The smaller portion of the beam is used to generate white light continuum in a 1 mm sapphire plate, which acts as the probe beam. The white light beam is further split into two portions: one is used as the probe and the other is used as the reference to correct for the pulse-to-pulse intensity fluctuation. The pump beam is focused onto the sample with a beam size of 300 μm, and it overlaps the smaller probe beam (diameter: 100 μm). The delay

between the pump and the probe pulses is varied using a computer-controlled translation stage (Newport, ESP 300).

Pump probe experiments are carried out at room temperature. During the measurements, the pump and the probe energies are kept low to minimize photo-damage to the samples. In a pump probe scan, the value of the normalized pump induced absorption change (T/T0) is determined as a function of the delay time between the pump and the probe pulses. The TA spectrum at different delay times is measured by passing the probe beam through a monochromator and then through a photodiode detector that is connected to the lock-in amplifier.[20,21]
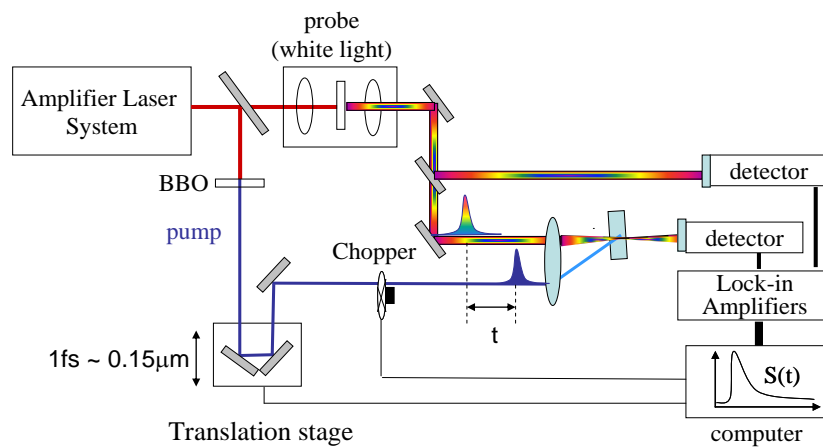
Figure 2.8. Schematic of pump-probe experimental setup.

2.4.2 Time-correlated single-photon counting

Time-correlated single-photon counting (TCSPC) is a method that is used to measure the lifetime of PL.[22] After excitation, various electrons in excited states relax to a lower state through radiative recombination at different times.

35

By observing the timeline of the emission, we can determine the exponential decay of the emission intensity, and in turn, the lifetime of the excited state.
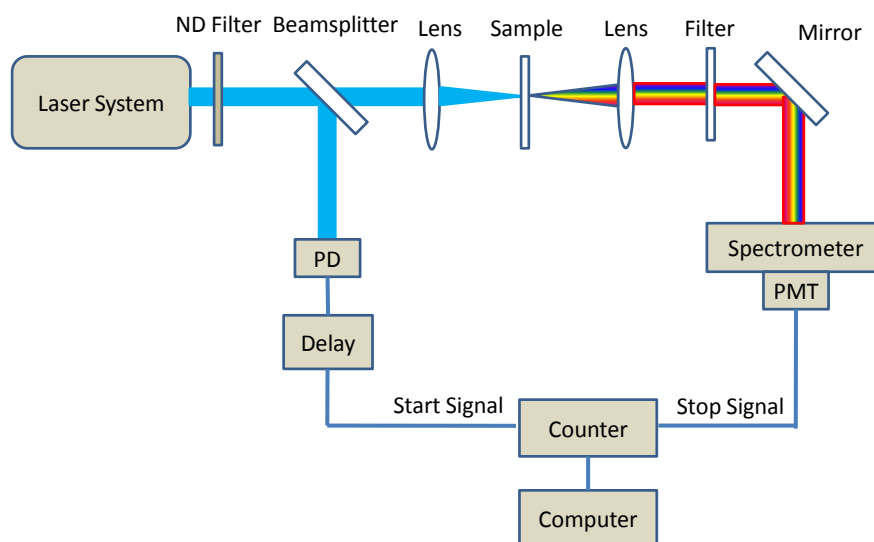
Figure 2.9. Schematic of experimental setup for TCSPC.

Figure 2.9 shows the experimental setup for TCSPC. The light from the laser is split into two portions: one portion acts as the start signal, and the other portion acts as the excitation source. The PL of the sample is collected using a spectrometer with an attached PMT, which is used for the stop signal. Both the start and the stop signals are input to the TCSPC counter, where the lifetime of the PL can be obtained.

2.5 Optical nonlinearity characterization techniques

Under high light intensity, the optical nonlinearity of materials becomes dominant.[23] For optical nonlinearity, the dielectric polarization P becomes nonlinear with the light electric field E. Many unique properties, such as the Kerr effect, self-focusing, self-phase modulation, four-wave mixing, and

multiphoton absorption are related to the nonlinear optical properties of materials.[24-27]

2.5.1 Saturable absorption and reverse saturable absorption

Saturable absorption is a nonlinear optical property in which the absorption of light decreases with the light intensity.[28] Saturable absorption is often observed at high optical intensities. Under a high excitation light intensity, valence band electrons are excited to a higher energy state. Before the excited electrons relax to the ground state, the ground state becomes depleted, resulting in a decreased absorption and a subsequent increase in the transmission. So the rate of excitation must be larger than rate of decay.

Therefore, under high excitation intensity, saturable absorption occurs. If the excited state absorption cross section is higher than that of the ground state, transmission decreases with the light intensity. This phenomenon is opposite to that observed in saturable absorption, and it is called reverse saturable absorption. Excited state absorption, multiphoton absorption, nonlinear scattering, and free carrier absorption are typical reverse saturable absorption phenomena.
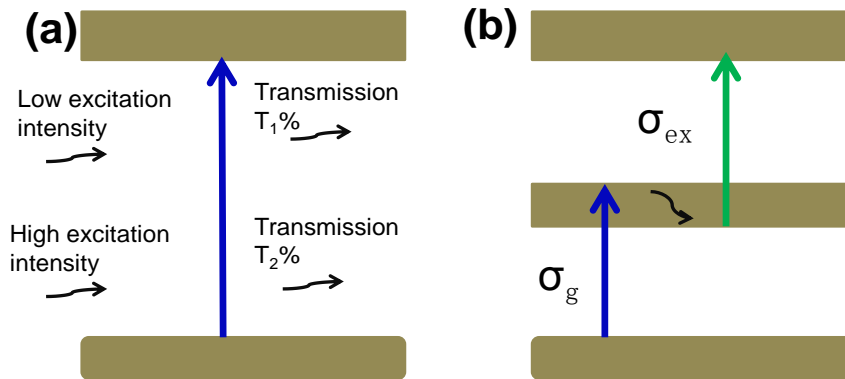
Figure 2.10. Saturable absorption and reverse saturable absorption. (a). In saturable absorption, the transmission increased with the excitation intensity ($T_1\% < T_2\%$). (b). On the other hand, in reverse saturable absorption, the ground state absorption cross section is less than the excited state ($\sigma_{ex} > \sigma_g$).

2.5.2 Multiphoton excitation photoluminescence

Multiphoton excitation PL is a higher-order nonlinear process.[29] In a linear excitation process, the photon energy is high enough to promote the valence band electrons to the excited state. Therefore, only one photon is absorbed at a time. In this case, the PL intensity is linearly dependent on the incident laser intensity. In the multiphoton excitation process, long wavelength light is used as the excitation source, where the photon energy is not adequate to promote the valence band electrons to the excited state. Electrons can only be excited to a high energy state by simultaneously absorbing multiple photons. In this case, the PL intensity increases nonlinearly with the nth power of excited light intensity where n photons are absorbed simultaneously to promote the electron to the excited state. Thus by measuring the power law of the PL signal one can understand how many photons are involved in the excitation process.

Multiphoton excitation PL requires high-intensity pulsed laser excitation.

Compared with the traditional single-photon excitation process, multiphoton PL has many advantages. As multiphoton PL is proportional to the nth power of the light intensity, the PL signal is disproportionally high at the focal point leading to spatial discrimination. This can be used for three-dimensional mapping. Another advantage is that multiphoton excitation can be realized using near-infrared light, the penetration depth of which is greater, and therefore, multiphoton excitation can be used as a probe deeper inside a material.[30]
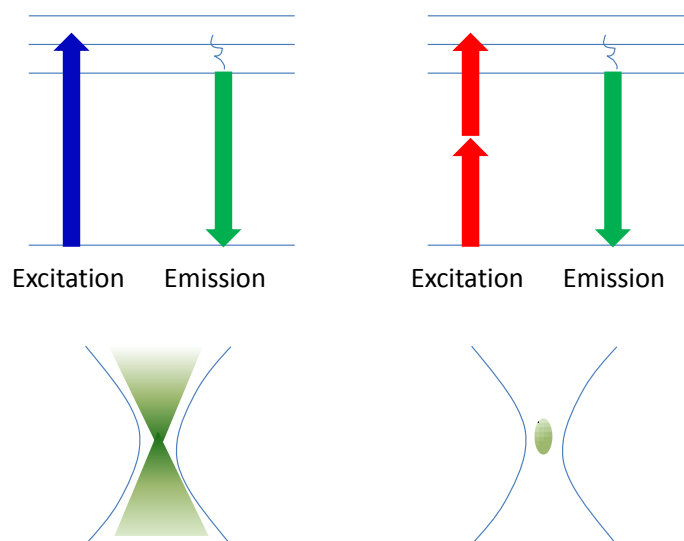
Figure 2.11. Two-photon excitation photoluminescence. The emission signal is disproportionally high at the focal point leading to spatial discrimination.

2.5.3 Z-Scan

Third-order nonlinear susceptibility, such as the Kerr nonlinearity, nonlinear absorption, and saturation irradiance, can be detected by a "closed" and "open" z-scan experiment.[31]

The nonlinear refractive index can be obtain from the "closed aperture" z-scan.[32]

$$\Delta T_{p-v} \approx 0.406 \, (1-S)^{0.25} |\Delta \emptyset_0| \qquad (2.2)$$

$$\Delta \emptyset_0 = \frac{2\pi}{\lambda} n_2 I_0 L_{eff} \qquad (2.3)$$

Where $L_{eff} = (1 - e^{-\alpha L})/\alpha$, L is the sample thickness, α is the linear absorption coefficient, S is the transmittance of the aperture in the absence of a sample. $\Delta \emptyset_0$ is the nonlinear phase shift, I_0 is the on-axis peak intensity at the focal plane. With equation (2.2) and (2.3) we can obtain the nonlinear refractive index of the sample.

Figure 2.12 shows the setup of the z-scan experiment. A Spectra-physics Ti:sapphire oscillator seeded amplifier laser system was used as the excitation source. The amplifier provides an output with a central wavelength of 800 nm, pulse duration of 100 fs, and repetition rate of 1 kHz. The output beam was split into two portions. A larger portion was focused at the sample by using a lens with a focal length of 15 cm, giving a focal spot size of ~ 40 μm (radius). Another portion was collected by the reference detector. The sample is placed on a motorized stage that can move the sample toward and away from the focus point. The transmittance of the sample was recorded accordingly. The z-scan experimental system was calibrated by measuring the third-order nonlinear absorption coefficient of a standard ZnSe sample.
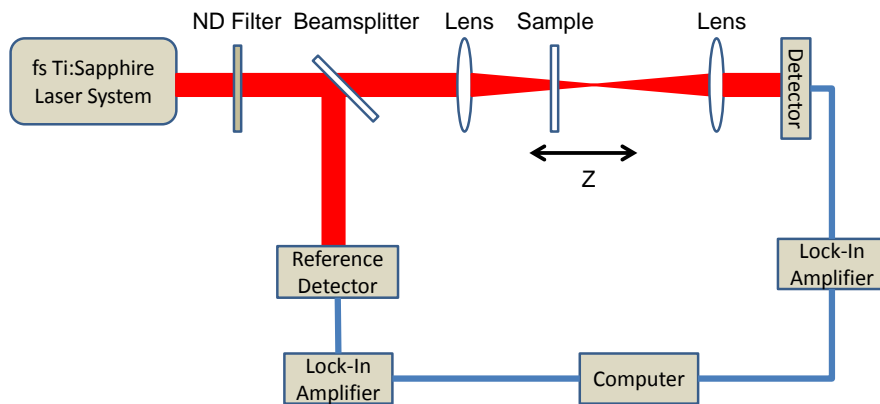
Figure 2.12. Schematic of z-scan experimental setup.

2.5.4 Optical bistability

The nonlinearity of a material can be exploited for optical bistability applications. Optical bistability refers to a situation in which two stable transmissions states can exist. By using an input laser, nonlinearity of the material, and feedback mechanism, an optical bistable device can be setup.[33]

There are two types of bistability: absorptive and refractive. Absorptive bistability is based on the saturable absorption of materials. The first bistable state occurs at the low-incident-intensity range where the intensity is below the saturable limit. The second bistable state occurs at the high-incident-intensity range where the intensity exceeds the saturable limit. Refractive bistability is based on the nonlinearity of the refractive index change. The first bistable state occurs at the low-incident-intensity range where normal linear refraction is dominant. The second bistable state occurs at the high-incident-intensity range where a nonlinear refractive index manifests. Materials with saturable absorption or the Kerr nonlinearity can be used for

41

studies of optical bistability.

Graphene has saturable absorption and a large Kerr nonlinearity that can be used for optical bistability applications. The detailed configuration of the optical bistability experimental setup is shown schematically in Fig. 2.13. A high power (up to 5 W) diode-pumped solid state laser (Newport, Millennia Edge) with single longitudinal mode (TEM$_{00}$, spectral linewidth: < 5 MHz) output at 532 nm is used in this work. A Faraday isolator is placed after the laser to prevent reflection from the Fabry-Perot cavity. The acousto-optic modulator (Isomet AOM driver, 532C-L) with a central frequency of 80 MHz and minimum rise time of 6 ns is used to modulate the input power into the Fabry-Perot cavity. The optical bistability experiments were carried out with a Burleigh RC-140 plano Fabry-Perot interferometer. Two high energy partial reflecting mirrors with surface figure of 1/10 wavelength at 532 nm are fixed in the mirror mounts of the Fabry-Perot interferometer. The front mirror has a reflectivity of 95% and the rear one has a reflectivity of 99% at 532 nm. Monolayer graphene was grown by the chemical vapor deposition (CVD) method and wet-transferred onto the rear mirror for optical experiments. An object lens (focal length= 20 mm and beam waist= 3 mm before the cavity) is placed before the cavity to focus beam onto graphene surface with a beam waist of about 1 μm. The incident and transmitted intensities are collected by two fast silicon photodiodes with 1 ns response time and displayed as horizontal and vertical deflections on a fast (response time <1ns)oscilloscope (Tektronix, 1 GHz).
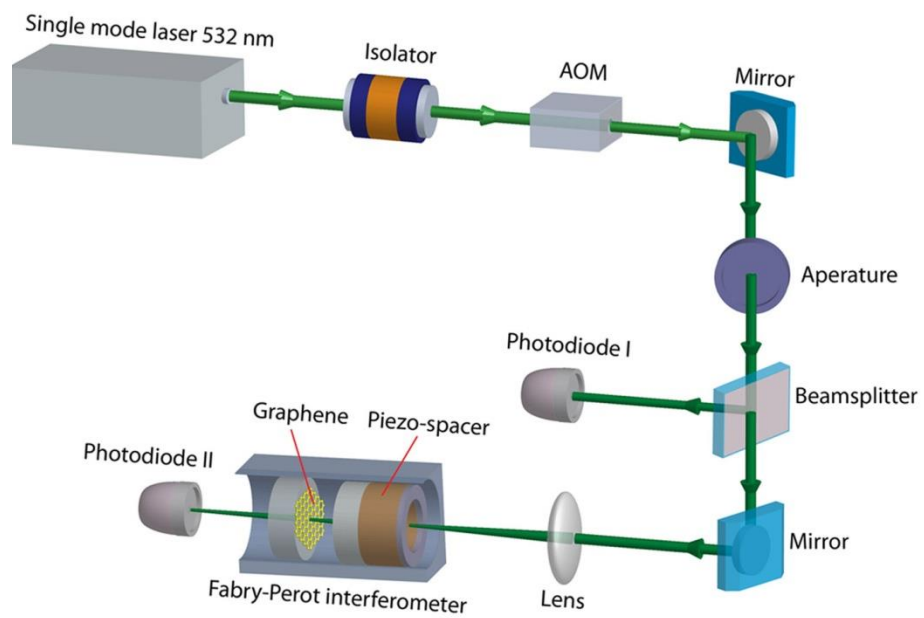
Figure 2.13. Schematic of experimental setup for optical bistability.

Bibliography

1. D. Dijkkamp, T. Venkatesan, X. D. Wu, S. A. Shaheen, N. Jisrawi, Y. H. Min-Lee, W. L. McLean and M. Croft, "Preparation of Y-Ba-Cu oxide superconductor thin films using pulsed laser evaporation from high Tc bulk material," Applied Physics Letters 51, 619-621 (1987).

2. A. Inam, M. S. Hegde, X. D. Wu, T. Venkatesan, P. England, P. F. Miceli, E. W. Chase, C. C. Chang, J. M. Tarascon and J. B. Wachtman, "As-deposited high Tc and Jc superconducting thin films made at low temperatures," Applied Physics Letters 53, 908-910 (1988).

3．S. Yilmaz, T. Venkatesan and R. Gerhard-Multhaupt, "Pulsed laser deposition of stoichiometric potassium-tantalate-niobate films from segmented evaporation targets," Applied Physics Letters 58, 2479-2481 (1991).

4. I. Zwieback, D. Perlov, J. P. Maffetone and W. Ruderman, "Electrical and optical properties of CdGeAs2 single crystals irradiated with fast electrons," Applied Physics Letters 73, 2185-2187 (1998).

5. A. E. Espinal, L. Zhang, C.-H. Chen, A. Morey, Y. Nie, L. Espinal, B. O. Wells, R. Joesten, M. Aindow and S. L. Suib, "Nanostructured arrays of semiconducting octahedral molecular sieves by pulsed-laser deposition," Nature Materials 9, 54-59 (2009).

6. D. H. Lowndes, D. Geohegan, A. Puretzky, D. Norton and C. Rouleau, "Synthesis of Novel Thin-Film Materials by Pulsed Laser," Science 273, 16 (1996).

7. Y. Zhao, A. R. Barman, S. Dhar, A. Annadi, M. Motapothula, J. Wang, H. Su, M. Breese, T. Venkatesan and Q. Wang, "Scaling of flat band potential and dielectric constant as a function of Ta concentration in Ta-TiO2 epitaxial films," AIP Advances 1, 022151-022159 (2011).

8. A. R. Barman, M. Motapothula, A. Annadi, K. Gopinadhan, Y. L. Zhao, Z. Yong, I. Santoso, Ariando, M. Breese, A. Rusydi, S. Dhar and T. Venkatesan, "Multifunctional Ti1−xTaxO2: Ta doping or alloying?" Applied Physics Letters 98, 072111 (2011).

9. B. E. Warren, "X-ray Diffraction," (Courier Dover Publications, 1969).

10. I. Robinson and R. Harder, "Coherent X-ray diffraction imaging of strain at the nanoscale," Nature Materials 8, 291-298 (2009).

11. http://en.wikipedia.org/wiki/X-ray_Diffraction

12. W. R. Bowen and N. Hilal, "Atomic Force Microscopy in Process Engineering: An Introduction to AFM for Improved Processes and Products," (Butterworth-Heinemann, 2009).

13. K. Lang, D. Hite, R. Simmonds, R. McDermott, D. Pappas and J. M. Martinis, "Conducting atomic force microscopy for nanoscale tunnel barrier characterization," Review of Scientific Instruments 75, 2726-2731 (2004).

14. K. Watanabe, T. Taniguchi and H. Kanda, "Direct-bandgap properties and evidence for ultraviolet lasing of hexagonal boron nitride single crystal," Nature Materials 3, 404-409 (2004).

15. A. Djurisic, Y. Leung, K. Tam, L. Ding, W. Ge, H. Chen and S. Gwo, "Green, yellow, and orange defect emission from ZnO nanostructures: Influence of excitation wavelength," Applied Physics Letters 88, 103107-103103 (2006).

16. A. Djurišić, Y. Leung, K. Tam, Y. Hsu, L. Ding, W. Ge, Y. Zhong, K. Wong, W. Chan and H. Tam, "Defect emissions in ZnO nanostructures," Nanotechnology 18, 095702 (2007).

17. K. Vanheusden, C. Seager, W. Warren, D. Tallant and J. Voigt, "Correlation between photoluminescence and oxygen vacancies in ZnO phosphors," Applied Physics Letters 68, 403 (1996).

18. D. Haranath, S. Sahai and P. Joshi, "Tuning of emission colors in zinc oxide quantum dots," Applied Physics Letters 92, 233113 (2008).

19. S. Sundaram and E. Mazur, "Inducing and probing non-thermal transitions in semiconductors using femtosecond laser pulses," Nature Materials 1, 217-224 (2002).

20. J. Q. Chen, X. Wang, Y. H. Lu, A. R. Barman, G. J. You, G. C. Xing, T. C. Sum, S. Dhar, Y. P. Feng, Ariando, Q. H. Xu and T. Venkatesan, "Defect dynamics and spectral observation of twinning in single crystalline LaAlO3 under subbandgap excitation," Applied Physics Letters 98, 041904 (2011).

21. X. Wang, J. Q. Chen, A. R. Barman, S. Dhar, Q. H. Xu, T. Venkatesan and Ariando, "Static and ultrafast dynamics of defects of SrTiO3 in LaAlO3/SrTiO3 heterostructures," Applied Physics Letters 98, 081916 (2011).

22. D. O'Connor, "Time-correlated single photon counting," (Academic Press, 1984).

23. P. P. Banerjee, "Nonlinear Optics: Theory, Numerical Modeling and Applications," Vol. 86 (CRC Press, 2003).

24. M. Sheik-Bahae, A. A. Said and E. W. Van Stryland, "High-sensitivity, single-beam n2 measurements," Optics Letters 14, 955-957 (1989).

25. R. DeSalvo, D. J. Hagan, M. Sheik-Bahae, G. Stegeman, E. W. Van Stryland and H. Vanherzeele, "Self-focusing and self-defocusing by cascaded second-order effects in KTP," Optics Letters 17, 28-30 (1992).

26. H. K. Tsang, C. Wong, T. Liang, I. Day, S. Roberts, A. Harpin, J. Drake and M. Asghari, "Optical dispersion, two-photon absorption and self-phase modulation in silicon waveguides at 1.5 uw wavelength," Applied Physics Letters 80, 416-418 (2002).

27. L. Deng, E. Hagley, J. Wen, M. Trippenbach, Y. Band, P. Julienne, J. Simsarian, K. Helmerson, S. Rolston and W. Phillips, "Four-wave mixing with matter waves," Nature 398, 218-220 (1999).

28. J. Valdmanis, R. L. Fork and J. P. Gordon, "Generation of optical pulses as short as 27 femtoseconds directly from a laser balancing self-phase

modulation, group-velocity dispersion, saturable absorption, and saturable gain," Optics Letters 10, 131-133 (1985).

29. R. W. Boyd, "Nonlinear optics," (Academic press, 2003).

30. L. Polavarapu, M. Manna and Q.-H. Xu, "Biocompatible glutathione capped gold clusters as one-and two-photon excitation fluorescence contrast agents for live cells imaging," Nanoscale 3, 429-434 (2011).

31. Y. H. Lee, Y. Yan, L. Polavarapu and Q.-H. Xu, "Nonlinear optical switching behavior of Au nanocubes and nano-octahedra investigated by femtosecond Z-scan measurements," Applied Physics Letters 95, 023105 (2009).

32. M. Sheikbahae, A. A. Said, T. H. Wei, "Sensitive measurement of optical nonlinearities using a single beam," IEEE J. Quantum Elect., 26, 760-769 (1990).

33. H. M. Gibbs, "Optical bistability: controlling light with light," Academic Press, (1985).

Chapter 3　　Defect Dynamics and Spectral Splitting in LaAlO₃

3.1 Introduction

The low microwave losses, good lattice matching with many common oxides (pseudo cubic a=3.79 Å), wide band gap (5.6 eV) and thermal stability have made LAO crystals a strategically important substrate.[1-4] The optical characteristics in the infrared and microwave regions have been widely studied for the rare-earth LAO on account of their deployment in the fabrication of high temperature superconductor based microwave devices.[5-7] More recently there has been resurgence in the interest in LAO due to the observation of a quasi 2DEG at the interface of LAO and STO crystals for the polar nature of LAO and the requirements to avoid a polarization catastrophe.[8] LAO exhibits a cubic to rhombohedral phase transition at 820 K and at temperatures below this value the crystal develops twins.[9] The twinning could result in the formation of crystalline domains where the cations may be displaced from their equilibrium sites. Such displacements could potentially affect the electronic energy levels which may show up in various spectroscopic measurements. Recent observations of resistive switching in oxides, high mobility electrons, unusual magnetic phenomena at the LAO/STO interfaces underscore the role of defects within the band gap of these oxides and the need for careful characterization of these defects, namely their location, energy width and electron life times.[10-12] TA and PL in the picosecond to femtosecond time scale are powerful tools to study the dynamic coupling of electron and lattice, and detect localized defect states for wide band gap

crystals, such as STO and LAO.[13,14]

Based on PL and TA, many interesting carrier dynamics studies have been reported for the doped and undoped STO.[15-17] However, as far as we know, few ultrafast dynamic and PL studies have been reported on LAO crystals.[18,19] Kawabe et al. found that under 266 nm excitation there were two distinct components, a fast UV one arising from band-band excitation and a broad component involving oxygen defect levels.[18] Kanai et al. found these by using 248 and 193 nm excitation, a series of five different PL peaks which were associated with defect levels inside the gap.[19] In both papers, the electrons were pumped to the conduction band and the resultant PL was dominated by emission from conduction band to various defect levels. Under this condition, the PL spectrum was dominated by broad peaks with very little distinguishable features.

In this chapter, we investigate the dynamics of electron relaxation and defect PL from single crystal LAO, by using sub-bandgap excitation (400 nm) which selectively probes certain defect levels reveal features not seen in the previous studies. We see consistent doublet features on more than one PL peaks and we believe this to arise from the twin splitting of the defect energy band, which in turn enables us to estimate the size of the cationic displacements within the twins in LAO.

3.2 Experimental Procedure

In this study, doubly polished (100) LAO single crystals [Crystec GmbH], 1×1 cm in size, 0.5 mm thick were used as received. The detail of the femtosecond TA and pump probe experiments were explained in chapter 2. To eliminate the effect of the probe light excitation the power intensity ration between the

pump and probe is kept at more than 20, in all experiments. All the time-resolved experiments were performed at room temperature. The temperature dependent PL experiments were carried out by using the same 400 nm laser excitation source. The PL signal was collected through a Princeton Instruments SP 2300i Spectrometer with a CCD detector. The spectral resolutions were 0.14 nm for PL measurement and 5 nm for TA measurements. The UV-visible transmittance spectrum of the LAO crystal was measured using a Shimadzu UV-Vis-NIR spectrometer with a wavelength range from 240 to 2600 nm.

3.3 Results and Discussion

3.3.1 Photoluminescence of pure LAO

The UV-visible transmittance spectrum shown in Fig. 3.1 indicates that LAO has an optical bandgap of 5.6 eV. The high and flat transmission at the longer wavelength range indicates the intrinsic purity of this material, where only bandgap absorption is observed in the static spectrum. As reported, some defect levels are formed by oxygen vacancies and impurities within the bandgap. Those defect levels are usually related to the small amount of impurities and trapped states. For the UV spectrum the signals are dominated by the ground state absorption, thus the defect levels are hardly to identify.
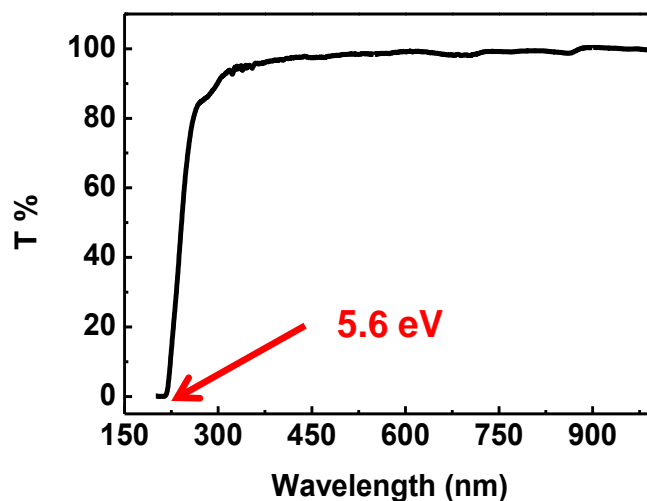
Figure 3.1. UV-visible transmittance spectrum of as received LAO (100) single crystal. The arrow indicates the bandgap of 5.6 eV.

In order to study the behavior of the intra-bandgap defect levels, we have measured the temperature dependent PL spectrum. In Fig. 3.2 (a), three distinct peaks were observed in the PL spectrum, a broad peak at high photon energies from 550-650 nm and two sharp peaks at lower photon energy centered at 699 and 726 nm. Both sharp peaks show a doublet splitting of ~6 nm. The splitting is also likely to be present in the peak centered at 600 nm but is not observable due to the peak broadening. As the photon energy of the 400 nm excitation is 3.1 eV, which is below the band gap of LAO (5.6 eV), the electrons can reach the conduction band only via a multi-photon process. Under this situation the PL intensity should increase nonlinearly with increaseing excitation intensity. However, Fig. 3.2 (b) clearly shows that the PL intensities at three different wavelengths follow a linear dependence on the excitation intensity. The linearity suggests that PL arises from the electron of the valence band excited to some intermediate defect levels followed by decay

51

down to various lower defect levels. The PL intensities at 726 and 699 nm increase with the temperature, while the PL intensity for the broad spectrum from 550 to 650 nm decreases linearly with the temperature. This interesting effect indicates that the PL for the broad spectrum and the two sharp peaks originate from different electronic processes.
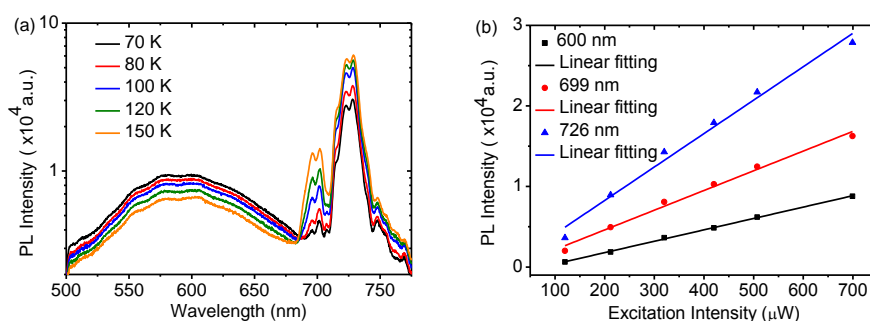
Figure 3.2. (a) Photoluminescence data for LAO crystal at different temperatures under 400 nm laser excitation, (b) Photoluminescence intensity at 600, 699 and 726 nm under different excitation intensities at room temperature.

This is better illustrated in Fig. 3.3 where we have taken the calculated defect levels from Lou et al.[20] and have matched the observed PL with possible energy levels. The broad peak at 600 nm is likely due to the electronic transition from singly charged oxygen interstitial defect levels to valence band; the 726 nm peak is likely due to La interstitial and/or the Al antisite at the La position to the valence band. The different temperature dependences of these peaks may be related to the relative temperature redistribution of the density of the defects. With increasing temperatures, one would infer from this data an increase in the La interstitial and/or the Al antisite at the La position defects and a decrease of oxygen interstitial.
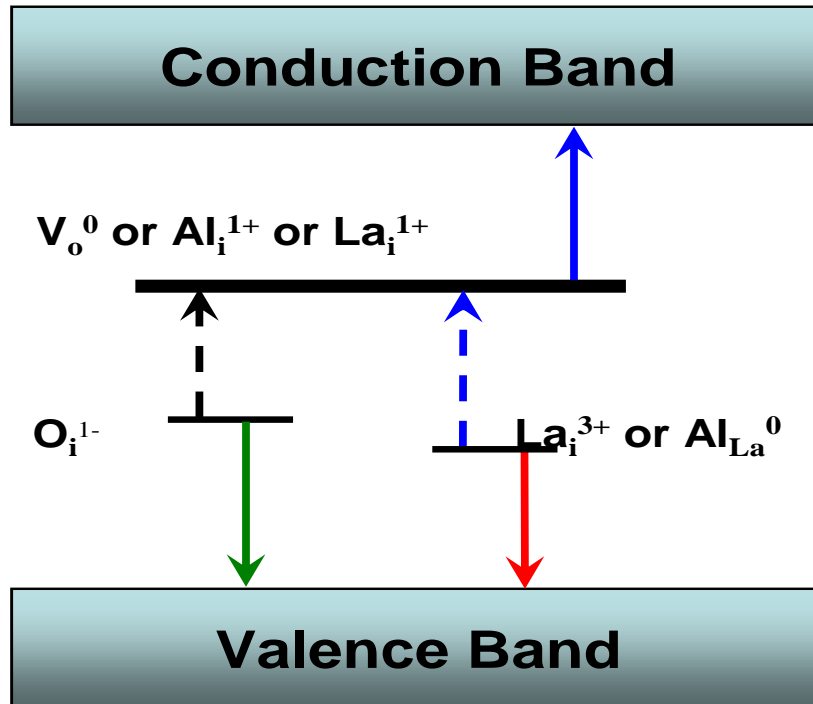
Figure 3.3. Illustration for the possible origin of the photoluminescence (down arrow) and the transient absorption (up arrow) peaks with the calculated defect levels from Lou et al.[20]

The spectral splitting of the peaks at 699 and 726 nm is quite interesting and may be related to the twin formation in LAO. At around 820 K, LAO undergoes a transition from a high temperature cubic phase to a low temperature orthorhombic phase with a rhombohedral primitive unit cell through a Pm3m↔R3c octahedral tilting.[21] This symmetry breaking transition leads to a buildup of high stress in the crystal which is relieved by the formation of eight energetically equivalent domain states, of which there are only four macroscopically observable twins. Any pair of the four twin states have twin boundaries along the (100) or (110) planes. However, it has been found that the (100) twins are energetically more favorable than the (110)

twins due to less strain. [22] These twin states may have significant displacement of the cations from their equilibrium sites which may affect the electronic energy levels. To shed more light on the effect of this cation displacement, first-principle calculations based on density functional theory (DFT) are employed for the position of energy level in the bandgap. The DFT calculations include the generalized gradient approximation, using a plane wave basis (kinetic energy cut-off 400 eV) and projector augmented-wave pseudo potential.[23,24] One oxygen atom was removed from $3 \times 3 \times 3$ supercell to model the oxygen vacancy defect in LAO. This defect level was found at around 2.23 eV above valence band maximum (VBM) (without shifting the Al or La). When the Al atom was shifted from the original site with the other atoms in their original sites, the position of the defect level changed significantly. The defect level shifted about 15 meV from original position when the Al atom was displaced 0.09 Å from the original site (Fig. 3.4), while a similar displacement at the La site did not lead to any significant shift of the defect level. Hence the twinning could result in two different Al sites, one shifted and the other not, leading to the observed 6 nm splitting in the defect PL.
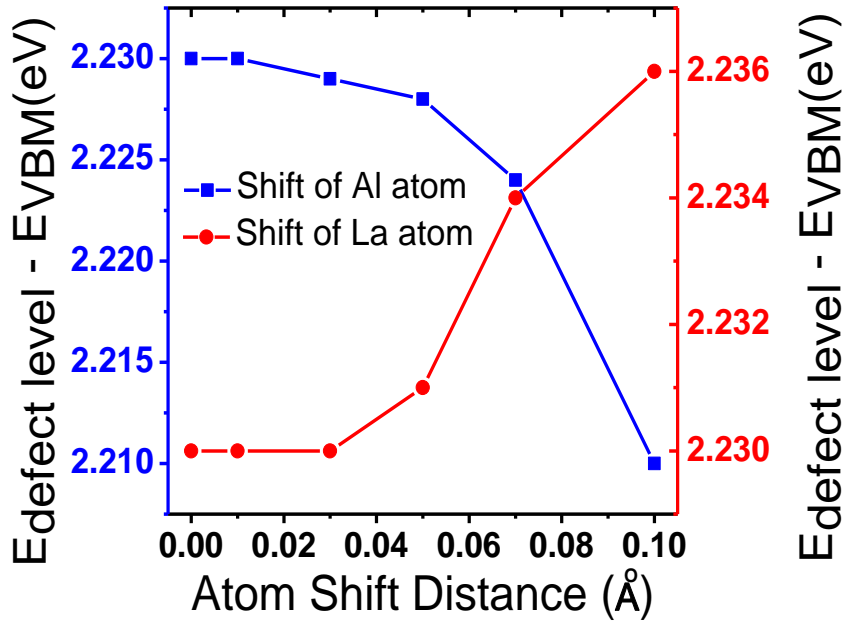
Figure 3. 4. First principle calculated defect levels with shifting Al and La atoms.

3.3.2 Oxygen-vacancy-dependent photoluminescence

As discussed above, the defect levels in the band gap contribute to the PL spectrum. From the PL spectrum, we can observe that there are at least two types of defects in the LAO crystal. The oxygen interstitials contribute to the broadened spectrum centered at a wavelength of around 600 nm. The La interstitial and/or Al antisite at the La position contribute to the two sharp peaks. These two types of defects behave quite differently with temperature. To further study this behavior in detail, we annealed the LAO crystal at different oxygen pressures, which can change the oxygen vacancy concentration in the sample and this may help in understanding the effect of the oxygen vacancy and interstitial defects on the PL.

We have prepared three samples under different annealing conditions to introduce different concentrations of oxygen vacancies. Sample (a) is the as received single crystal that acts as the reference. Sample (b) is annealed at 1 atm oxygen pressure under 973 K for 1 h. Sample (c) is annealed at 1×10^{-2} Torr oxygen pressure under 973 K for 1 h. Figure 3.5 shows the room temperature PL spectrum for three samples prepared under different oxygen background pressures and hence with different oxygen vacancy concentrations.

To compare the PL intensity, we normalized the PL spectrum at 800 nm, which is the second-order grating diffraction and it is proportional to the incident laser intensity. The PL results show that the as received LAO single crystal has the highest PL intensity. It is noted that sample (b) has more oxygen interstitials and sample (c) has less oxygen interstitials than the as received sample (a); however, after annealing, the PL intensities for both samples (b) and (c) are suppressed. As mentioned before, the LAO crystal shows a crystal phase transition at ~820 K. It should be noted that the annealing temperature is 973 K, which is higher than this phase transition temperature. During the annealing process, this phase transition may introduce a lattice distortion and further introduce more defect states into the crystal; most of these defects become recombination centers and increase the nonradiative decay process, resulting in the reduction of the PL intensity.
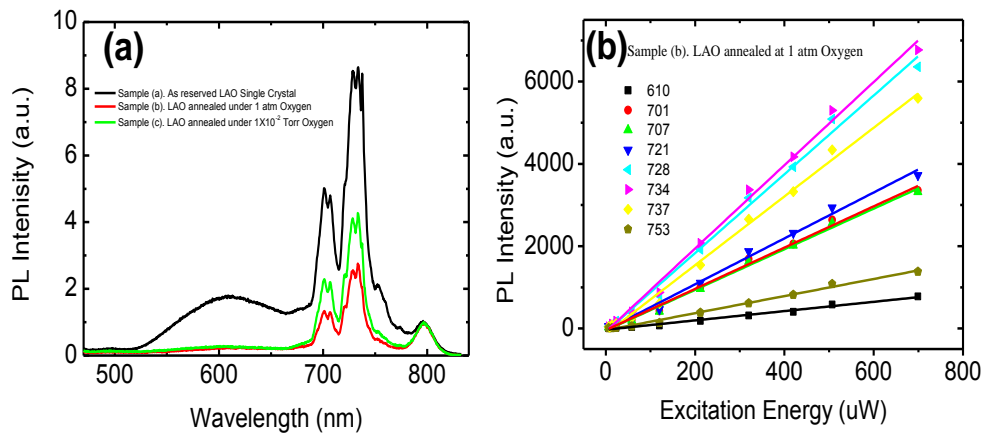
Figure 3.5. (a). Room temperature PL of LAO under different annealing conditions. Sample (a) is the as reserved LAO single crystal; sample (b) is the LAO single crystal annealed at 973 K under 1 atm pressure for 1 h; sample (c) is the LAO single crystal annealed at 973 K under 1×10^{-2} Torr oxygen pressure for 1 h; (b). Power dependence in sample (b) (LAO single crystal annealed at 973 K under 1 atm oxygen pressure for 1 h), all wavelengths showed linear dependence with excitation power.

3.3.3 Transient absorption and relaxation time determination

The transient absorption spectra of the defect dynamics for the LAO crystal under excitation at 400 nm at the room temperature are shown in Fig. 3.6. Two transient absorption bands at 620 and 760 nm were observed at different excitation intensities. It is interesting to note that the two bands behave differently with the time. The transient absorption band at 620 nm under a high excitation intensity (270 nJ/pulse) decays with two different time scales, a fast decay with a time constant of 4 ps followed by a slow decay with time constant over 1 ns. However, the transient absorption band at 760 nm only shows one slow decay component. This difference in the time evolution behaviors indicate that the 620 and 760 nm bands originate from different electronic processes. Figure. 3.6(b) shows excitation intensity dependent

transient spectra at a time delay of 2.0 ps. The excitation intensity dependence indicates a hybrid of one- and two-photon excitation processes with a larger two photon component for the 620 nm band (power of 1.6) than the 760 nm band (power of 1.4). As the excitation intensity increases, amplitude of the fast decay components for 620 nm band also increases. The two-photon excitation at high excitation intensities will promote the electrons onto the conduction band. The initial decay from the conduction band to upper defect level is believed to be very fast (~100 fs and not observed in our data), which is followed by decay to lower defect level with a time constant of 4 ps and subsequent decay back to valance levels with a slow decay components (>1 ns). Figure 3.6 shows that the relaxed transient spectra at 30 ps became similar to the initial (e.g. at 2 ps) transient spectra under lower excitation intensities. The one-photon excitation (which will dominate at the low excitation intensity) can only promote electrons to the mid-gap defect level.

The energy diagram is depicted in Fig. 3.3. The black and blue arrows are indicators for the TA peaks. Black arrow indicates the 760 nm TA peak, and the blues indicates the 620 nm TA peak. The 620 nm band arises from two different electronic transitions, the first one from the upper defect level to the conduction band absorption with a short decay time constant (4 ps) and the second from the lowest defect levels to the upper gap defect level excitations with a slow decay time constant (> 1 ns). The 760 nm transient absorption is from the lowest defect levels to the upper defect level with a slow time constant. Hence this confirms that the upper defect level centered at 3.1 eV has a fast electron decay time (~4 ps) while the two lower defect levels centered at 2.1 and 1.7 eV have a long (>1 ns) decay time. It is indeed surprising that for such large variations in the decay time of these defect levels

and stresses the need for their detailed characterization.
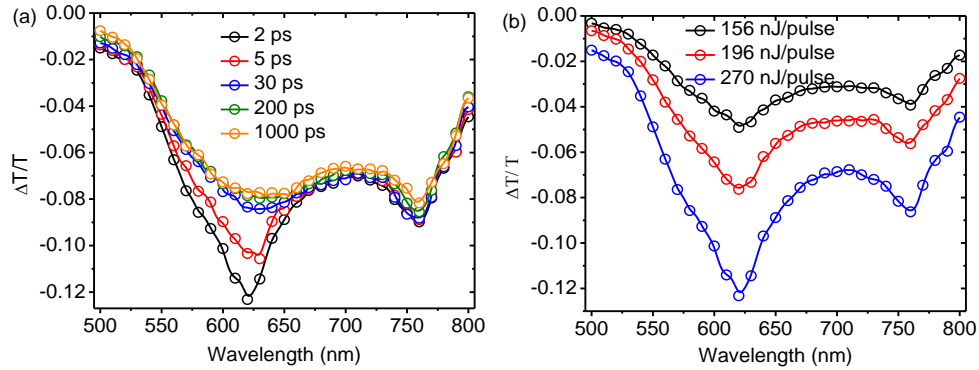
Figure 3.6. (a) Transient absorption spectra for the single LAO crystal under 270 nJ/pulse 400 nm femtosecond laser excitation at room temperature. (b) Transient absorption spectra under different excitation intensity with 2 ps delays time.

3.4 Conclusions

The study of wide bandgap oxides and the defects lying within the bandgap may be better studied by using sub-bandgap excitation rather than a band to band excitation. We have shown this to yield exciting new data for the case of LAO where a doublet splitting is seen in the various defect levels with different dynamics processes. These splitting give us an idea of the cationic displacements in LAO as a result of structural phase transitions which are responsible for the commonly observed twins in this system. The fs pump probe studies are able to distinguish the widely differing electronic lifetime of the various defect levels. Hence PL and optical pump probe spectroscopic techniques can shed new information on these wide band gap materials.

Bibliography

1. R. W. Simon, C. E. Platt, A. E. Lee, G. S. Lee, K. P. Daly, M. S. Wire and J. A. Luine, "Low‑loss substrate for epitaxial growth of high‑temperature superconductor thin films," Applied Physics Letters 53, 2677-2679, (1988).

2. S. X. Zhang, D. C. Kundaliya, W. Yu, S. Dhar, S. Y. Young, L. G. Salamanca-Riba, S. B. Ogale, R. D. Vispute and T. Venkatesan, "Niobium doped TiO2: Intrinsic transparent metallic anatase versus highly resistive rutile phase," Journal of Applied Physics 102, (2007).

3. W. L. Wang, C. Y. Peng, Y. T. Ho and L. Chang, "Microstructure of a-plane ZnO grown on LaAlO3 (001)," Thin Solid Films 518, 2967-2970, (2010).

4. A. Boudali, B. Amrani, M. D. Khodja, A. Abada and K. Amara, "First-principles study of structural, elastic, electronic, and thermal properties of LaAlO3 perovskite," Computational Materials Science 45, 1068-1072, (2009).

5. J. Demsar, A. Gozar, V. K. Thorsmolle, A. J. Taylor and I. Bozovic, "Long-lived near-infrared photoinduced absorption in LaSrAlO4 excited with visible light," Physical Review B 76, (2007).

6. Q. Wan, Y. P. He, N. Dai and B. S. Zou, "Eu3+-doped LaPO4 and LaAlO3 nanosystems and their luminescence properties," Science in China Series B-Chemistry 52, 1104-1112, (2009).

7. X. H. Zeng, L. H. Zhang, G. J. Zhao, J. Xu, Y. Hang, H. Y. Pang, M. Y. Jie, C. F. Yan and X. M. He, "Crystal growth and optical properties of LaAlO3 and Ce-doped LaAlO3 single crystals," Journal of Crystal Growth 271, 319-324, (2004).

8. A. Ohtomo and H. Y. Hwang, "A high-mobility electron gas at the LaAlO3/SrTiO3 heterointerface," Nature 427, 423-426, (2004).

9. M. A. Carpenter, S. V. Sinogeikin, J. D. Bass, D. L. Lakshtanov and S. D. Jacobsen, "Elastic relaxations associated with the Pm(3)over-barm-R(3)over-barc transition in LaAlO3: I. Single crystal elastic moduli at room temperature," Journal of Physics-Condensed Matter 22, (2010).

10. Z. Q. Liu, D. P. Leusink, W. M. Lü, X. Wang, X. P. Yang, K. Gopinadhan, Y. T. Lin, A. Annadi, Y. L. Zhao, A. R. Barman, S. Dhar, Y. P. Feng, H. B. Su, G. Xiong, T. Venkatesan and Ariando, "Reversible metal-insulator transition in LaAlO3 thin films mediated by intragap defects: An alternative mechanism for resistive switching," Physical Review B 84, 165106 (2011).

11. M. Basletic, J. L. Maurice, C. Carretero, G. Herranz, O. Copie, M. Bibes, E. Jacquet, K. Bouzehouane, S. Fusil and A. Barthelemy, "Mapping the spatial distribution of charge carriers in LaAlO3/SrTiO3 heterostructures," Nature Materials 7, 621-625, (2008).

12. Ariando, X. Wang, G. Baskaran, Z. Q. Liu, J. Huijben, J. B. Yi, A. Annadi, A. R. Barman, A. Rusydi, S. Dhar, Y. P. Feng, J. Ding, H. Hilgenkamp and T. Venkatesan, "Electronic phase separation at the LaAlO3/SrTiO3 interface," Nat. Commun. 2, (2011).

13. Y. Yamada, H. Yasuda, T. Tayagaki and Y. Kanemitsu, "Photocarrier recombination dynamics in highly excited SrTiO3 studied by transient absorption and photoluminescence spectroscopy," Applied Physics Letters 95, (2009).

14. D. Hreniak, W. Strek, P. Deren, A. Bednarkiewicz and A. Lukowiak,

"Synthesis and luminescence properties of Eu3+-doped LaAlO3 nanocrystals," Journal of Alloys and Compounds 408, 828-830, (2006).

15. Y. Yamada, H. Yasuda, T. Tayagaki and Y. Kanemitsu, "Temperature Dependence of Photoluminescence Spectra of Nondoped and Electron-Doped SrTiO3: Crossover from Auger Recombination to Single-Carrier Trapping," Physical Review Letters 102, (2009).

16. A. Rubano, D. Paparo, F. M. Granozio, U. S. di Uccio and L. Marrucci, "Blue luminescence of SrTiO3 under intense optical excitation," Journal of Applied Physics 106, (2009).

17. D. S. Kan, T. Terashima, R. Kanda, A. Masuno, K. Tanaka, S. C. Chu, H. Kan, A. Ishizumi, Y. Kanemitsu, Y. Shimakawa and M. Takano, "Blue-light emission at room temperature from Ar+-irradiated SrTiO3," Nature Materials 4, 816-819, (2005).

18. Y. Kawabe, A. Yamanaka, E. Hanamura, T. Kimura, Y. Takiguchi, H. Kan and Y. Tokura, "Photoluminescence of perovskite lanthanum aluminate single crystals," Journal of Applied Physics 88, 1175-1177, (2000).

19. K. Kanai, E. Hirata and Y. Ohki, "Photoluminescence Analysis of Czochralski-Grown Lanthanum Aluminate Single Crystals," Japanese Journal of Applied Physics 47, 7980-7982, (2008).

20. X. Luo, B. Wang and Y. Zheng, "First-principles study on energetics of intrinsic point defects in LaAlO3," Physical Review B 80, (2009).

21. S. Bueble, K. Knorr, E. Brecht and W. W. Schmahl, "Influence of the ferroelastic twin domain structure on the {100} surface morphology of LaAlO3 HTSC substrates," Surface Science 400, 345-355, (1998).

22. C. H. Kim, J. W. Jang, S. Y. Cho, I. T. Kim and K. S. Hong, "Ferroelastic

twins in LaAlO3 polycrystals," Physica B 262, 438-443, (1999).

23 . J. P. Perdew, K. Burke and M. Ernzerhof, "Generalized gradient approximation made simple," Physical Review Letters 77, 3865-3868, (1996).

24. P. E. Blochl, "Projector augmented-wave method," Physical Review B 50, (1994).

Chapter 4   Fine Structure of Defect States in SrTiO₃

4.1 Introduction

In the field of oxide electronics, STO is a very important and strategic material, much like silicon is in the field of microelectronics. In recent times, STO has attracted increased attention owing to the observation of a quasi 2DEG at its native surface as well as the LAO/STO interface.[1-8] Recent PL measurements in low energy argon ion irradiated STO has emphasized the role of defects states in STO. Hence it is essential to understand the defect states (radiative versus non-radiative, lifetime of carries in these higher energy levels) of STO to realize its widespread utilization as a substrate and as an overlayer for a variety of opto-electronic device applications. To this extent recently, many studies have focused on defects in STO using PL and time-resolved measurements.[9-19] Most such techniques use above-bandgap excitations and show broad band and featureless PL spectra. In a prior study of the LAO/STO interface, we were able to map out the defect states induced by oxygen vacancy in a sample being annealed in vacuum to enhance the oxygen vacancy concentration.[19] In this study, we compare both above- and below bandgap excitation PL spectra with TA spectroscopy in as received STO without vacuum annealing to minimize oxygen vacancy signals. Unlike the featureless broad band PL spectra as seen in prior measurements, the TA spectra exhibited distinct spectral features arising from previously unobserved defect levels originating not just from oxygen vacancies. By using this approach, we have identified several important defect levels within the bandgap of STO and measured their lifetime as well.

In this chapter, doubly polished (100) STO single crystals (Crystec GmbH, Berlin Germany) of 1×1 cm size and 0.5-mm thickness were used as received. As mentioned earlier, in the case of the procured STO single crystal, we focused on the defect concentration in bare STO that was not subjected to any annealing or reduction.

4.2 Experimental Procedure

The details of the Z-Scan, PL and TA experiments are presented in chapter 2. 800-nm excitation PL experiments were carried out using the same femtosecond laser as the excitation source. The 350-nm above-bandgap excitation PL was carried out using an optical parametric amplifier system, and the PL signal was collected through an Acton SP 2300i monochromator (Princeton Instruments) coupled with a CCD detector. All experiments were performed at room temperature.

4.3 Results and Discussion

Figure 4.1 shows the UV-Vis transmission spectrum of the STO (100) single crystal. The sharp decrease in transmission indicates the bandgap of 3.2 eV (387 nm). Unlike our previous study on vacuum annealed STO there are no visible defect states in the gap indicating a very low oxygen vacancy concentration. We studied the PL and TA by using the following excitation photon energies: above-bandgap excitation, 3.54 eV (350 nm); sub-bandgap excitation, 3.1 eV (400 nm); and below-bandgap excitation, 1.55 eV (800 nm).
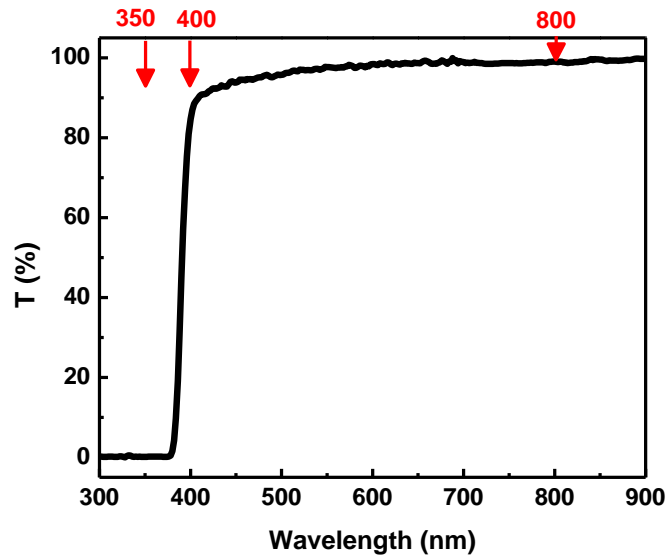
Figure 4.1. UV-Vis transmission spectrum of the STO (100) single crystal. The three arrows indicate the three wavelengths above bandgap, 350 nm; sub-bandgap, 400 nm; and below bandgap, 800 nm for the TA studies.

4.3.1 Multi-photon excitation PL of STO

Multi-photon absorption/excitation has been widely used in many chemical and biological studies. In these experiments, a long-wavelength source is usually used because it has high penetration depth and can obtain information from deep within a material. Another advantage of multi-photon experiments is that owing to the energy density threshold, higher-order absorptions only occur at a hot spot where the energy density is high enough to allow simultaneous multi-photon absorption to occur. Thus far, no studies have investigated the multi-photon excitation PL of STO. As shown in the z-scan experiment in Fig. 4.2, the two photon absorption coefficient of STO is 7.3×10^{-13} cm/W, which suggested that the STO can absorb the 800 nm photons through the multi-photon excitation process. From the band structure of STO, a two photon absorption falls short of the conduction band by about 100 meV.

66

Hence most of this absorption takes place in a defect level just below the conduction band edge. However, for reasons mentioned below, most of the decay from this level is not through PL in the visible region.

Next we studied the nonlinear excitation PL of single-crystal STO by using an 800-nm femtosecond laser as the excitation source when bright blue PL emission is observed at room temperature. Figure 4.3 shows this PL of single-crystal STO under multi-photon excitation using 800-nm femtosecond laser pulses. A broad luminescence peak centered at 2.7 eV was observed. The linear absorption spectra showed strong absorption at the band gap energy of 3.2 eV (dashed line in Fig. 4.3 (a)). As the excitation photon energy was 1.55 eV, the valence band electron can only be excited to the conduction band by a multi-photon excitation process (~ a three photon process), as evidenced by the power-dependent PL data (Fig. 4.3 (b)) with a slope of 2.7. Similar to recently reported data, the spectra are dominated by transitions from the conduction band to some broad defect energy levels.[9-14] Figure 4.3 (c) shows a photograph of the PL of STO under intense 800-nm femtosecond pulse laser excitation that can be clearly seen by the naked eye. While the absorption of the 800 nm photons is dominated by two-photon absorption, the PL emission is dominated by a three photon process. This tells us that the PL is dominated by decay of excited electrons from the conduction band to the various lower lying defect states, while the absorption is dominated by the below bandgap defects states whose contribution to the visible PL is negligible.
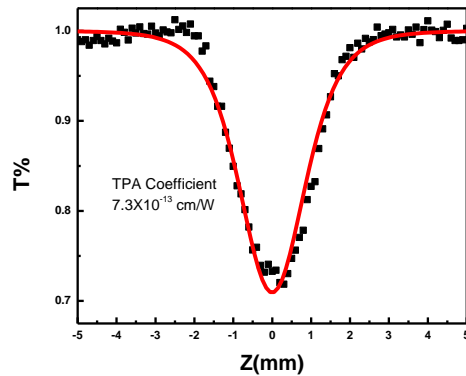
Figure 4.2. Z-Scan measurement for the two photon absorption coefficient of STO single crystal, with the 800 nm fs pulse (30 mJ/cm^2). The fitting result shows the two photon absorption coefficient of 7.3x10^{-13} cm/W.
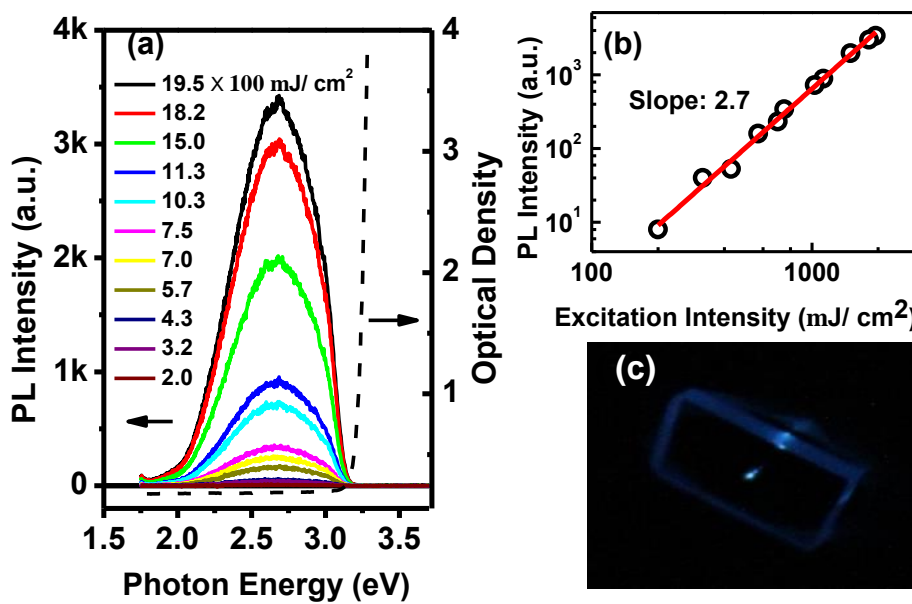
Figure 4.3. (a) 800-nm femtosecond laser pulse (photon energy: 1.55 eV) excitation emission spectra of single-crystal STO with different pump powers, where the dashed line indicates the UV-Vis absorption spectrum of STO. (b) Log-log plots of the peak intensities of the blue emission from STO versus excitation intensity. The solid line indicates the power fitting with a slope of 2.7. (c) Photograph of blue emission from STO under multi-photon excitation of 800-nm femtosecond laser pulse.

4.3.2 One-photon above-bandgap excitation PL of STO
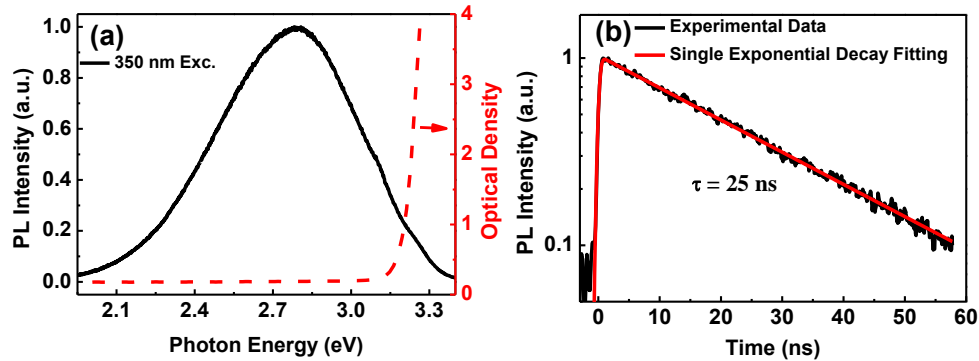
Figure 4.4. (a) Above-bandgap (350 nm; 3.5 mJ/cm^2) excitation PL of STO. (b) PL dynamics for STO under 350-nm excitation.

To further identify the origin of PL excitation, we used 350 nm (3.54 eV) (above-bandgap) excitation as the source for investigating the PL properties. Figure 4.4 shows the PL of single-crystal STO under above-bandgap excitation. The increased absorption spectra showed strong absorption at a bandgap energy of 3.2 eV (dashed line in Fig. 4.4 (a)). There was a large shift (~0.4 eV) between the absorption and the emission peaks. This shift indicated that the broad optical emission must be attributed to the de-excitation from the bottom of the conduction band to a number of defect levels above the valence band maximum. The long PL lifetime of ~25 ns indicated that the lifetime of electrons in the conduction band is very long. It should be noted that this 350-nm above-bandgap excitation PL has a similar emission structure as the 800-nm multi-photon excitation, further supporting the fact that the 800 nm excitation shown in Fig. 4.3 is a nonlinear process that excites electrons to the conduction band.

Despite several studies focusing on the PL properties of STO, the details of the emission centers remain unclear.[9-21] For the above-bandgap excitation, the electrons are promoted to levels above the conduction band from where they

relax to the bottom of the conduction band via electron-phonon scattering with subsequent emission from the bottom of the conduction band. The PL seems to arise from the recombination of electrons from the conduction band with defect levels centered 0.4 eV above the valence band with a bandwidth of 0.7 eV.

4.3.3 Transient absorption and defect dynamics

Both the above- and sub-bandgap excitation PL show broad emission spectra and hence no detail information is available about the discrete defect energy levels that are expected to be present in this system from such optical measurements.[13-15,18-21] Further studies of the fast decay processes in the picosecond and sub-picoseconds range generally use TA spectroscopy, which can provide information about all the optically active processes including radiative and non-radiative carrier decay.

Figure 4.5 shows the transient absorption spectrum of STO under 350-nm above-bandgap excitation. A strong induced absorption peak at 1.8 eV was observed; decay dynamics shows that this peak has a long lifetime in the nanosecond range. A weak induced absorption peak at 2.1 eV was also observed, which indicates close band defect state absorption. The 350-nm excitation has photon energy (3.54 eV) greater than the STO bandgap (3.2 eV), it has a short penetration depth because most photons are absorbed within a depth of a hundred nanometers from the surface. The TA signal is mostly contributed by the few 100 nm surface region. During this above-bandgap excitation process, the electrons in the valence band are promoted to the conduction band, and these excited electrons have a long decay time and account for the induced absorption observed through the TA spectrum.

The probe photon energy dependent transmission modulation shown in Fig. 4.5 indicates a step at around 2 eV. This can be interpreted as due to transitions from the conduction to defect levels at about 2 eV above the valence band. Between 2-2.8 eV above the valence band, there seems to be very few defect levels. Closer inspection reveals a small dip about 2.2 eV and at about 1.8 eV. The pump probe signal for this wavelength is handicapped by the short penetration depth of the pump beam and its limited overlap with the probe beam. We hence studied the TA using 800 nm as the excitation wavelength where the penetration depth and laser intensity were much higher and the probe overlap was also much stronger.
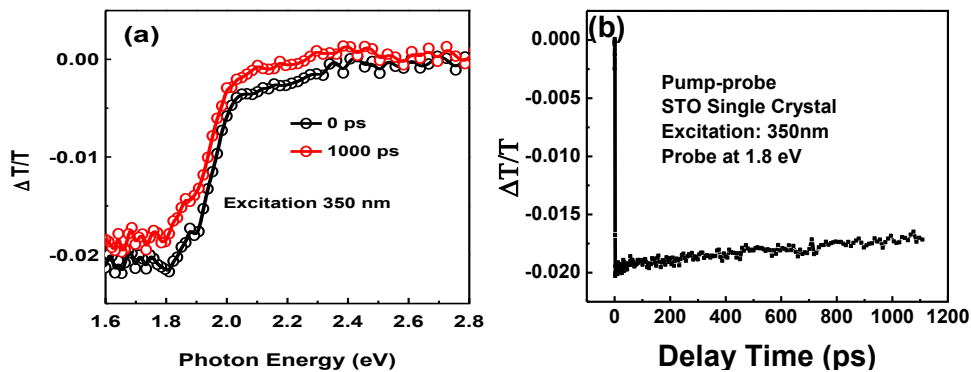
Figure 4.5. (a) Transient absorption spectra for above-bandgap (350 nm; 10 $\mu J/cm^2$) excitation. (b) Decay dynamics of the photon induced absorption probed at 1.77 eV under 350-nm (10 $\mu J/cm^2$) excitation.

Figure 4.6 shows the TA of the STO under 800-nm excitation. As shown before, under high excitation intensity, 800-nm excitation can excite electrons to the conduction band via multi-photon absorption. To only excite defect-level electrons, we have kept low excitation intensity so that only linear excitation can happen. The power-dependent data in Fig. 4.6 (a) shows linear fitting, indicating only one-photon excitation process and only the defect

states in between the bandgap have been excited. Two well defined absorption peaks located at 1.65 and 2.1 eV were observed in Fig. 4.6 (b). It is shown that all these defect states show the slow decay process in the nanosecond range after being excited by the 800-nm photons. One of the interesting points is the absence of a peak at 2.8 eV which will correspond to the peak in the defect density of states to which the conduction band electrons decay down to. So this tells us that these defect levels measured are radiatively forbidden with respect to the conduction band. Thus we are able to map out the defect levels which do not satisfy the selection rule for optical transition.
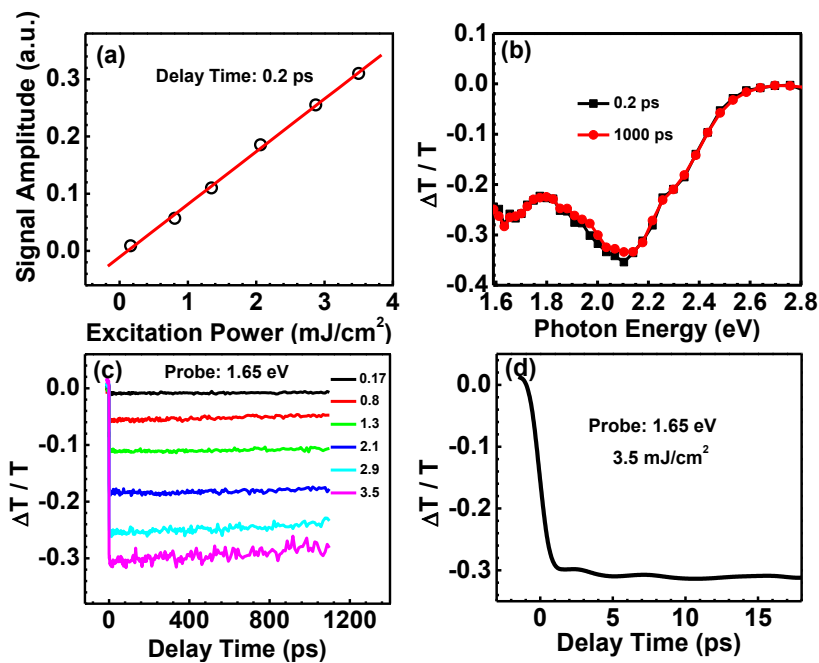
Figure 4.6. (a) Transient absorption spectra for below-bandgap (800 nm; 3.5 mJ/cm^2) excitation. (b) Power-dependent data for probe wavelength at 1.65 eV at delay time of 0.2 ps. The solid line shows the linear fitting. (c) Decay dynamics of photon-induced absorption probed at 1.65 eV under 800 nm excitation with different excitation intensity. (d) Initial decay dynamics for probe wavelength at 1.65 eV within 18 ps for 800 nm excitation.

Next we study 400-nm excitation, which has a photon energy of 3.1 eV that is just below the bandgap of STO (3.2 eV), and excites the defect levels just below (0.1 eV) the conduction band very efficiently. From this defect level, there would be transitions to the lower defect levels. By excitation to this defect level, one can populate lower defect levels, which could be observed by TA measurements.

Figure 4.7 shows the TA spectra under 400-nm femtosecond laser excitation. Five absorption peaks were observed (E–J in Fig. 4.7 (a)). One-photon excitation is confirmed in Fig. 4.7 (b), where a power law of 1.0 is seen for the TA signal versus the excitation density. These defects (E–J in Fig. 4.7 (a)) have very short lifetime of < 2 ps, as shown in the case of the peak centered at 2.1 eV that has a lifetime of 1.7 ps in Fig. 4.7 (c) and its inset. At longer delay times these short-lived peaks (E–J in Fig. 4.7 (a)) disappear and two long-lived broader peaks (L and M in Fig. 4.7 (d)) with lifetime in the nanosecond range remain.

It is intriguing that only the 400-nm excitation shows the fast decay process. Furthermore, there is no observable PL signal in this case, indicating all the transitions to be non-radiative. The speed of this fast non-radiative signal implies that the defects (both excited and ground states) are closely related to the same atomic species where a strong electron-phonon coupling may be possible, leading to the short lifetime. For example, the defect level just below the conduction band has been associated with oxygen vacancy and hence it seems reasonable to assume that the defect centered at 1.1 eV above the VB may also be related to oxygen vacancy. The non-radiative transitions occur to ground states that are centered at 0.7, 0.95, 1.1, 1.35 and 1.55 eV above the valence band with defect band widths between 0.1-0.2 eV. But in a time scale

of nanoseconds, the electrons decay down to two trap states centered at 1.1 and 1.55 eV with extremely long life time beyond our TA capability of 1.2 ns. The defect levels seem to merge and broaden under electron excitation condition as seen in Fig. 4.7 (d).
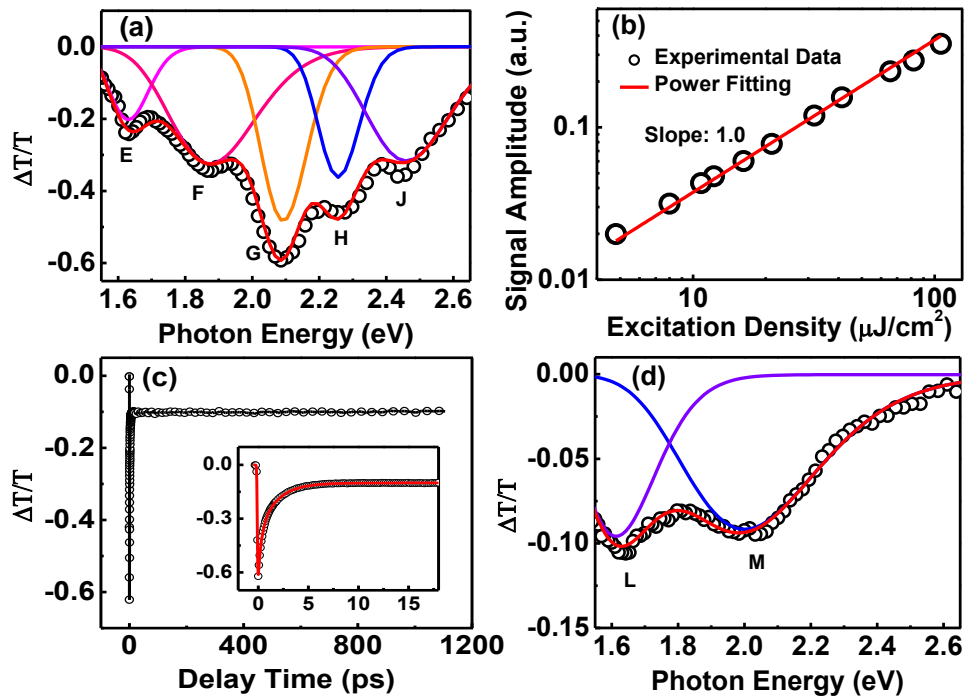
Figure 4.7. (a) TA spectra of STO at delay time of 0 ps under 400-nm (160 μJ/cm^2) excitation. Circles indicate experimental data and solid lines, multi-peak Gaussian fitting results. (b) Peak amplitude of the transient signal at 2.1 eV (open circles) versus excitation power (delay time of 0 ps). The solid line indicates power fitting with a slope of 1.0. (c) Decay dynamics of the photon-induced absorption probed at 2.1 eV under 400-nm (160 μJ/cm^2) excitation. The inset shows the initial decay dynamics within 18 ps. (d) TA spectra of STO at delay time of 1000 ps under 400-nm (160 μJ/cm^2) excitations.

Figure 4.8 summarizes the electron dynamics of the STO under the sub-bandgap and band edge excitations. For 350-nm above-bandgap excitation, the valence band electrons are promoted to the conduction band, from where they quickly relax to the bottom of the conduction band and they

decay predominantly to a set of defect levels centered 0.4 eV above the valence band with a bandwidth of 0.7 eV. For the PL, these defect bands must satisfy the radiation selection rule for transition from the bottom of the conduction band. For 800-nm sub-bandgap excitation, the valence band electrons are excited to the defect levels at 1.55 eV above the valence band from where they transfer to defect levels centered at 1.1 and 1.55 eV with band widths of 0.3 and 0.1 eV, respectively above the valence band. There is no transition to these levels from the conduction band. For 400 nm band edge excitation, the valence band electrons are excited to the defect states located 100 meV below the conduction band, and these electrons decay to low lying defect states centered at 0.7, 0.95, 1.1, 1.35 and 1.55 eV within few picoseconds, which contributes to the fast decay process in the TA spectra of Fig. 4.7 (a). Since there is no PL associated with these transitions they are non-radiative and the speed of the transition suggests strong electron phonon coupling which must mean that these defects arise from the same entity (most likely oxygen vacancies). After the excitation these energy levels broaden into two conspicuous levels centered at 1.55 and 1.1 eV with very long life time as was seen in the case of the 800 nm linear excitation.
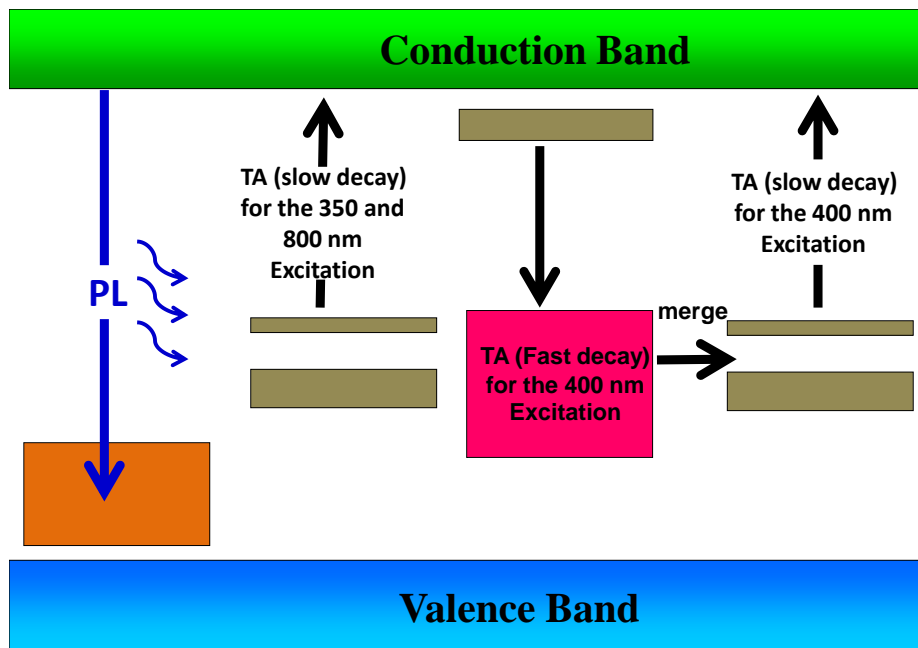
Figure 4.8. Illustration of origin of electron dynamics for 350-, 800-, and 400-nm excitations. The plotted defect levels are not exactly to scale.

4.4 Conclusions

The PL and transient absorption of STO under multi-photon and one-photon excitation at room temperature was studied. The PL originated from electron decay from the conduction band to a defect band centered at 0.4 eV (with a 0.7 eV bandwidth) above the valence band with a life time of 25 ns. There were defect levels centered at 0.7, 0.95, 1.1, 1.35 and 1.55 eV to which rapid non-radiative transitions occurred from the oxygen vacancy levels just below the conduction band. The fast non-radiative transitions (~ few ps) suggested that these defect levels may originate from the same atomic entity as the electron-phonon coupling is very strong. After the fast decay, these energy levels are coalesced into two prominent trap levels centered at 1.1 and 1.55 eV above the valence band.

Bibliography

1. A. Ohtomo and H. Hwang, "A high-mobility electron gas at the LaAlO3/SrTiO3 heterointerface," Nature 427, 423-426 (2004).

2. Ariando, X. Wang, G. Baskaran, Z. Q. Liu, J. Huijben, J. B. Yi, A. Annadi, A. R. Barman, A. Rusydi, S. Dhar, Y. P. Feng, J. Ding, H. Hilgenkamp and T. Venkatesan, "Electronic phase separation at the LaAlO3/SrTiO3 interface," Nat Commun 2, 188 (2011).

3. N. Reyren, S. Thiel, A. D. Caviglia, L. F. Kourkoutis, G. Hammerl, C. Richter, C. W. Schneider, T. Kopp, A.-S. Rüetschi, D. Jaccard, M. Gabay, D. A. Muller, J.-M. Triscone and J. Mannhart, "Superconducting Interfaces Between Insulating Oxides," Science 317, 1196-1199, (2007).

4. G. Herranz, M. Basletić, M. Bibes, C. Carrétéro, E. Tafra, E. Jacquet, K. Bouzehouane, C. Deranlot, A. Hamzić, J. M. Broto, A. Barthélémy and A. Fert, "High Mobility in LaAlO3/SrTiO3 Heterostructures: Origin, Dimensionality, and Perspectives," Physical Review Letters 98, 216803 (2007).

5. R. Pentcheva and W. E. Pickett, "Charge localization or itineracy at LaAlO3∕SrTiO3 interfaces: Hole polarons, oxygen vacancies, and mobile electrons," Physical Review B 74, 035112 (2006).

6. M. S. J. Marshall, A. E. Becerra-Toledo, L. D. Marks and M. R. Castell, "Surface and Defect Structure of Oxide Nanowires on SrTiO3," Physical Review Letters 107, 086102 (2011).

7. N. Nakagawa, H. Y. Hwang and D. A. Muller, "Why some interfaces cannot be sharp," Nat Mater 5, 204-209 (2006).

8. A. F. Santander-Syro, O. Copie, T. Kondo, F. Fortuna, S. Pailhes, R. Weht,

X. G. Qiu, F. Bertran, A. Nicolaou, A. Taleb-Ibrahimi, P. Le Fevre, G. Herranz, M. Bibes, N. Reyren, Y. Apertet, P. Lecoeur, A. Barthelemy and M. J. Rozenberg, "Two-dimensional electron gas with universal subbands at the surface of SrTiO3," Nature 469, 189-193, (2011).

9. Y. Yamada, H. Yasuda, T. Tayagaki and Y. Kanemitsu, "Temperature Dependence of Photoluminescence Spectra of Nondoped and Electron-Doped SrTiO3: Crossover from Auger Recombination to Single-Carrier Trapping," Physical Review Letters 102, 247401 (2009).

10 . H. Yasuda and Y. Kanemitsu, "Dynamics of nonlinear blue photoluminescence and Auger recombination in SrTiO3," Physical Review B 77, 193202 (2008).

11. Y. Kanemitsu and Y. Yamada, "Light emission from SrTiO3," physica status solidi (b) 248, 416-421, (2011).

12. Y. Yamada, H. Yasuda, T. Tayagaki and Y. Kanemitsu, "Photocarrier recombination dynamics in highly excited SrTiO3 studied by transient absorption and photoluminescence spectroscopy," Applied Physics Letters 95, 121112 (2009).

13. S. Mochizuki, F. Fujishiro and S. Minami, "Photoluminescence and reversible photo-induced spectral change of SrTiO3," Journal of Physics: Condensed Matter 17, 923 (2005).

14. D. Kan, T. Terashima, R. Kanda, A. Masuno, K. Tanaka, S. Chu, H. Kan, A. Ishizumi, Y. Kanemitsu, Y. Shimakawa and M. Takano, "Blue-light emission at room temperature from Ar+-irradiated SrTiO3," Nat Mater 4, 816-819 (2005).

15. R. Leonelli and J. L. Brebner, "Time-resolved spectroscopy of the visible

emission band in strontium titanate," Physical Review B 33, 8649-8656 (1986).

16. Y. Yamada and Y. Kanemitsu, "Band-to-band photoluminescence in SrTiO3," Physical Review B 82, 121103 (2010).

17. A. Rubano, D. Paparo, F. Miletto, U. Scotti di Uccio and L. Marrucci, "Recombination kinetics of a dense electron-hole plasma in strontium titanate," Physical Review B 76, 125115 (2007).

18. K. Yumashev, P. Prokoshin, A. Malyarevich and V. Mikhailov, "Transient bleaching/induced absorption in reduced SrTiO3 under picosecond excitation," JOSA B 14, 415-419 (1997).

19. X. Wang, J. Q. Chen, A. R. Barman, S. Dhar, Q.-H. Xu, T. Venkatesan and Ariando, "Static and ultrafast dynamics of defects of SrTiO3 in LaAlO3/SrTiO3 heterostructures," Applied Physics Letters 98, 081916 (2011).

20. C. Lee, J. Destry and J. L. Brebner, "Optical absorption and transport in semiconducting SrTiO3," Physical Review B 11, 2299-2310 (1975).

21. R. L. Wild, E. M. Rockar and J. C. Smith, "Thermochromism and Electrical Conductivity in Doped SrTiO3," Physical Review B 8, 3828-3835 (1973).

Chapter 5   Defect Electron Dynamics in TiO$_2$

5.1 Introduction

TiO$_2$ is an important oxide material, and it has been widely studied for applications to photocatalysts and solar cells owing to its high catalytic efficiency.[1-3] TiO$_2$ has a bandgap of 3.1 eV, which lies between the UV to visible light range.[4] Owing to its high photo-chemical activity, TiO$_2$ has attracted increasing interest in recent years.[5-8] These studies revealed that theoptical property is one of the dominant characteristics of TiO$_2$. Understanding the optical properties could help us to find a way to improve the photo-reaction efficiency of TiO$_2$. Femtosecond to picosecond carrier dynamics studies of TiO$_2$ are the main techniques used to study the reaction process.

This chapter describes the carrier dynamics of TiO$_2$ single crystals and films. We also studied the carrier dynamics of the oxygen vacancy in TiO$_2$ and TiO$_2$ films with Ta substitution in the Ti site. Photocatalysis applications of TiO$_2$ films were also studied. The photocatalysis efficiency was found to show a high correlation with the carrier relaxation lifetime of TiO$_2$ varied by changing the oxygen pressure during deposition.

5.2 Experimental Procedure

In this study, three different sets of samples were studied. 1. Doubly polished (100) rutile TiO$_2$ single crystals [Crystec GmbH] of 1×1 cm size and 0.5-mm thickness were used as received. 2. Two TiO$_2$ films were deposited at temperatures of 700 ℃ under an oxygen pressure of 1×10^{-3} and 5×10^{-6} Torr, respectively on quartz, with a repetition rate of 10 Hz for 90 min, and the film

thickness was estimated to be ~600 nm and the films were polycrystalline. The chamber base pressure for all depositions was maintained well below 1×10^{-6} Torr. $Ta_xTi_{1-x}O_2$ (x=0, 0.03, 0.06, 0.1) films on LAO substrates were deposited at 800 ℃ under an oxygen pressure of 1×10^{-5} Torr and laser repetition rate of 5 Hz for 90 min, and the film thickness was found to be 300 nm and in single anatase phase. The film deposition conditions are described in detail in chapter 2.

The UV-Vis transmission spectroscopy, TA, and pump-probe techniques were the same as those described in chapter 2.

5.3 Results and Discussion

5.3.1 Transient absorption of pure TiO_2 bulk single crystal and films

Figure 5.1 shows the UV-Vis transmission spectra of the as received TiO_2 single bulk crystal (black line) and the PLD-prepared pure TiO_2 film on quartz substrate (red and green lines). The oscillation peaks are due to film interference, which is often observed in a thin film.[9-11] The interference also indicates that the prepared film has a uniform surface quality. Furthermore, the UV-Vis transmission spectrum shows that the TiO_2 single crystal and film has a bandgap of 3.1 and 3.5 eV, respectively.
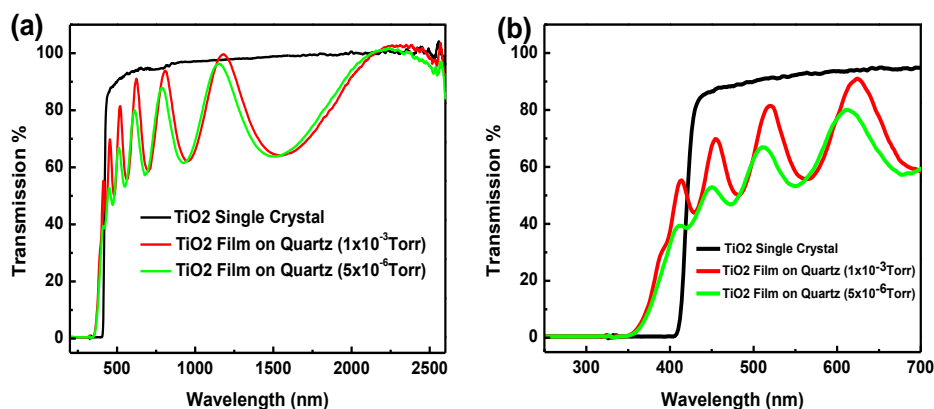
Figure 5.1. UV-Vis transmission spectra of TiO$_2$ single crystal and films.

Figure 5.2 shows the 400-nm excitation TA spectrum of the TiO$_2$ single crystal with delay times of 1, 200, and 500 ps. The TA transmission results show two broad absorption peaks located at 2.4 and 1.8 eV with bandwidths of 0.2 and 0.5 eV, respectively. The 1.8 eV peak may have a number of transitions (centered at 2.0, 1.8, 1.7, 1.65, and 1.6 eV), giving rise to a broad band. The TA spectrum shows that the photon excited carriers have a long decay time, as seen in Fig. 5.3. The single wavelength dynamic results show that the carrier relaxation time is around 1–2 ns for probe photon energy of 1.6-2.4 eV.

The long decay time (a consequence of the indirect band gap) may indicate that the recombination process for excited carriers is very slow. This long lifetime also explains the high photo-chemical activity of TiO$_2$, where the excited carrier has sufficient time to oxidize or reduce other materials.
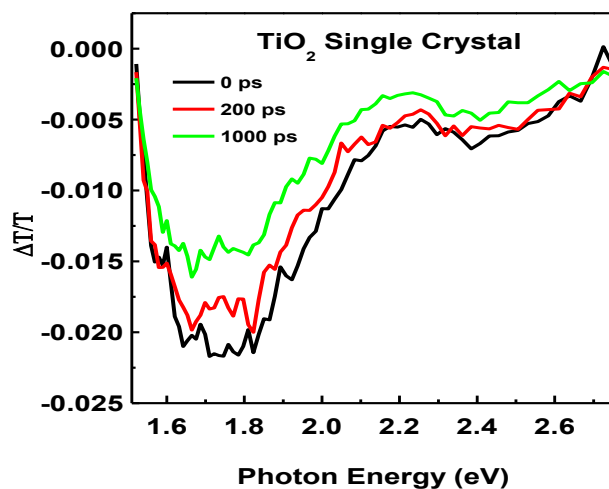
Figure 5.2. Transient absorption spectra of TiO$_2$ single crystal with different delay times under 400-nm (160 μJ/cm^2) excitation.
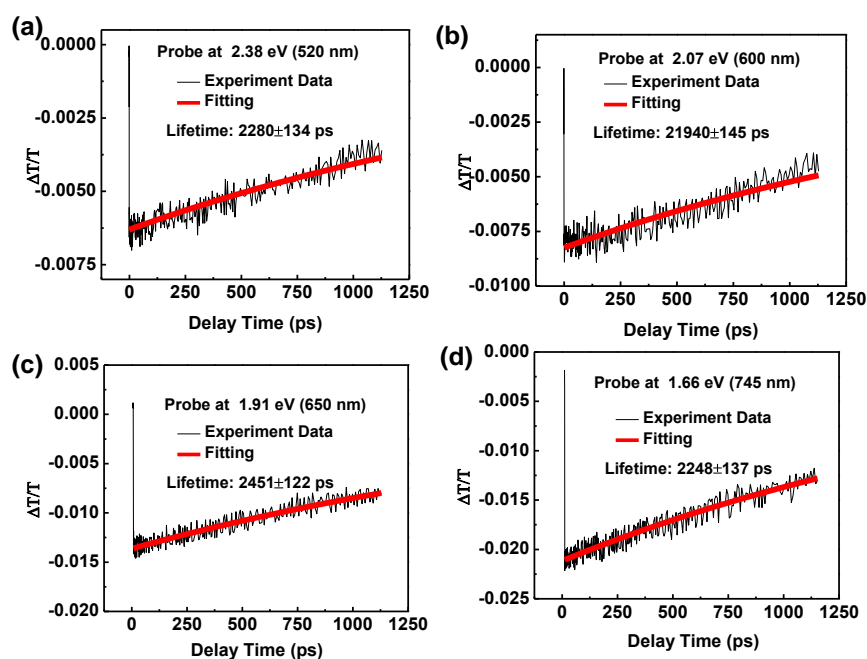
Figure 5. 3. Single wavelength dynamic of TiO$_2$ single crystal at probe photon energy of (a) 2.38, (b) 2.07, (c) 1.91 and (d) 1.66 eV under 400-nm (160μJ/cm^2) excitation.

83

As shown above, the TiO$_2$ single crystal has unique properties that make it suitable for photo-catalysis applications. It is preferable to use thin film TiO$_2$ instead of the bulk crystal to reduce the cost of TiO$_2$-based devices. However, the defect levels and carrier dynamics in the films may be quite different compared to the bulk crystal because the films usually have more defects due to oxygen vacancies, impurities, and lattice distortion. To understand the role of these defects as well to study the carrier recombination process in the films, we studied the TA of the TiO$_2$ films. It is well known that the common defect in TiO$_2$ is an oxygen vacancy. Therefore, we prepared two films with different oxygen vacancies to study their effects on the carrier dynamics.

Figure 5.4 shows the TA spectra of the TiO$_2$ films prepared under different oxygen pressures. As shown, both films have three induced absorption peaks centered at 2.3, 1.95 and 1.65 eV, respectively. Compared to the single crystal TiO$_2$ these peaks are similar but several of the transitions also seen in single crystal (at 1.8, 1.7 and 1.6 eV) are missing. The origin of this difference is not clear. All these peaks decreas rapidly with delay time. Figure 5.5 shows the decay dynamics in detail for probe photon energy of 2.3, 1.95 and 1.65 eV. Single exponential decay fitting shows that these defects have a lifetime of ~300 ps. Clearly this fast decay time is related to the large amount of oxygen vacancies present in the film. This is supported by the fact that TiO$_2$ films prepared at low oxygen pressures (with a larger number of oxygen vacancies) show even faster carrier decay time of 180 ps (Fig. 5.6).

A consistent picture that emerges is that single crystals show long carrier lifetimes while polycrystalline thin films show much shorter lifetimes. There are many factors in a polycrystalline film that could contribute to the short lifetime, such as grain boundaries, surface recombination, oxygen vacancy

and so on. Based on the data, oxygen vacancies play a role in reducing the carrier lifetimes. The role of grain boundaries requires comparison with single crystalline films. (As will be shown in the next section, single crystal TiO_2 films (anatase) show ns recombination times as expected). From a catalysis perspective, all of these effects are not good since they decrease the carrier lifetime.
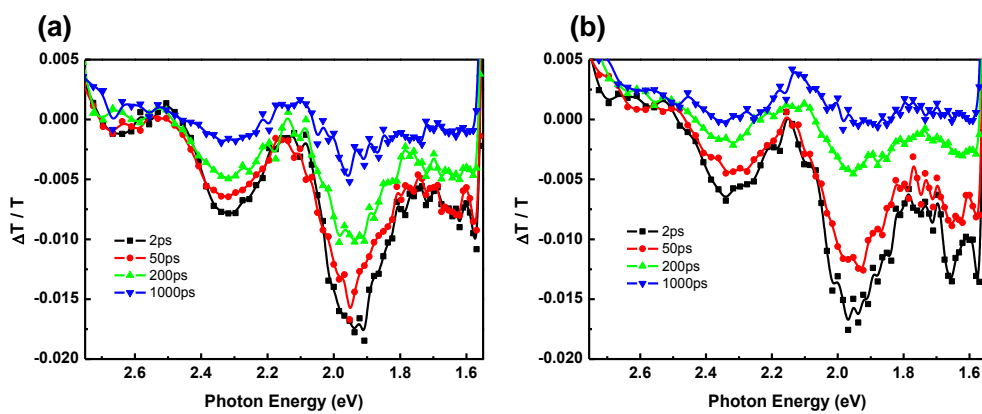
Figure 5.4. Transient absorption spectra of PLD-prepared TiO_2 films. (a) TA for low oxygen vacancy TiO_2 film (1×10^{-3} Torr). (b) TA for high oxygen vacancy TiO_2 film (5×10^{-6} Torr) under 400-nm (160 $\mu J/cm^2$) excitation.
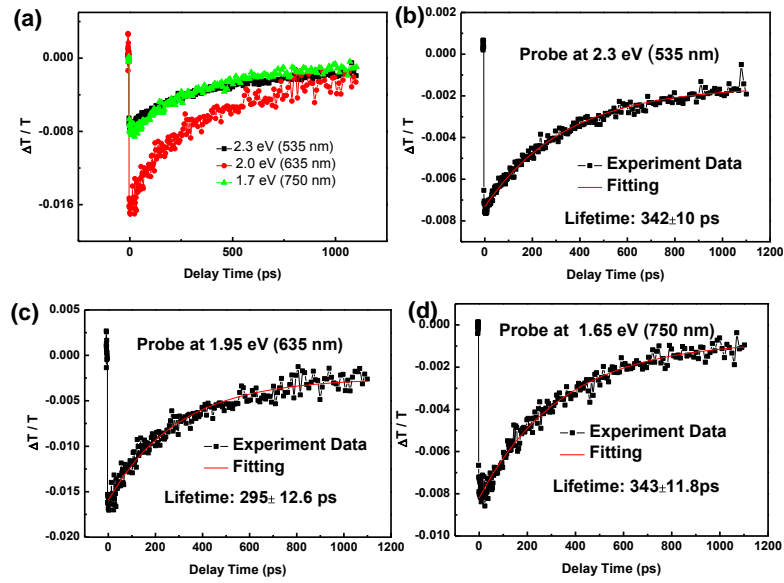
Figure 5.5. (a) Single wavelength decay dynamics for TiO$_2$ film with less oxygen vacancies (1 $\times 10^{-3}$ Torr) under probe photon energy of (b) 2.3, (c) 1.95 and (d) 1.65 eV using 400-nm (160 μJ/cm^2) excitation.
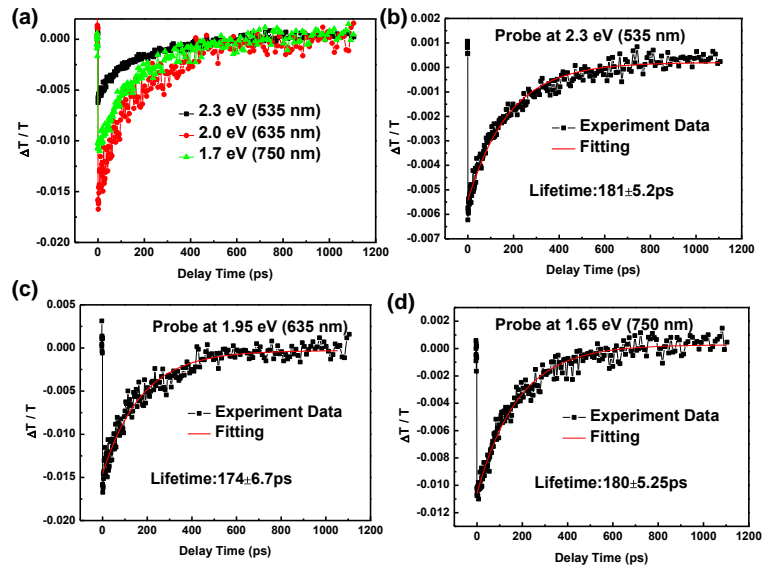
Figure 5.6. (a) Single wavelength decay dynamics for TiO$_2$ film with more oxygen vacancies (5 $\times 10^{-6}$ Torr) under probe photon energy of (b) 2.3, (c) 1.95 and (d) 1.65 eV using 400-nm (160 μJ/cm^2) excitation.

86

5.3.2 Transient absorption for Ta-doped anatase TiO_2 films

Chemical substitution is a commonly used method to change the optical properties of TiO_2.[12-15] As mentioned above, the oxygen vacancy can introduce free electrons into the system, which speeds up the carrier recombination process. Chemical substitution can also introduce free electrons and thus change the optical properties of TiO_2 films. As discussed before, a TiO_2 film deposited on quartz substrate has many defects due to lack of lattice match, resulting in the short lifetime of the excited carriers. To reduce the number of defects as well as to increase the film quality, we have prepared single-crystal TiO_2 films. With the perfect lattice match between TiO_2 and LAO, high-quality single-crystal anatase films have been obtained, as shown in Fig 5.7. Furthermore, we have also prepared Ta-substituted TiO_2 to study the effect of Ta substitution on the carrier recombination process.

The XRD spectrum shown in Fig. 5.7 indicates that Ta-substituted TiO_2 has an anatase phase. The LAO substrate has a lattice constant of 3.789 Å, which matches the lattice constant of anatase TiO_2 (3.782Å) very well. This can be seen from the strong anatase peak in the XRD spectrum. The good crystal film showed a reduced number of surface defects, and therefore, the changes in properties are mainly due to the effect of Ta substitution.

Figure 5.8 shows the UV-Vis transmission spectra of Ta substituted TiO_2 films. It can be seen that the band gap of TiO_2 increases with the Ta substitution concentration. With 10% Ta substitution, the band gap of TiO_2 is blue shifted by 0.25 eV. It can also be seen that as the Ta concentration increases, more free electrons dominate the system and an absorption peak appears in the infrared range.
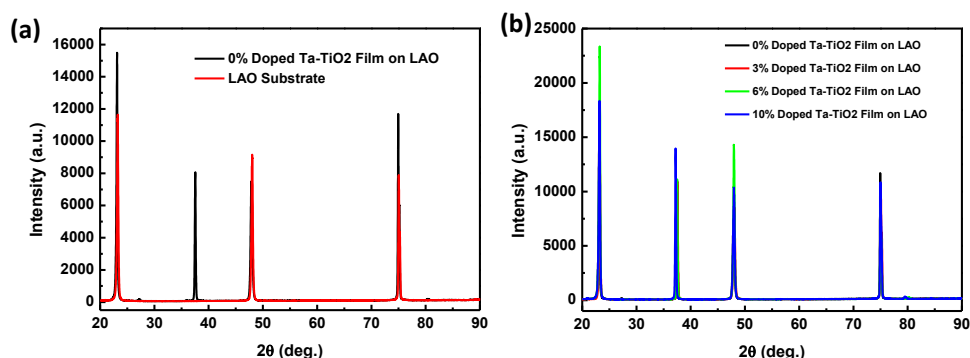
Figure 5.7. (a) XRD spectra of TiO$_2$ film and LAO substrate. (b) XRD spectra of Ta-substituted TiO$_2$ films.
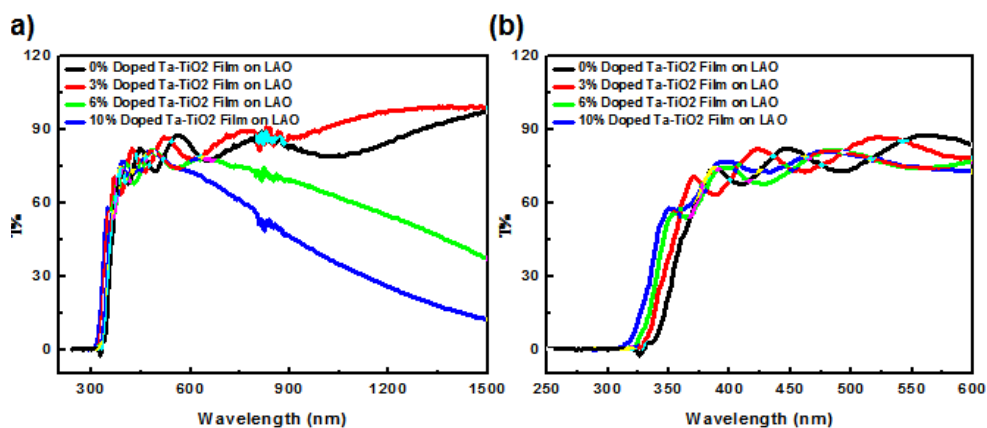
Figure 5.8. UV-Vis transmission spectra of Ta-substituted TiO$_2$ films.

As discussed in chapter 3, the LAO single crystal shows defect absorption under 400-nm excitation. Considering that the LAO substrate is 0.5-mm thick, when using 400-nm excitation, the signal will be dominated by the LAO substrate signal. To eliminate this effect, we chose a shorter wavelength of 350 nm and detected the reflection signal from the TiO$_2$ films. It is shown that all signals are from the TiO$_2$ films, and no detectable LAO signal was observed in this reflection TA study.

Figure 5.9 shows the reflection TA spectrum of the pure TiO_2 anatase film deposited on the LAO substrate. A broadened induced absorption peak centered at 2.0 eV is observed. White light continuum is generated by the supercontinuum of the 800-nm fs laser pulse. To eliminate the source light, we used a 780-nm short pass filter to cut off the 800-nm light; because this filter cuts off longer wavelengths, the induced absorption peak above 780 nm is not shown. The pump-probe reflection dynamics shows that the carrier relaxation time has three time constants: a fast decay during the first 10 ps, followed by a slow decay with a lifetime of 100 ps, and finally a very slow decay in the order of 1000 ps.

Initially, for above band gap excitation, the photon is absorbed by the valence band electrons and is excited to the conduction band, where carrier–carrier scattering occurs with a lifetime of a few hundreds femtoseconds. The excited hot carriers relax to the bottom of the conduction band and from there to the lower levels via carrier-phonon interaction with a lifetime of ~10 ps. The additional Auger recombination process takes a longer time in the order of 100 ps. The finally observed 1000 ps decay dynamics may be due to the trapped defect states, which usually have very long lifetime.

Figure 5.10 shows the TA spectrum for a 3% Ta-substituted TiO_2 film. A broad absorption peak centered at 2.1 eV was observed just like pure TiO_2. The pump-probe dynamics experiment reveals only two decay processes: one with a short lifetime of 4 ps and the other with a lifetime of 28 ps. In a 6% Ta-doped film (Fig. 5.11), the absorption at 2.1 eV becomes sharper and the lifetime decrease to 2.2 and 12.3 ps, respectively. With a further increase in the Ta doping concentration, the lifetime of the carrier reduces further. A 10% Ta-doped TiO_2 film (Fig. 5.12) shows a very fast decay with a lifetime of 4 ps.

It is observed that the carrier dynamic signal does not fully relax to zero after 1000 ps in all cases, indicating the presence of a slow decay process characteristic of traps.

The prominent defect states seen at 2.1 eV is most likely from oxygen vacancies. What the TA spectrum shows is that the oxygen vacancy concentration decrease with Ta concentration. This is also consistent with the fact that the maximum TA observed decreases with Ta concentration. With the band gap increase, the energy gap between the intermediate defect levels and the valence band increases, resulting in the blue-shift of the observed TA. It is well known that when donors are introduced (by Ta substitution) into a semiconductor, the formation energy for oxygen vacancies begins to increase as the semiconductor resists further increases in charge. Hence the oxygen vacancy concentration decreases with Ta concentration.

Figure 5.13 summarizes the TA spectra at a delay time of 2 ps for TiO_2 films with different Ta substitution concentrations. It is shown that the induced TA peak blue-shifts with increasing Ta concentration. As mentioned before, the band gap of TiO_2 increases with the Ta concentration. This blue shift of the observed induced absorption from the TA spectrum is consistent with the band gap increase of TiO_2.

As shown before, TiO_2 single crystal has the slowest decay in the order of a few nanoseconds, anatase TiO_2 crystalline films have a decay of 1 ns and polycrystalline TiO_2 films on quartz substrates have a fast decay of 180-300 ps.

When Ta is substituted into TiO_2, the lifetime decreases steadily with Ta concentration. This must be related to the carriers already present in the

conduction band. It is also known that Ta substitution for Ti leads to changes in the band structure and the reduction of the carrier lifetime may be related to this issue.[16] The large donor contribution lowers the formation energy to compensate defects, such as Ti vacancy or Ti^{3+}. Such defects near the conduction band may also contribute to this TA signal.[16,17] These defect states may act as recombination centers and rapidly reduce the lifetime of the carriers. Furthermore, Ta-substituted TiO_2 films are more conductive than TiO_2, and excited holes easily recombine with electrons, which further reduce the carrier lifetime. In all samples, it was seen that the carrier does not relax back to the initial states up to several ns, suggesting the existence of some trapping centers that trap excited electrons contributing to the long lifetimes.[15]
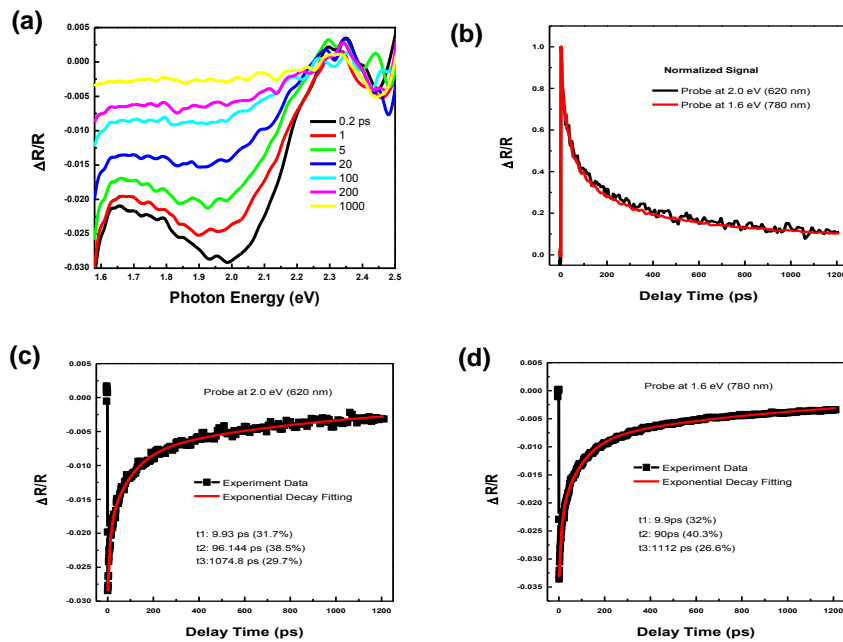
Figure 5.9. (a) Reflection transient absorption spectra for pure TiO_2 film on LAO substrate under 350-nm (100 $\mu J/cm^2$) excitation. (b) Single wavelength decay dynamics under probe photon energy of (c) 2.0 and (d) 1.65 eV.
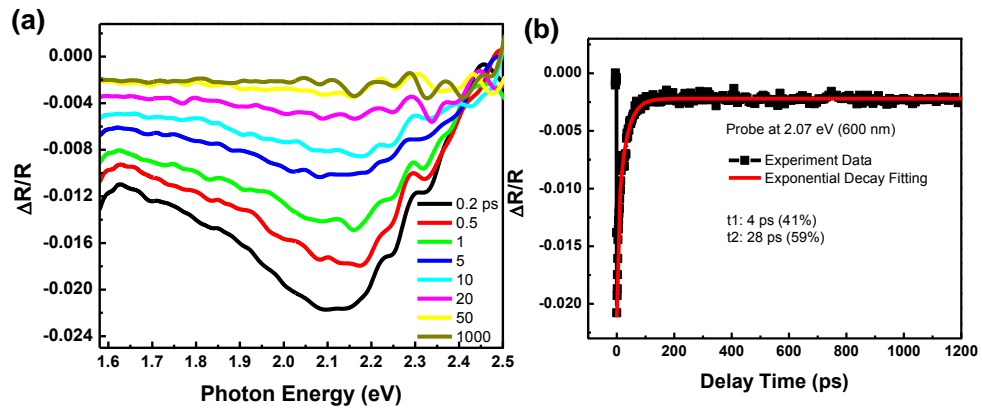
Figure 5.10. (a) Reflection transient absorption spectra for 3% Ta-substituted TiO$_2$ film on LAO substrate under 350-nm (100 μJ/cm^2) excitation. (b) Single wavelength decay dynamics under probe photon energy of 2.0 eV.
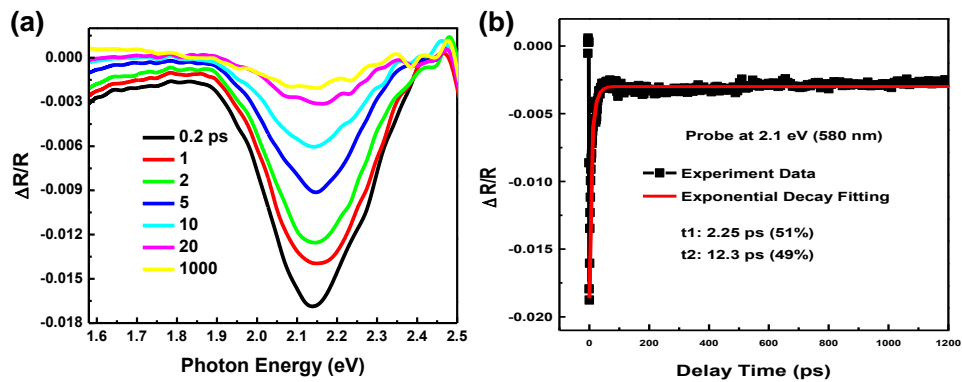
Figure 5.11. (a) Reflection transient absorption spectra for 6% Ta-substituted TiO$_2$ film on LAO substrate under 350-nm (100 μJ/cm^2) excitation. (b) Single wavelength decay dynamics under probe photon energy of 2.0 eV.
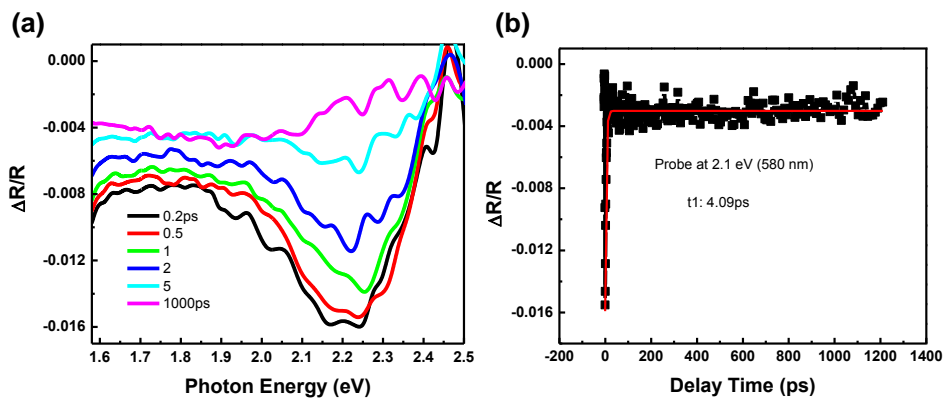
Figure 5.12. (a) Reflection transient absorption spectra for 10% Ta-substituted TiO$_2$ film on LAO substrate under 350-nm (100 μJ/cm^2) excitation. (b) Single wavelength decay dynamics under probe photon energy of 2.1 eV.
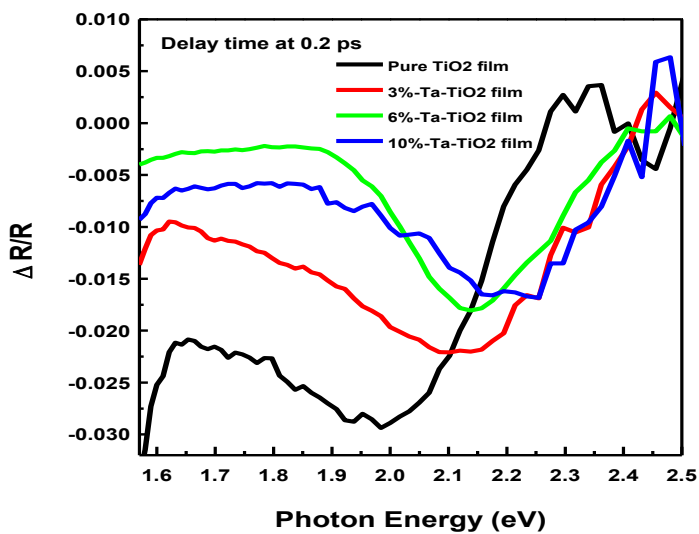
Figure 5.13. Reflection transient absorption spectra for TiO$_2$ film and Ta-substituted TiO$_2$ films at delay time of 0.2 ps under 350-nm (100 μJ/cm^2) excitation.

5.3.3 Photocatalysis application of TiO_2 film with different oxygen vacancies
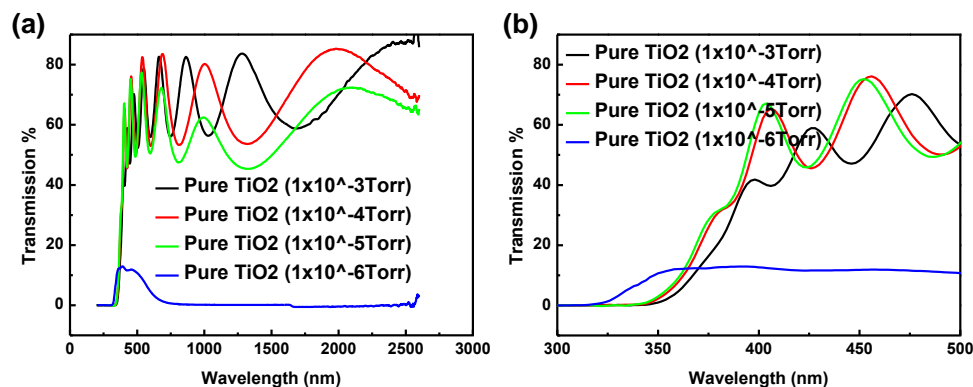
Figure 5.14. UV-Vis transmission spectra of TiO_2 films deposited under different oxygen pressures.

Figure 5.14 shows the UV-Vis absorption spectra of TiO_2 films deposited on quartz substrates with different oxygen vacancies. It is observed that the bandgap of TiO_2 increases from 3.54 to 3.85 eV as the oxygen pressure decreases from 1×10^{-3} to 1×10^{-6} Torr. TiO_2 deposited under low oxygen pressure shows strong absorption in the visible to NIR range; this absorption is due to the free electron absorption induced by the high oxygen vacancy.

To study the photocatalysis of TiO_2 films, we experimentally investigated the photodegradation of methylene blue using the TiO_2 films. The mechanistic scheme of the degradation of methylene blue using TiO_2 is shown below.

$$TiO_2 \xrightarrow{h\nu} h^+ + e^-$$
$$O_2 + e^- \longrightarrow O_2^-$$
$$h^+ + H_2O \longrightarrow OH^\cdot + H^+$$
$$h^+ + dye \longrightarrow products$$
$$OH^\cdot + dye \longrightarrow products$$
$$O_2^- + dye \longrightarrow products$$
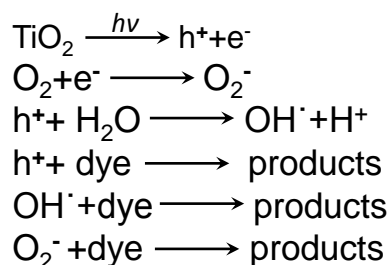
As mentioned above, the TiO_2 carrier relaxation time decreases with the oxygen vacancy. For catalysis, electrons or holes are usually required to have long lifetime so that the excited carrier has sufficient time for the reaction. It is predicted that TiO_2 with low oxygen vacancy has high catalytic efficiency. Furthermore, the UV-Vis transmission spectrum suggests that low-oxygen-vacancy TiO_2 has the smallest band gap. This helps the material absorb more visible light and thus further increases the efficiency.

Figure 5.15 shows the photodegradation of methylene blue using TiO_2 films under 365-nm lamp irradiation. It is shown that the photodegradation efficiency decreases with the oxygen vacancy, which is consistent with our TA prediction. As TiO_2 absorbs the incident photons, electron and hole pairs are generated, and the holes degrade the methylene blue. To increase the efficiency of the degradation process, the holes need to have a long lifetime. Therefore, this shows that low-oxygen-vacancy samples have high efficiency.

It is observed that 365-nm light is just at the conduction band edge, because different oxygen vacancy samples have different band gaps. The low-oxygen-vacancy sample has a narrow band gap that absorbs more light and generates more electron and hole pairs. As the concentration of excited carriers increases, the photodegradation efficiency increases. In contrast, the high-oxygen-vacancy sample has a large band gap that absorbs less light; therefore, the efficiencies are low for this sample. This absorption difference affects the catalysis results. To study the carrier lifetime effect, we need to use above band gap irradiation for all samples in the photodegradation experiment.

Figure 5.16 shows the photo-degradation of the same TiO_2 samples using a

254-nm lamp as the irradiation source. 254-nm photons have energy that far exceeds the band gap of all TiO_2 samples, and therefore, under this irradiation, all samples have equal absorption of incident light and generation of electron-hole pairs. Under this situation, the difference in degradation efficiency can only be attributed to the carrier relaxation time.

This result is consistent with the fact that the low-oxygen-vacancy sample has a higher degradation effect. The high oxygen vacancy results in high electron concentration; these high-density electrons reduce the lifetime of the photon excited holes, thus causing low efficiency. Furthermore, the band gap blue shift increases with the oxygen vacancy, indicating that the oxygen vacancy also introduces defects into the structure; these defects usually act as recombination centers, and further reduce the lifetime of the excited carriers. All these effects reduce the catalysis efficiency of TiO_2.
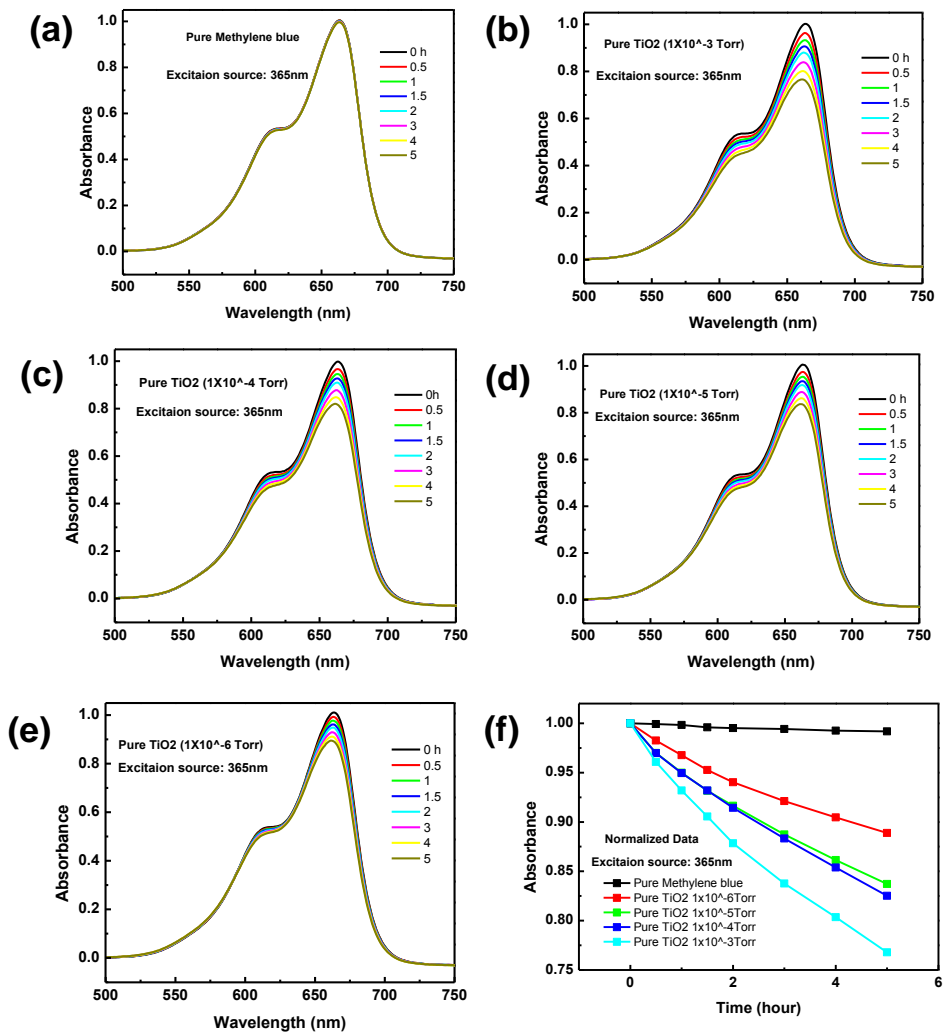
Figure 5.15. Photodegradation of Methylene blue using TiO$_2$ films under 365-nm UV lamp irradiation.
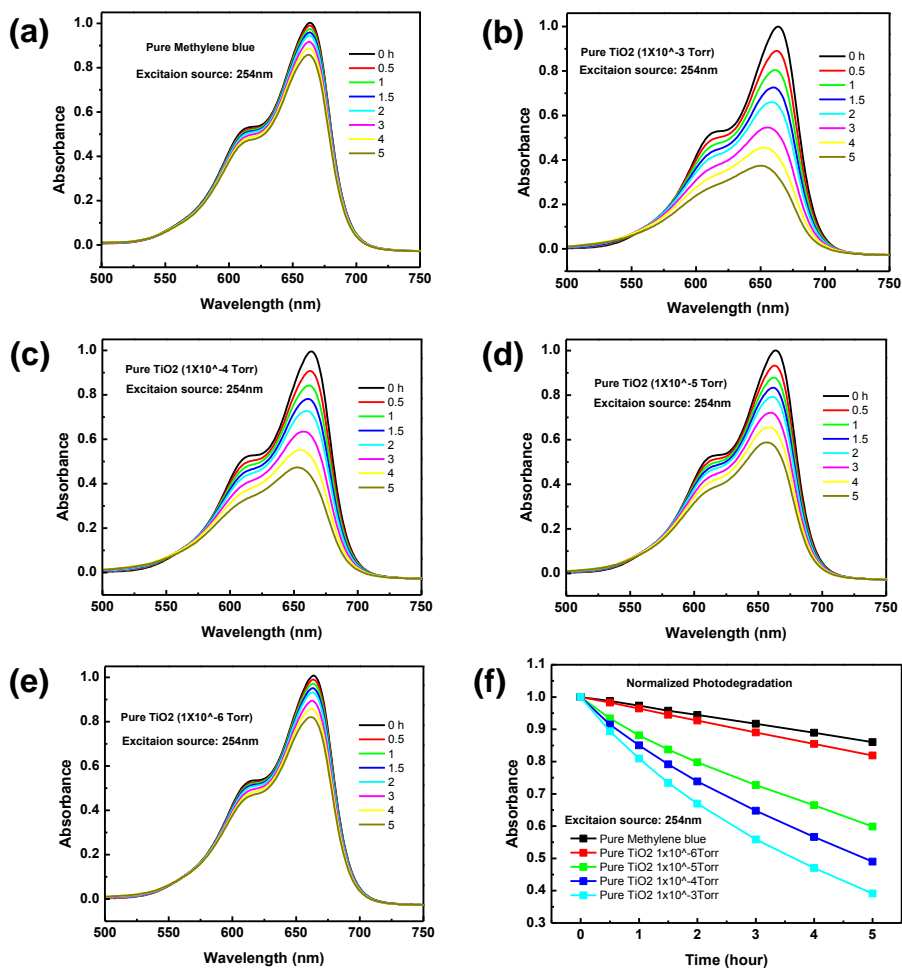
Figure 5.16. Photodegradation of Methylene blue using TiO_2 under 254-nm UV lamp irradiation.

Figure 5.17 summaries the photodegradation efficiency of TiO_2 films with different oxygen vacancies. The results show that the TiO_2 film deposited at a high oxygen pressure has a higher catalytic efficiency. As mentioned above, the excited carrier decay lifetime decrease with the oxygen vacancies. This may indicate that oxygen vacancies act as carrier recombination centers, with a resulting increase in electron and hole recombination rate and reduced catalytic efficiency.
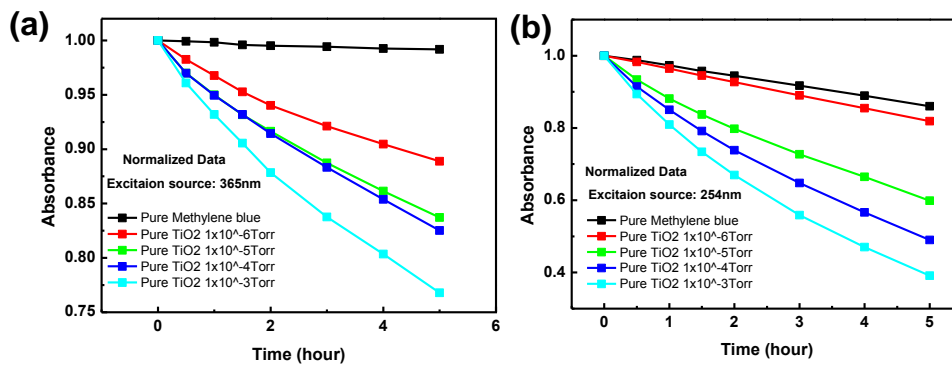
Figure 5.17. Photodegradation of Methylene blue using TiO_2 films with different oxygen vacancies under (a) 365 nm and (b) 254 nm UV lamp irradiation

5.4 Conclusions

In summary, the TA of TiO_2 in three different forms has been studied. The bulk single crystal shows two broadened TA centered at 2.4 and 1.8 eV. A pump-probe experiment showes that these peaks have a very long lifetime decay in the nanosecond range. These TA are due to the defect level in between the band gap. The three transient induced absorption peaks (2.3, 1.95, and 1.65 eV) of the polycrystalline TiO_2 films have a very fast decay time of 180-300 ps. The carrier lifetime decreases with the oxygen vacancy.

By using a 350-nm fs laser, we studied the reflection TA spectra of Ta-substituted TiO_2. The TA spectra arose from the induced excited electron absorption. It is observed that the excited carrier lifetime decreases with the Ta concentration. The TA spectrum shows the blue-shift of the induced absorption peak, which is consistent with the UV spectrum in which the band gap increases with the Ta substitution concentration. Assuming that Ta replaces Ti ions, it lead to the reconstruction of the band structure, and

formation of compensating defects and these defects may help in increasing the carrier recombination process.

The photo-degradation experiment shows that the low-oxygen-vacancy TiO_2 film has higher degradation efficiency. This can be explained by the UV-Vis transmission and TA results. On one hand, the low-oxygen-vacancy TiO_2 film has a narrower band gap that helps it to absorb more light. On the other hand, the low-oxygen-vacancy samples have carriers with long lifetime, and the excited carrier can thus have sufficient time for the chemical action. These results suggest that for the application of TiO_2 film as a catalyst, it is better to use low-oxygen-vacancy samples.

Bibliography

1. M. Mrowetz, W. Balcerski, A. Colussi and M. R. Hoffmann, "Oxidative power of nitrogen-doped TiO2 photocatalysts under visible illumination," The Journal of Physical Chemistry B 108, 17269-17273 (2004).

2. S. Klosek and D. Raftery, "Visible light driven V-doped TiO2 photocatalyst and its photooxidation of ethanol," The Journal of Physical Chemistry B 105, 2815-2819 (2001).

3. K. Hara, K. Sayama, Y. Ohga, A. Shinpo, S. Suga and H. Arakawa, "A coumarin-derivative dye sensitized nanocrystalline TiO2 solar cell having a high solar-energy conversion efficiency up to 5.6%," Chemical Communications, 569-570 (2001).

4. T. Umebayashi, T. Yamaki, H. Itoh and K. Asai, "Band gap narrowing of titanium dioxide by sulfur doping," Applied Physics Letters 81, 454-456 (2002).

5. S. U. Khan, M. Al-Shahry and W. B. Ingler, "Efficient photochemical water splitting by a chemically modified n-TiO2," Science 297, 2243-2245 (2002).

6. A. L. Linsebigler, G. Lu and J. T. Yates Jr, "Photocatalysis on TiO2 surfaces: principles, mechanisms, and selected results," Chemical Reviews 95, 735-758 (1995).

7. W. Choi, A. Termin and M. R. Hoffmann, "The role of metal ion dopants in quantum-sized TiO2: correlation between photoreactivity and charge carrier recombination dynamics," The Journal of Physical Chemistry 98, 13669-13679 (1994).

8. H. Irie, Y. Watanabe and K. Hashimoto, "Nitrogen-concentration

dependence on photocatalytic activity of TiO2-x N x powders," The Journal of Physical Chemistry B 107, 5483-5486 (2003).

9. Z. Wu, A. Türkler, R. Brooks, D. Hole, P. Townsend, S. Köster, K. Kurt, J. Gonzalo and A. Suarez-Garcia, "Luminescence characterisation of defects in pld alumina and copper implanted silica," Nuclear Instruments and Methods in Physics Research Section B: Beam Interactions with Materials and Atoms 191, 121-126 (2002).

10. H. Sakai, M. Watanabe, K. Takiyama and B. Ullrich, "Optical properties of ZnxCd1-xS mixed crystal thin film produced by PLD," International Congress on Laser Advanced Materials Processing. 270-273 (2002)

11. W. Hu, Z. Liu, J. Sun, S. Zhu, Q. Xu, D. Feng and Z. Ji, "Optical properties of pulsed laser deposited ZnO thin films," Journal of Physics and Chemistry of Solids 58, 853-857 (1997).

12. M. Salmi, N. Tkachenko, R. J. Lamminmaki, S. Karvinen, V. Vehmanen and H. Lemmetyinen, "Femtosecond to nanosecond spectroscopy of transition metal-doped TiO2 particles," J. Photochem. Photobiol. A-Chem. 175, 8-14, (2005).

13. K. Takeshita, A. Yamakata, T. Ishibashi, H. Onishi, K. Nishijima and T. Ohno, "Transient IR absorption study of charge carriers photogenerated in sulfur-doped TiO2," J. Photochem. Photobiol. A-Chem. 177, 269-275, (2006).

14. S. Tojo, T. Tachikawa, M. Fujitsuka and T. Majima, "Iodine-doped TiO2 photocatalysts: Correlation between band structure and mechanism," J. Phys. Chem. C 112, 14948-14954, (2008).

15 . K. Yamanaka and T. Morikawa, "Charge-Carrier Dynamics in

Nitrogen-Doped TiO2 Powder Studied by Femtosecond Time-Resolved Diffuse Reflectance Spectroscopy," J. Phys. Chem. C 116, 1286-1292, (2012).

16. A. R. Barman, M. Motapothula, A. Annadi, K. Gopinadhan, Y. Zhao, Z. Yong, I. Santoso, M. Breese, A. Rusydi and S. Dhar, "Multifunctional Ti1−xTaxO2: Ta doping or alloying?" Applied Physics Letters 98, 072111 (2011).

17. Y. Zhao, A. R. Barman, S. Dhar, A. Annadi, M. Motapothula, J. Wang, H. Su, M. Breese, T. Venkatesan and Q. Wang, "Scaling of flat band potential and dielectric constant as a function of Ta concentration in Ta-TiO2 epitaxial films," AIP Advances 1, 022151-022159 (2011).

Chapter 6   Optical Bistability in Graphene

6.1 Introduction

Graphene is a rising star in nonlinear optics due to its easily-achievable saturable absorption and giant Kerr nonlinearity, which are both essential properties for digital optics based on optical nonlinear devices. [1-4] Here, we demonstrate the operation of a graphene-based optical Fabry–Perot cavity resonator with bistability. Absorptive and dispersive effects in graphene are hard to justify due to the limited absorption path length of a monolayer. Rather, we discovered that laser induced thermal stress produces bubbles on the graphene and bubbles create a vertical dimension adequate for strong non-linear dispersive effects, leading to an optically induced optical path length change of $\lambda/2$ at resonance. The all-optical switching between two optical states happens within a time scale of tens of nanoseconds due to the dispersive optical nonlinearities. Graphene-based optical devices with intrinsic optical bistability allow us to explore the promise of such elements as the building block of future high-speed all-optical circuitry.

Graphene photonics has given birth to a new research area which may be the cradle for many novel optoelectronic devices in the future. [5-8] The wavelength-independent absorption as well as switchable optical transition by shifting Fermi level has enabled many controllable photonic devices such as photodetector, electro-optical modulator, and polarization controller.[9-11] Due to the linear band structure which allows interband optical transitions at all photon energies, extremely large third-order optical nonlinearity $\chi^{(3)}$ has been observed in graphene.[3,4] As a result, graphene photonics extends to

multifunctional nonlinear devices including mode-locked laser and optical limiter.[1,2,12,13] Recently, graphene transferred onto silicon photonic crystal cavity was demonstrated to be an effective nonlinear optical device enabling resonant optical switching, regenerative oscillation and four-wave mixing.[14] However, in order to achieve high quality optical signal processing, it is nontrivial to isolate the optical nonlinearities of graphene from those of the supporting substrate materials such as silicon and other thermal nonlinearity effects.

The intrinsic type of bistable optical devices is a versatile platform to investigate these nonlinearities.[15] Great efforts have been dedicated to develop optical bistable devices with reduced size, low operating power, short switching times and room temperature operation.[16] A simple bistable optical device of the intrinsic type can be constructed by placing nonlinear optical materials inside a Fabry–Perot cavity.[17] These materials can either be dispersive, non-absorptive Kerr media, or absorptive type saturable absorbers. Practically, absorptive bistability is difficult to observe experimentally due to the small absorption length in a single layer of graphene, relatively small Fresnel number in a plane-mirror cavity and also the requirement for the photons to be somewhat close to a resonance.[17] Dispersive bistability can be achieved by the Kerr nonlinearity which can induce large phase shift and change the optical length by $\lambda/2$ or more at modest laser power. In order to achieve a large optical nonlinearity, very thick nonlinear media such as sodium vapour and InSb thin crystal are generally required.[18,19] The optical bistability in these devices is mainly driven by the refractive index change caused by the input light intensity. The change of the refractive index causes a change in the optical path length and when this is of the order of $\lambda/2$ this move

105

the device towards resonance. The resonance condition can be described by the Fabry-Perot formula:

$$nL = M \frac{\lambda}{2} \tag{6.1}$$

where n is refractive index, L is the length of the Fabry-Perot cavity, λ is the operating wavelength and M is an integer.

To date, the thinnest materials showing the optical bistability are micrometer-thick GaAs superlattices.[20,21] The phase shift β of this GaAs bistable etalon can be estimated by the following standard formula:

$$\beta = \frac{\Delta\omega}{\delta\omega} \alpha_0 d \left(1 + \frac{\Delta\omega^2}{\delta\omega^2}\right)^{-1} \tag{6.2}$$

where $\Delta\omega$ is the laser-resonance free-frequency separation, $\delta\omega$ is the resonance half-width at half-maximum, α_0 is the absorption coefficient and d is the thickness of absorptive medium. As the change of optical phase (also optical length) is proportional to the thickness of nonlinear media, an intriguing issue is whether this effect is observable in atomically thin, two-dimensional atomic crystals such as graphene. Although extremely large nonlinear Kerr coefficient has been reported in graphene, in order to generate a phase shift approaching π, the interaction with the light field will have to be significantly enhanced beyond that allowed by an atomically thin sheet.[3,4]

In this chapter, we demonstrate the intrinsic optical bistability of thermally restructured graphene nanobubble in a Fabry–Perot cavity. Although graphene is known to be a good saturable absorber, saturable absorptive effect alone cannot induce significant light modulation effect in the Fabry–Perot cavity

due to the limited absorptive path in atomically thin graphene. According to the analytic model by Szoke *et al.*[22], the condition for purely absorptive bistability in Fabry–Perot cavity is $\alpha d / (T + \alpha_B d) > 8$, where α is the absorption coefficient, α_B is unsaturable background absorption coefficient, d is the thickness of absorptive medium, and T is transmittance. Considering the monolayer graphene has a thickness of 0.335 nm and an absorption coefficient of 301,655 cm^{-1}, we arrive at $\alpha d = 0.01$, which is too small to fulfill the requirement for purely absorptive bistability.[23] Here we consider the possibility of engineering vertical corrugations in the form of bubbles on graphene in order to enhance the phase shift and obtain the optical bistability.

6.2 Experimental Procedure

The detailed configuration of the experimental setup is schematically shown in Chapter 2. Figure 6.1A shows our experimental setup for the observation of optical bistability in graphene. A high power (up to 5 W) laser at 532 nm with single longitudinal mode is used as the excitation source to achieve mode-matching resonance. The Fabry-Perot interferometer with two plane mirrors is mounted on Super-Invar frame to avoid thermal expansion. The cavity was aligned to see clear and sharp interference fringes (See Fig. 6.1B). The measured finesse of this system is about 17. However, in order to get a large laser intensity, a lens with a focal length of 2 cm was used, which cause transmission loss due to beam walk off. The maximum transmission of the empty cavity was only of 5%. This problem could be overcome by using a plano concave cavity properly mode matched to the incoming focused beam in order to get much larger transmission. However, in order to demonstrate bistability, this geometry of the resonator was adequate. Optical bistable

hysteresis is observed from monolayer graphene nanobubbles, as shown in Fig. 6.1C. In contrast, the empty cavity shows a linear response of transmitted power versus input power over the whole intensity range. A holding power (between switch-on and switch-off powers) of about 200 mW produces the widest optical hysteresis loop for the monolayer graphene over a focused beam diameter of ~1 μm. This power is comparable to that of a 5 μm thick GaAs superlattice over a focused beam diameter of 10 μm.[20] We can see that the transmitted power increases gradually at low input power and then increases suddenly when the incident power is above 250 mW. This is because the cavity resonance is not well tuned at low intensities but shifts towards the laser frequency as the input intensity is increased. Upon lowering the input, a switch-down intensity is reached, which shifts the cavity resonance away from the laser frequency. Therefore, a hysteresis between output and input is attained.
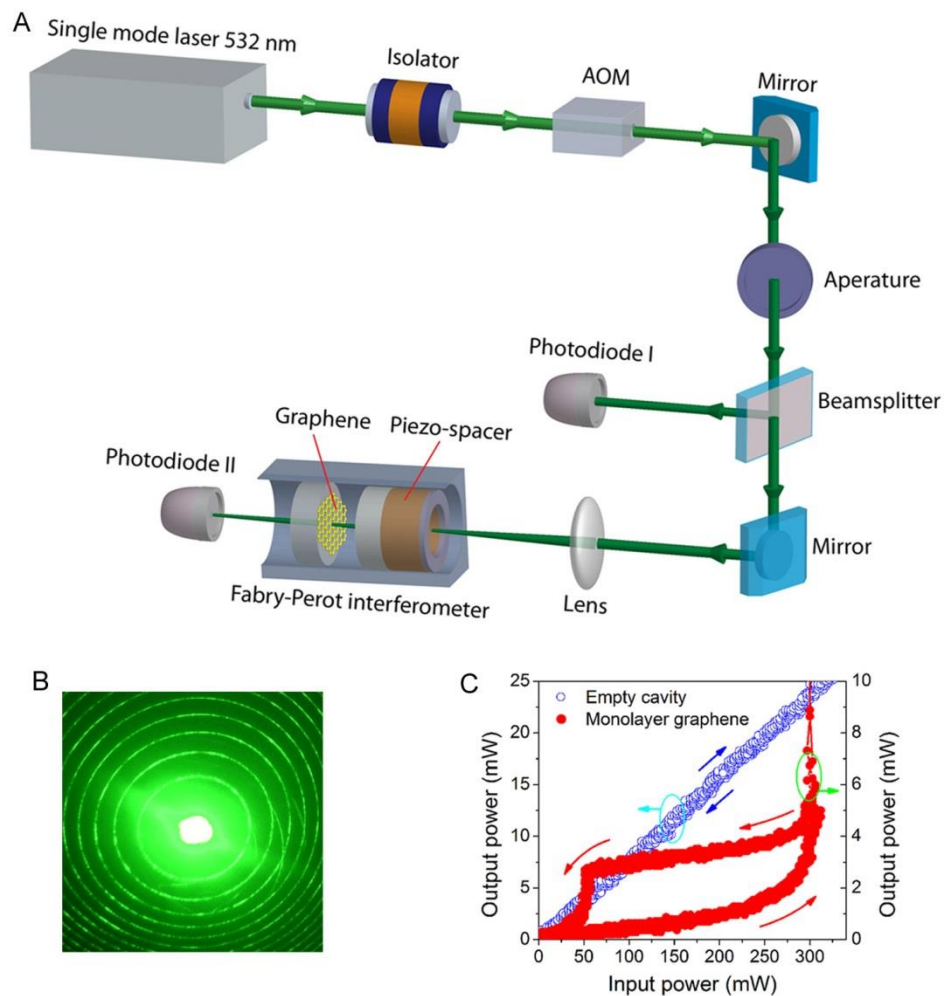
Figure 6.1. Optical bistability of graphene nanobubble. (A) Experimental setup for the observation of optical bistability in graphene. (B) Photograph showing interference fringes from the Fabry-Perot interferometer at resonance. (C) Optical bistability in monolayer graphene nanobubble. The blue trace is measured from empty Fabry-Perot cavity and the red trace is obtained by coating the back mirror with monolayer graphene.

6.3 Results and Discussion

6.3.1 Graphene preparation

Large area monolayer graphene films used in the work were grown by chemical vapour deposition (CVD) on Cu foil (Alfa Aesar AA13382RG). Poly(methyl methacrylate) (PMMA) thin film with thickness of ~ 100 nm was

spin-coated onto the as-grown graphene film, followed by the etching of the Cu catalyst in $FeCl_3$ solution. PMMA-supported graphene films were then rinsed in deionized water thoroughly and transferred onto the surface of partial reflecting mirrors. Last, the samples were submerged into acetone for the removal of PMMA. As the mirror coating is mainly a metal-oxide, the post-treatment of graphene sample in acetone will not cause any damage to the optical properties of the mirror. As-prepared samples were dried carefully by a gentle stream of N_2 gas prior to optical measurements.

The Raman spectra and images were measured on WITEC Alpha 300 confocal micro-Raman system equipped with a 532 nm laser source and 100✕ objective lens. The representative Raman spectra from bare mirror substrate and graphene transferred onto mirror are shown in Fig. 6.2A. For monolayer graphene, the Raman 2D band is much stronger than G band with a 2D/G ratio of 5.0, indicating the nature of one atomic layer.[24] The G and 2D band can be fitted well by single Lorentzian peak with full-width at half-maximum (FWHM) of 22 and 38 cm^{-1} respectively (shown in Fig. 6.2B and 6.2C), which suggested that the graphene used was of high crystalline quality.[25] These are key Raman features for monolayer graphene.

In order to verify the operating mechanism of the optical bistability, it is non-trivial to find out the saturation intensity in graphene samples which we have used. We transferred the same batch of monolayer and bilayer (stack of two monolayers) as well as multilayer graphene onto quartz substrate for the measurements. The nonlinear transmittance results are shown in Fig. 6.2D and E. For monolayer and bilayer graphene, the initial transmittance at low input power starts from ~97% and ~95% respectively. While increasing the input power of our 532 nm laser, the transmittance increases and then reaches

saturation, which is a typical behavior of saturable absorption. This saturable absorption phenomenon is even obvious in multilayer graphene which has a linear transmittance of about 78% (corresponding to ~10 layers of graphene). Saturation intensity is defined as the optical intensity required in a steady state to reduce the absorption to half of its unbleached value. The saturation intensity is estimated to be ~0.13 MW/cm^2 (1.3×10^9 W/m^2) for monolayer graphene, ~0.18 MW/cm^2 (1.8×10^9 W/m^2) for bilayer graphene and ~0.27 MW/cm^2 (2.7×10^9 W/m^2) for multilayer graphene (~10 layers).
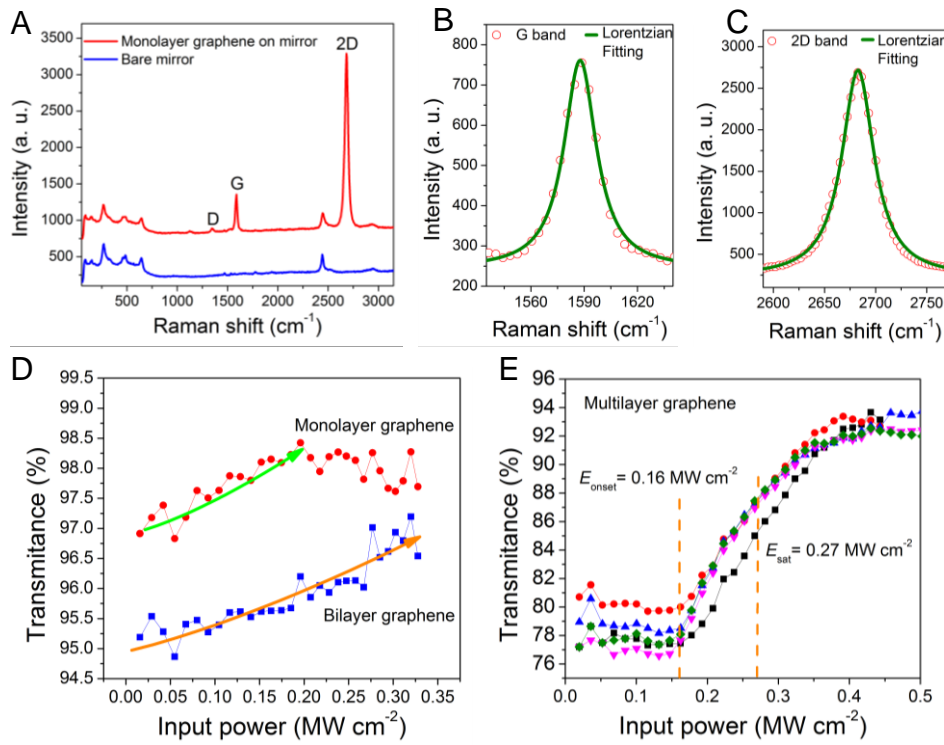
Figure 6. 2. (A) Raman spectra of bare mirror substrate and monolayer graphene on mirror. (B) Lorentzian fitting of G band giving FWHM of 22 cm^{-1}. (C) Lorentzian fitting of 2D band giving FWHM of 38 cm^{-1}. (D) Saturable absorption of monolayer and bilayer graphene. (E) Saturable absorption of multilayer graphene (~10 layers). The traces represent the measurements at different positions where the thickness is a little bit different.

111

6.3.2 Characterizations of graphene bubbles

Based on our current techniques, it is impossible to do in-situ observation on the graphene bubbles growth under intense laser irradiation while the graphene-covered mirror is working in the Fabry-Perot cavity. It is also quite challenging to locate the grapehene bubbles on the mirror after it is removed from the Fabry-Perot cavity as the laser spot and bubbles are too small to be identified by naked eyes and will not leave any clues on the mirror surface which is observable under optical microscope. Our strategy was to duplicate the laser irradiation conditions under a micro-Raman system which is equipped with objective lens to locate the laser spot. As the Raman system is equipped with a high resolution piezoelectric stage, we were able to scan the laser in the marked area on graphene. The Raman spectrometer with time-scan and image-scan functions is able to monitor spectrum changes during the bubble growth. AFM is used to identify the topography of graphene bubbles in the same area which was marked and irradiated by laser.

The Raman system (WITEC Alpha 300) is equipped with a 532 nm laser with maximum output power of 50 mW. The maximum laser power reaching the mirror surface is about 30 mW, which gives a power density of $\sim 3.8 \times 10^{10}$ W/m^2 if we considered the focused beam waist to be ~ 1 μm (which is actually even smaller, a few hundreds nanometres, if the laser is perfectly focused on mirror surface). This power density is much higher than the saturation intensity of 1.3×10^{9} W/m^2 in graphene, but still lower than the switching-on power in the cavity (i.e., 2.7×10^{11} W/m^2).

In order to study the accumulated heating effect induced by focused laser beam, we carried out time-dependent Raman spectroscopy while setting laser

power on sample surface at a modest value of 8 mW (not too high to prevent signal overload or any damage to our CCD detector). This will give a power density of ~ 1×10^{10} W/m^2. Raman spectra were recorded every second (integration time: one second) for 26 seconds immediately after the laser was shift to a fresh location on graphene surface. The results are shown in Fig. 6.3. We found that the Raman spectrum of graphene does not change too much in the first 10 seconds, but the D band continuously increases with a strong rise of the background in the following 10 seconds. The Raman spectrum nearly remains unchanged after 20 seconds illumination. We are not very clear about the origin of the strong background. If we compare the Raman spectrum collected at 20 seconds with that collected at 1 second, we can see that the D band at 1331.2 cm^{-1} is greatly enhanced, 2D band at 2668.8 cm^{-1} is weakened (Fig. 6.3B) and G band is relatively enhanced and broadened with a peak shift of 8.1 cm^{-1} from 1592.7 to 1600.8 cm^{-1} (Fig. 6.3C). These changes in Raman spectrum agree very well with the experimental observations on graphene bubbles reported in literature, which originates from the biaxial strain.[26]
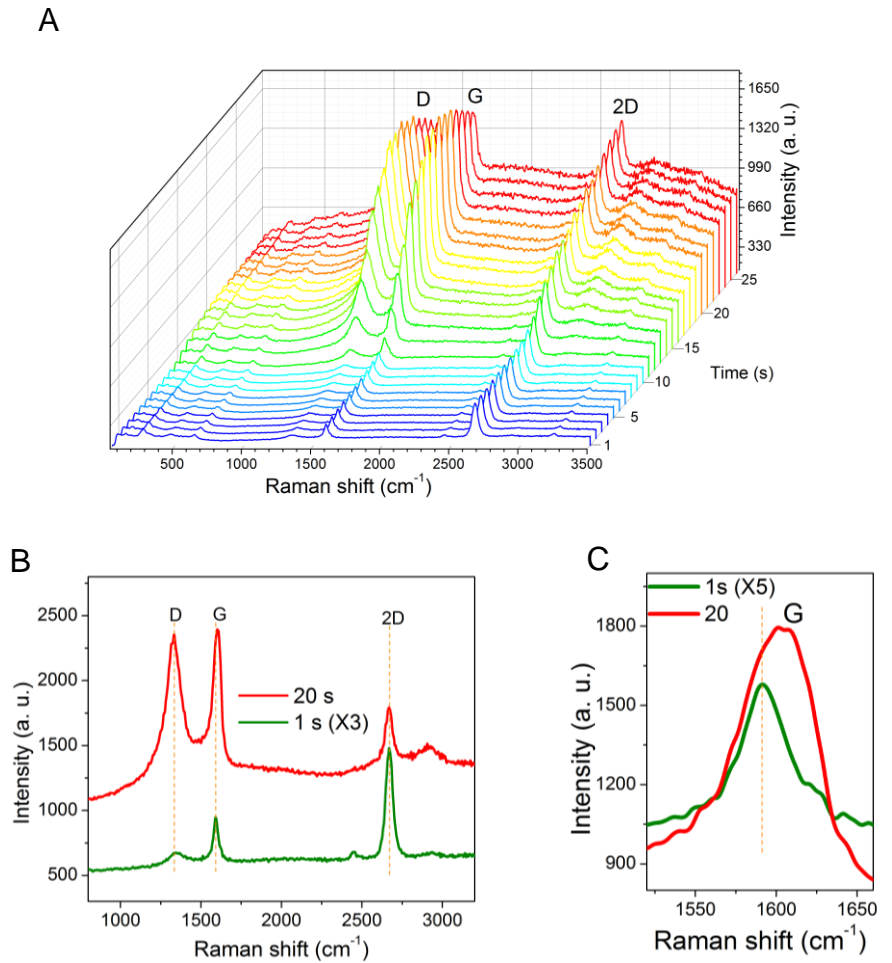
Figure 6. 3. Raman characterizations of graphene nanobubbles. (A) Time-dependent Raman spectra from graphene on mirror under laser irradiation. Integration time: one second. (B) Comparison of Raman spectra obtained at the 20th second and the first second. (C) Comparison of Raman G band obtained at the first second and the 20th second.

In order to verify our hypothesis on laser induced bubble formation, we carried out controlled Raman mapping and AFM measurements at the same location of the graphene sample, as shown in Fig. 6.4. We find a specific sample area which consists of the interface between monolayer graphene and bilayer graphene as well as a folded graphene ribbon. This feature can be easily identified in optical microscopies equipped in Raman as well as AFM system. A modest laser power (8 mW on sample surface, corresponding to

114

~1×10^{10} W/m^2) is applied to scan this area (80 points per line and a total of 80 lines) and Raman spectra were recorded simultaneously at each location. Figure 6.4B-D, show the Raman images of D band, G band and 2D. As we expected, there are lots of bright spots in the Raman image of D band (indicated by arrows in Fig. 6.4B), corresponding to the enhancement of D band signal.
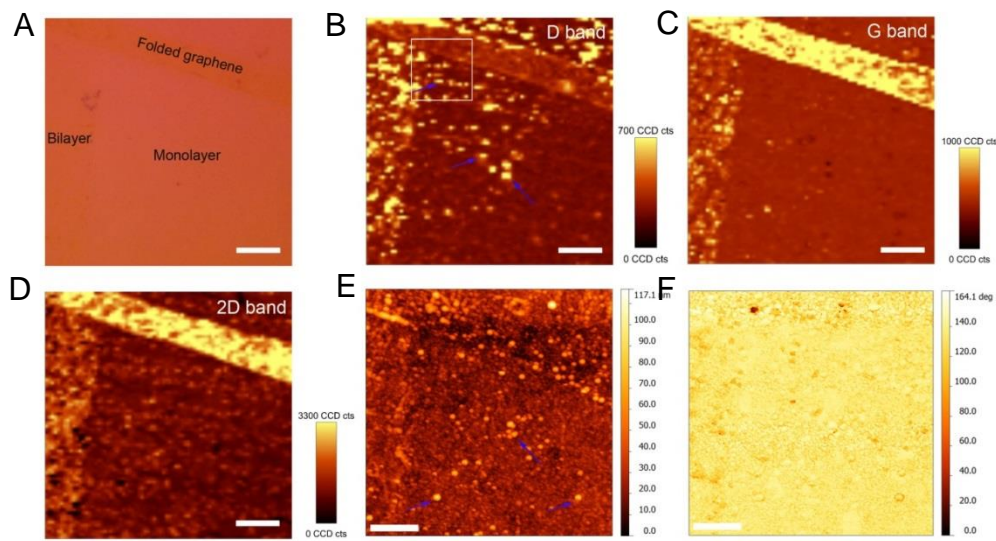
Figure 6. 4. Raman and AFM characterizations on selected area of graphene film. (A) Optical image of graphene showing the interface of monolayer and bilayer graphene as well as folded graphene. (B-D) Raman images of D band, G band and 2D band respectively. Scale bars: 7 μm. (E-F) AFM topographic and phase images of the graphene film after laser irradiation. The scanning area corresponds to the region indicated by the white square in Raman image of D band (Fig. 6.4 B). The blue arrows in E indicate the round shape blisters. Scale bars: 2 μm.

Following AFM measurements were carried out at the upper-left corner of monolayer graphene region where we can observe strong D band signals, as shown in Fig. 6.4, E and F. AFM characterizations reveal that graphene bubbles can indeed be formed as thermal stress causes the graphene to erupt into bubbles across the illuminated regions. These graphene nanobubbles are

found to be stable after removing the laser spot. We can see a few round shape blisters with the height larger than 50 nm, as indicated by the arrows in Fig. 6.4E. We can conclude that those graphene bubbles give strong D band signal due to the biaxial strain, and this is the direct evidence of graphene bubble formation after strong laser irradiation.
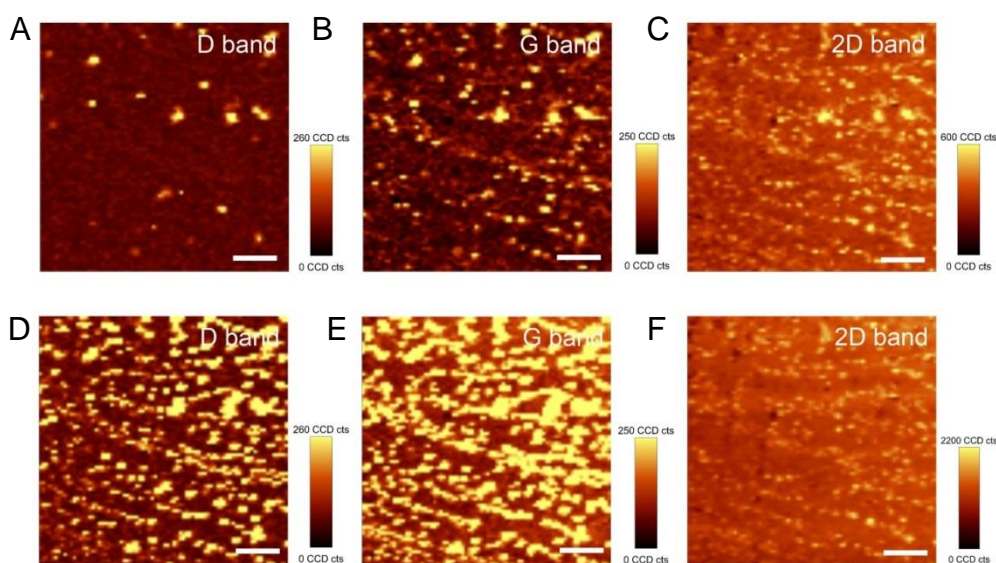
Figure 6. 5. Raman images of graphene on mirror before and after laser irradiation. (A-C) Raman images of D band, G band and 2D band before strong laser irradiation. (D-F) Raman images of D band, G band and 2D band after strong laser irradiation. Scale bars: 7 μm.

We are able to generate more spots which have similar changes in Raman signal (i.e., enhancement in D and G bands and blue-shift of G band) and locate them by Raman mapping with strong focused laser, as shown in Fig. 6.5. Here an area of 40×40 μm on monolayer graphene was investigated. We first performed Raman image scan in this area point-by-point (80 points per line and a total of 80 lines) with very low laser power (< 2 mW) which was below the threshold to cause any change in Raman spectra. The Raman

mapping results are shown in Fig. 6.5A-C, from which we only see a few bright spots with strong D band signals. These spots may originate from the strain of graphene film on the very rough mirror surface. Another possibility is that graphene film may be broken during the processes of transfer and removal of PMMA, which lead to defects. Subsequently, the highest laser power (30 mW on sample surface) was used to scan in the same area and the laser irradiation time at each spot was 0.3 second. At the same time, we collected the Raman spectra from each location and integrated different Raman bands to obtain the Raman images, as shown in Fig. 6.5D-F. Obviously, we can find many bright spots which correspond to Raman signal enhancements at those specific locations in Raman images of D band and G band after strong laser irradiation. From this data, we estimate that the coverage of graphene bubbles is about 30-40% of the surface area.

In order to further investigate graphene bubble growth after strong laser irradiation ($\sim 3.8 \times 10^{10}$ W/m^2), we carried out more AFM measurements on graphene which has been irradiated under the strong laser beam. We were able to find the same location treated by the laser with the help of markers under the microscope of the AFM system.
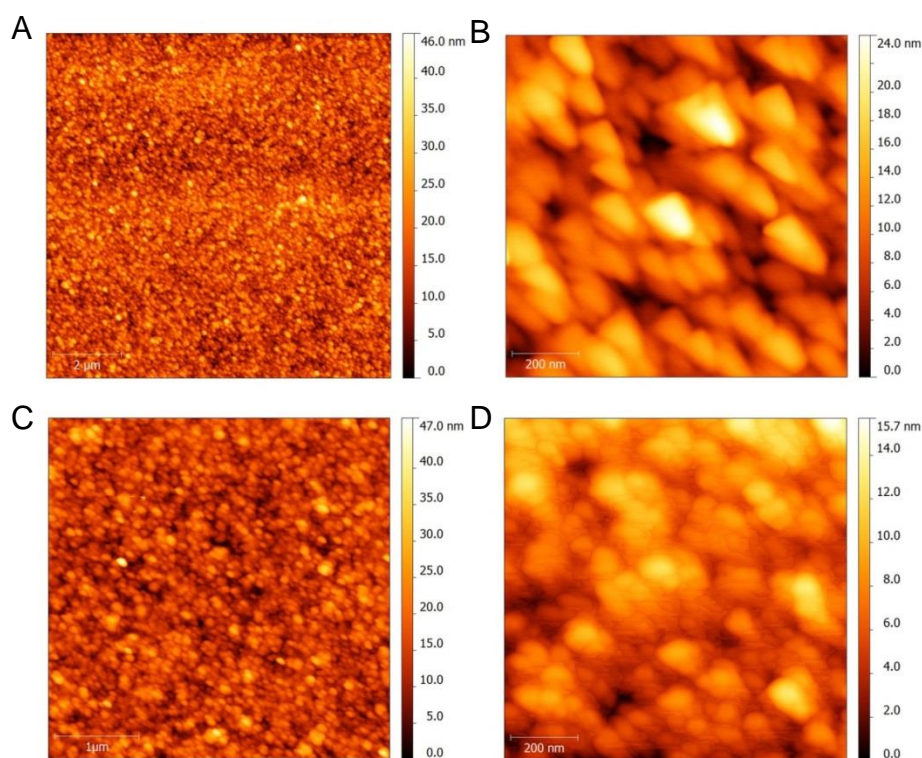
Figure 6. 6. AFM characterizations of bare mirror and graphene-covered mirror. (A-B) Topographic AFM images of bare mirror surface in an area of 10 μm and 1 μm respectively. (C-D) Topographic AFM images of graphene-covered mirror surface prior to laser irradiation in an area of 4 μm and 1 μm respectively.

Prior to laser irradiation, we did AFM measurements on bare mirror substrate and graphene-covered mirror, as shown in Fig. 6.6. It was found that the mirror coating consists of lots of metal oxide particles with the size less than 200 nm. As the mirror is polished to a λ/10 surface, the roughness (height difference between maximum and minimum) of the mirror is 46 nm over an area of 10 μm (shown in Fig. 6.6A). After covering with monolayer graphene film, the surface becomes smoother as graphene fills the gap between those particles. For example, with the same scan area of 1 μm in Fig. 6.6, B and D, the surface roughness has been reduced from 24 nm to 15.7 nm after covering with graphene. We are also able to see fluidic phase at the gaps of particles in

Fig. 6.6D and it is most like to be water and air trapped underneath graphene because the wet-transfer of graphene film onto rough mirror surface will withhold a certain amount of water and air.
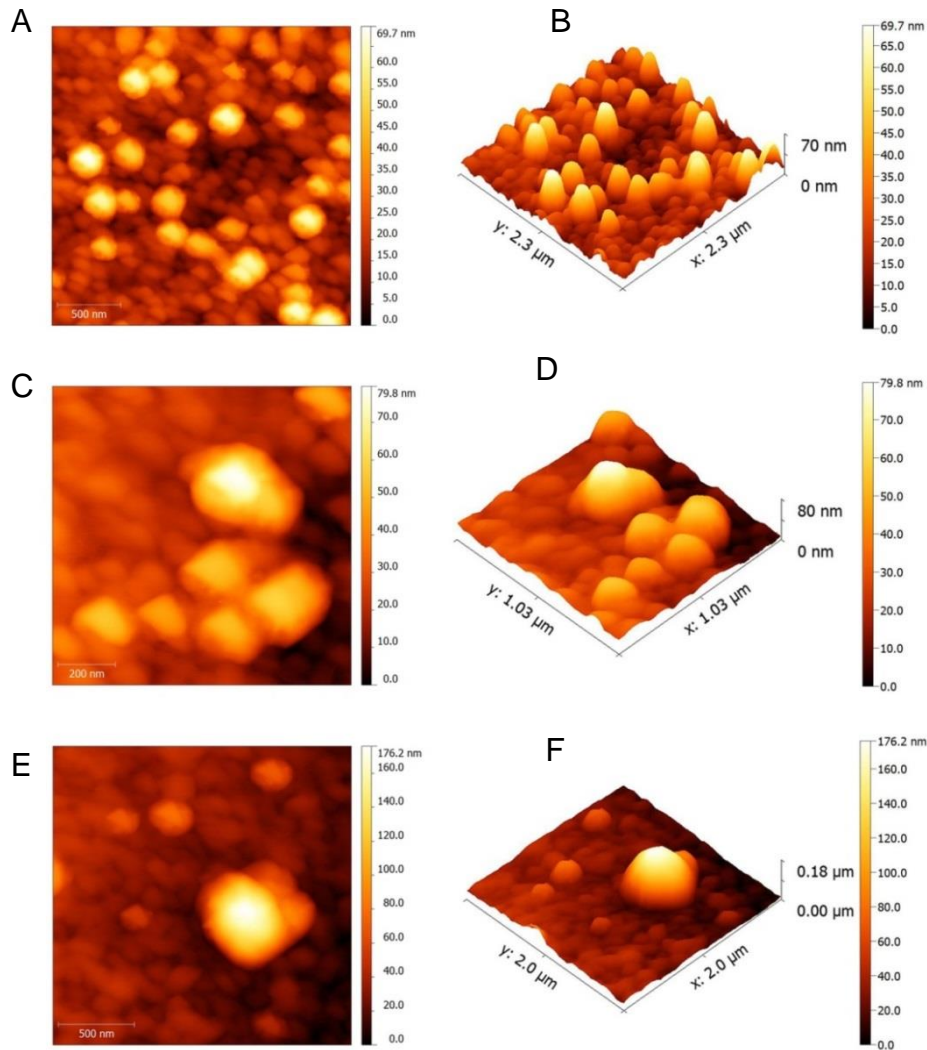
Figure 6. 7. Topographic AFM images of graphene bubbles on the mirror surface after laser irradiation (~3.8×10^{10} W/m^2). (A-B) 3D and 2D views of topographic AFM images showing many small graphene bubbles. (C-D) 3D and 2D views of topographic AFM images showing the merging of graphene bubbles. (E-F) 3D and 2D views of topographic AFM images showing single big graphene bubble.

After intense laser irradiation, AFM measurements were carried out within the same location and lots of graphene bubbles can be observed, as shown in Fig. 6.7. It was found that the formation of graphene bubbles depends a lot on the morphology of the mirror surface. Figure 6.7A and B show a lot of small graphene bubbles with the diameter of about 200 nm and height of 50 nm. It was found that most of these bubbles are lodged on triangle shape particles which have bright contrast in the AFM topographic image. If a few particles are close to each other, the laser induced graphene bubbles may merge together to form even larger bubble, as shown in Fig. 6.7C and D. Even larger graphene bubble with diameter > 500 nm and height of ~170 nm may form at certain circumstance where there is big particles and enough water and gas supply, as shown in Fig. 6.7E and F. Obviously the topographic images in Fig. 6.7 represent the nanobubbles at different growth stages.

A graphene bubble filled with liquid can also act as an adaptive focus lens due to relative larger refractive index inside compared with air outside.[27] Unlike planar graphene, the side wall of the curved graphene bubble provides larger interaction length with light. Considering the nonlinear Kerr effects in graphene, a graphene bubble acts as an adaptive nonlinear Kerr lens according to the finite-difference time-domain (FDTD) simulation shown in Fig 6.8A-E. In our simulations, a focused spot centered 643 nm below the graphene bubble (Fig. 6.8D) is already observable even though Kerr effect is not prominent at the power density of ~1×10^{10} W/m^2. This is not seen in planar graphene at the same power density (Fig. 6.8B). When the laser power is increased to ~5×10^{11} W/m^2, we find that such graphene bubble can focus light beam into a spot centered 615 nm below the mirror surface (Fig. 6.8E). The beam waist of the focal point is found to be reduced from ~500 nm (Fig. 6.8D) to ~400 nm (Fig.

6.8E). Such intensity-dependent self-focusing effect is a characteristic feature of adaptive Kerr lens. As a result, the phase change in graphene bubble is enhanced. Furthermore, the formation of graphene nanobubble uncouple the graphene film from mirror surface where the interaction with electromagnetic field could be very weak due to its position at the resonant node of the Fabry–Perot cavity.[28,29]
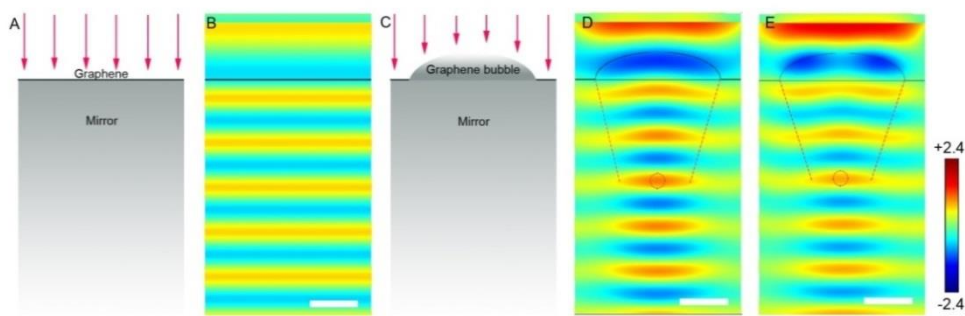
Figure 6. 8. Graphene nanobubble and adaptive Kerr lens. (A) Theoretical model of planar graphene on mirror substrate. The red arrows refer to plane light wave. (B) Simulated optical field of flat graphene on mirror substrate using FDTD (laser intensity: 1×10^{10} W/m^2). (C) Theoretical model of graphene nanobubble on mirror substrate. The red arrows refer to plane light wave. (D) Simulated optical field of graphene nanobubble showing self-focusing effect (under a laser intensity of 1×10^{10} W/m^2). (E) Simulated optical field on graphene nanobubble showing adaptive Kerr effect (under a laser intensity of 5×10^{11} W/m^2). Scale bars in B, D and E: 300 nm. Intensity scale of local field is shown on the right. The black lines represent graphene film and the region below refers to mirror substrate. The dashed lines in red indicate the focusing effect and the dashed circles in red show the center of focal points.

6.3.3 Tuning resonator spacing of the bistability

Figure 6.9A shows the bistability characteristic of the monolayer graphene as a function of the resonator spacing. When the resonators spacing (i.e., mirror separation) is tuned, the cavity is driven to a mode matched condition with the laser frequency. Meanwhile, the power inside the cavity is increased, which

forms the graphene nanobubbles and causes the enhancement of the nonlinearity effect of the graphene. As a result, the output versus input power curves illustrate different optical response ranging from limiting (at 0π), differential gain (at 0.8π), discriminator (narrow bistability at 0.83π), to bistability (at 0.87π, 0.93π and π).
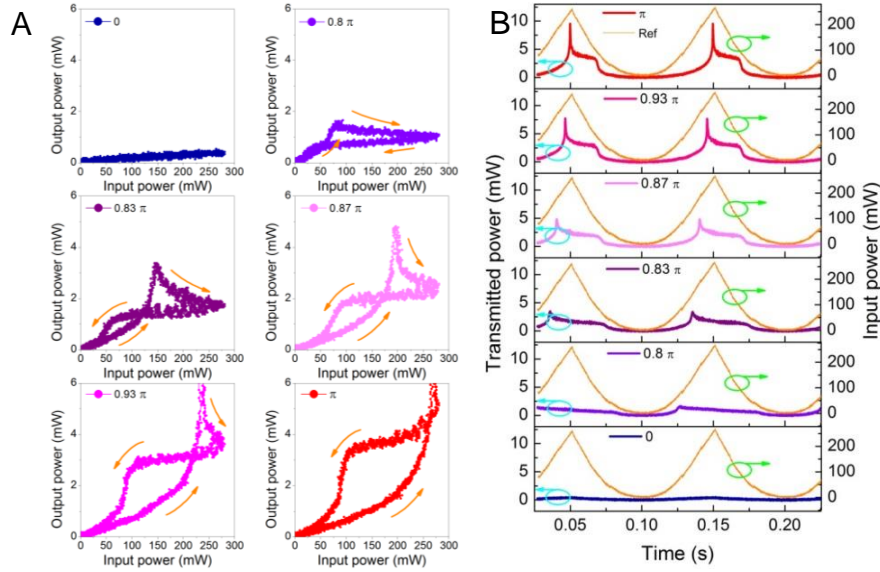
Figure 6. 9. Transmission characteristic's dependence on Fabry-Perot cavity detuning. (A) Optical bistable hysteresis loops as a function of resonator tuning. The cavity mistuning parameter β was controlled by changing the offset voltage of the piezo-spacer, i.e., the cavity length was increased continuously from phase at 0 to phase at π. (B) Time display of transmitted signal from the Fabry-Perot cavity in comparison with reference signal (orange color traces, right Y scale).

In order to clearly resolve the transmitted signal in comparison with the reference signal, the output trace versus time collected from photodiodes I and II in Fig. 6.1A are plotted in Fig. 6.9. It can be seen that the transmitted power increases very slowly in the beginning, and increases dramatically once the cavity is close to the resonant threshold, which thus leads to overshoot (as the maximum transmission point is not stable due to the requirement for the electric field to have a node at the mirror surface). The transmitted curves

obviously show asymmetrical shape while the incident signal shows a symmetrical ramping profile. We can see that the output power is suddenly turned on to achieve widest bistable hysteresis at phase π, which corresponds to $\lambda/2$ optical length change during resonance. Compared with recent report showing 0.18π phase change of terahertz wave by graphene, the phase change here is quite large due to the formation of bubble structure as well as amplification effect from the resonant cavity.[29]

It is worth noting the pronounced overshoot in the switch-on, which is an important characteristic of dispersive bistability. The output power at overshoot meets at the same input power for the empty cavity, indicating that the cavity is tuned to a highly transmitted status at the resonance. This feature of overshoot provides clues on the optical loss (e.g., unsaturable background and beam walk-off loss) in the cavity consisting of graphene. For example, the cavity has the highest loss at 0. When the resonator reaches the optimal condition at π, the overshoot becomes sharp and narrow, indicating the lowest optical loss in the cavity, which leads to increased trapping of the power in the cavity and results in the cavity overshoot. This overshoot appears at the high energy density range and enables the cavity to switch on because the transmission peak of the device will sweep through its maximum before settling into a lower self-consistent value.[30]

6.3.4 Response time of the bistability

The overshoot also indicates that the device exhibits fast switching dynamics with a response time which is shorter than the overshoot time.[30] We can estimate the cavity response time by directing a square wave into the cavity and monitoring the response time, as shown in Fig. 6.10A. It is clearly noticed that the appearance of overshoot depends on the detuning of the cavity. When the cavity approaches the mode-match condition, it is turned on and the overshoot becomes prominent. By single exponential fitting of the decay component, the cavity is determined to have a response time of around 40 ns (Figure 6.10B). This switching time is much faster than those of thermal optical bistability which are typically several to 100 ms.[17] However, the observed response time is a few orders of magnitude longer than that of the carrier relaxation time in graphene during saturable absorption which occurs in femtosecond range.[31,32]
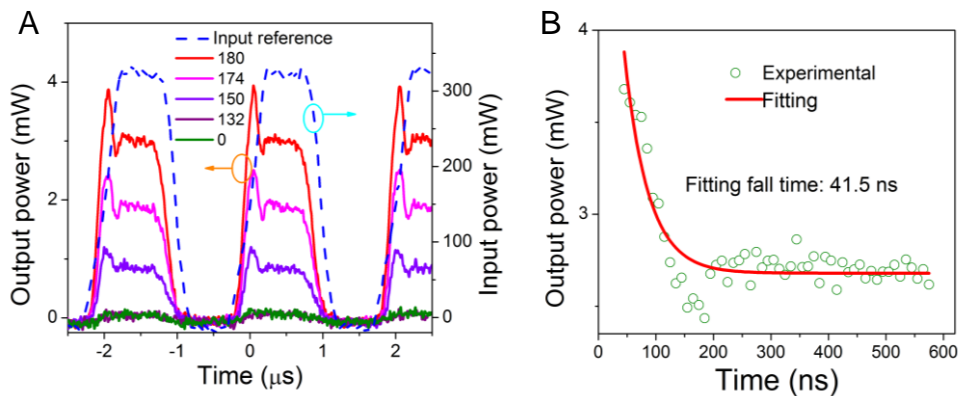
Figure 6. 10. The dynamics of Fabry-Perot cavity with graphene as a nonlinear refractive media. (A) The input square wave (blue dash trace) and output spectra at different cavity detuning. The frequency of the square wave is 500 kHz and input power is 0.33 W. (B) The experimental data and the fit to the fall time of the overshoot.

6.3.5 Dynamic trace of optical bistability

By setting a relatively low ramping frequency of acousto-optic modulator, the input power will change slowly so as to clearly observe the dynamic trace of the bistability hysteresis loop. Figure 6.11 shows the dynamic trace of the hysteresis loop of monolayer graphene in 9 seconds, in which the input power is shown on the x-axis and the output power is shown on the y-axis. As the input intensity increased, output power increased slowly at the early stage (from 1 s to 3 s), and then increased faster at the high input power range (from 4 s to 5 s) until turn on the Fabry-Perot interferometer. When the input power is decreased, the output power is firstly maintained at a high level for one second and then dropped quickly to the off state at the 7th second. Further decreasing the power (from 8 s to 9 s) will bring the interferometer back to the original state. As a result, we could resolve the dynamic trace of the hysteresis loop in one period and confirm the moving direction of the bistability.
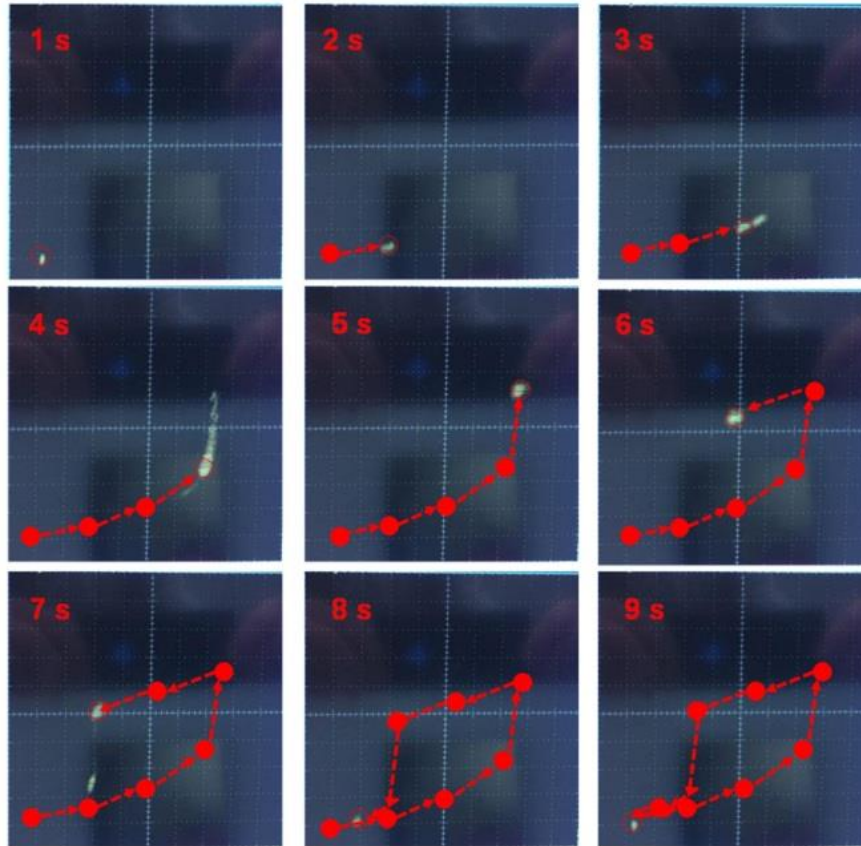
Figure 6. 11. Dynamic trace of the bistability hysteresis loop from 1s to 9s by setting the ramping frequency of acousto-optic modulator as 0.1 Hz.

6.3.6 Bistability of bilayer and multilayer graphene

In addition to the optical bistablility from monolayer graphene as discussed before, we have investigated the layer-dependent bistablility from bilayer and multilayer (~10 layers) graphene, as shown in Fig. 6.12 and 6.13. Both bilayer and multilayer graphene could give clear bistability loop, and the transmitted power decreases with the increasing of graphene layers. It is found that the bistability loop from bilayer graphene is much larger than that from multilayer graphene at resonance. This is because the multilayer graphene will cause larger light absorption as well as scattering loss, which leads to the lower

transmission of the cavity and furthermore limits the sharp switching between two optical states.
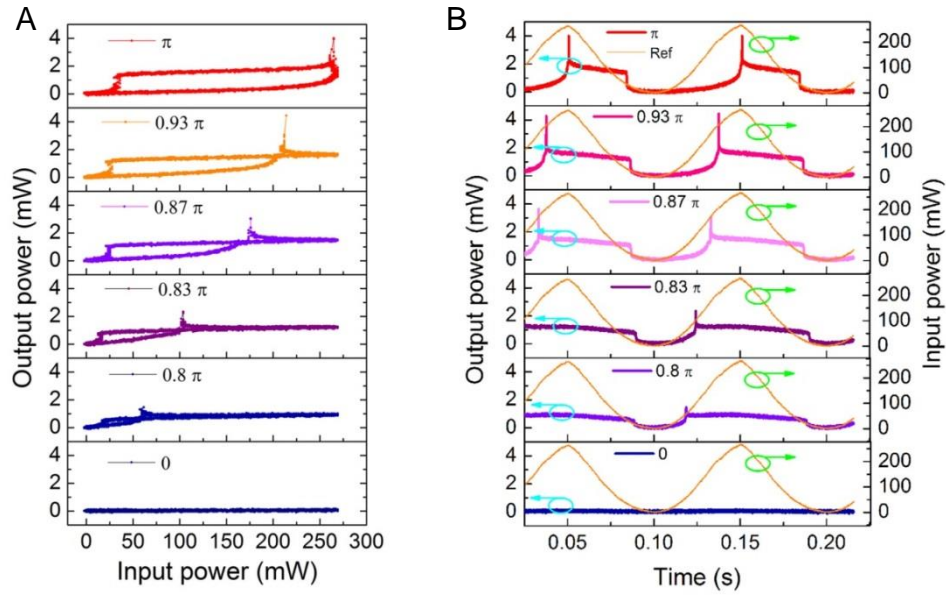
Figure 6. 12. Transmission characteristic's dependence on Fabry-Perot cavity detuning for the bilayer graphene. (A) Optical bistable hysteresis loops as a function of resonator tuning. The cavity mistuning parameter β was controlled by changing the offset voltage of the piezo-spacer, i.e., the cavity length was increased continuously from phase at 0 to phase at π. (B) Time display of transmitted signal from the Fabry-Perot cavity in comparison with reference signal (orange color traces, right Y scale).
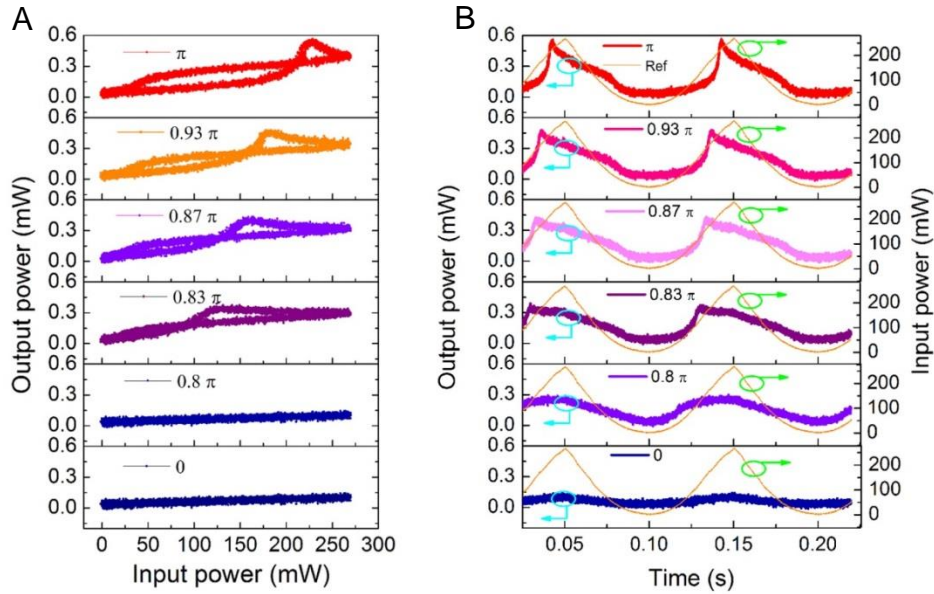
Figure 6. 13. Transmission characteristic's dependence on Fabry-Perot cavity detuning for the multilayer graphene (~10 layers). (A) Optical bistable hysteresis loops as a function of resonator tuning. The cavity mistuning parameter β was controlled by changing the offset voltage of the piezo-spacer, i.e., the cavity length was increased continuously from phase at 0 to phase at π. (B) Time display of transmitted signal from the Fabry-Perot cavity in comparison with reference signal (orange color traces, right Y scale).

6.3.7 Power dependent of bistability

Figure 6.14 shows the power dependent bistability of the monolayer and bilayer graphene. It is interesting to note that turn-on and turn-off power are independent of incident light intensity. Only the tail increase with increase incident light intensity. As shown before, cavity turn-on power could be controlled by tuning the cavity length. This interesting behavior indicates that with proper cavity length alignment optical bistability could be achieved, even with lower input power. Meanwhile, a larger bistability hysteresis loop could be obtained at the high power input, which may be useful for applications.
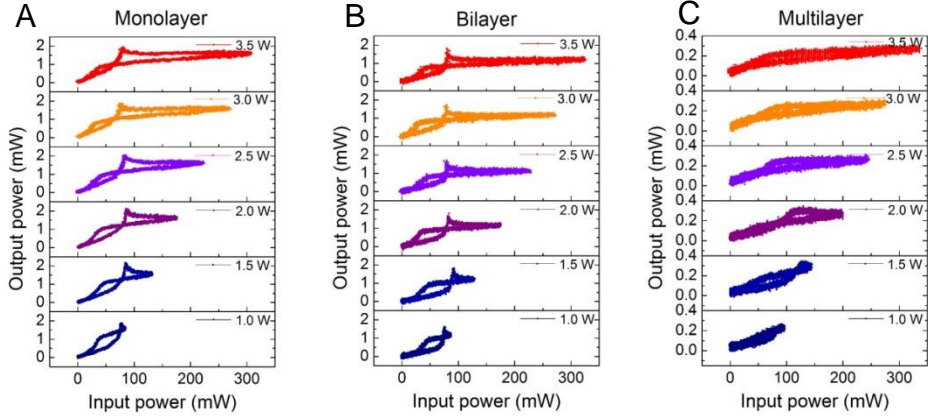
Figure 6. 14. Power dependent bistability of the monolayer, bilayer and multilayer (~10 layers) graphene. The laser power is tuned from 1 W to 3.5 W. The input power at X-axis represents the real incident power which is directed into Fabry-Perot cavity.

6.3.8 Simulation of the bistability

According to the configuration of our bistable device, the boundary conditions can be written as,

$$E_T = \sqrt{T} E_F (L) \tag{6.3}$$

$$E_F (0) = \sqrt{T} E_I + R\, e^{2iKL} e^{-\alpha d} E_F (0) \tag{6.4}$$

Where T is the transmittance, L is the length of the Fabry-Perot cavity, α is the intensity-dependent absorption coefficient, E_I, E_R, E_F, E_B, E_T are the incident, reflected, forward, backward, and transmitted electric field slowly varying complex amplitudes, respectively (Fig. 6.15). As such, we assume that the absorption coefficient depends only on the "uniform field" approximation (field envelope is position independent) and thereby neglect saturation or nonlinear index corrections due to field changes along the laser axis.
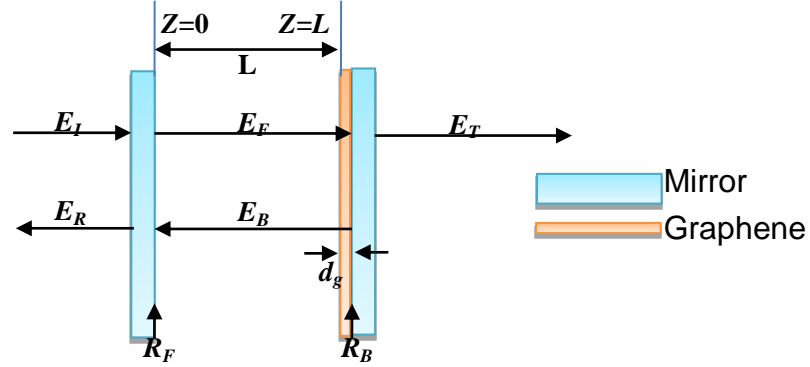
Figure 6. 15. Schematic model of the Fabry-Perot interferometer. E_I, E_R, E_B and E_T are the incident, reflected, forward, backward and transmitted electric fields, respectively. R_F and R_B refer to the reflectivity of the front and back mirror. d_g refers to the thickness of graphene film and L refers to the cavity length.

The field E_T is simply related to E_F :

$$E_T = \sqrt{T} E_F(L) = \sqrt{T} e^{-\alpha d} e^{2iK\ell} E_F(0) \qquad (6.5)$$

Where, $\ell = K - d$. Combining this with Equation (6.5), we have the amplitude transmission function

$$\frac{E_T}{E_I} = \frac{T e^{2iK(\ell - L)}}{e^{\alpha d - 2iKL} - R} \qquad (6.6)$$

Up to this point, our equations apply to an arbitrary complex absorption coefficient, α and hence can be used to study both purely dispersive and purely absorptive optical bistability.

For absorptive bistability, the intensity transmission function is simplified as:

$$\frac{I_I}{T} = \frac{I_T}{T} \left[1 + \frac{\alpha_0 d / T}{1 + I_T / T} \right]^2 \qquad (6.7)$$

130

For purely dispersive case, we approximately assume $[\mathrm{Re}(\alpha) = 0]$. By setting $\beta = \text{nearest multiple of } (2\pi) - 2KL$, β is the cavity-laser phase detuning, we find that the amplitude transmission function (6.6) yields

$$\frac{E_T}{E_I} = \frac{Te^{2i K(\ell -)L}}{e^{i\beta} - R} \tag{6.8}$$

The intensity transmission function is

$$\frac{I_T}{I_I} = \frac{T^2}{\left| e^{i\beta} - R \right|^2} = \frac{1}{1 + 4R \sin^2(\beta/2)/T^2} \tag{6.9}$$

Where, $I_T = \left| E_T \right|^2$, $I_I = \left| E_I \right|^2$ (here we suppose the E's are dimensionless fields corresponding to the usual dimensionless intensity definition). At a cavity resonance, which gives

$$\frac{I_T}{I_I} = \frac{T^2}{\left| e^{-i\beta} - R \right|} = \frac{1}{1 + R\beta^2/T^2} \tag{6.10}$$

To understand dispersive bistability, we expand the phase shift β as,

$$\beta = \beta_0 + \beta_2 I_T \tag{6.11}$$

Combining equation (6.9) and (6.11), we can simulate and plot the curve of the optical bistability.

In order to further understand the bistable mechanism, we proposed a simplified theoretical model to verify the bistable hysteresis. As mentioned before, the condition for purely absorptive bistability is $\alpha d / (T + \alpha_B d) > 8$, where α is the absorption coefficient, α_B is the unsaturable background

131

absorption coefficient, *d* is the thickness of absorptive medium, and *T* is transmittance. The thickness of the graphene is too small to fulfill the requirement for purely absorptive bistability. For the absorptive bistability, the switch-down intensity is independent of transmittance whereas the switch-up intensity is inversely related to transmittance. However, this is not the case if we look into the experimental results shown in Fig. 6.16. For monolayer graphene, the turn-on power density of 2.7×10^{11} W/m^2 is much larger than the saturation intensity of 1.3×10^9 W/m^2, indicating an over-saturated status in graphene.

Summarizing above experimental observations, we point out that optical dispersive bistability is the dominant regime as the contribution from absorptive effect is negligibly small. By taking nonlinear dispersion into account, the simulation can qualitatively reproduce the bistable hysteresis in our experiments, as shown in Fig. 6.16B. We performed control experiments on monolayer, bilayer and compared with theoretical calculations. Striking differences in hysteresis between monolayer graphene and bilayer are observed, which are mainly caused by different phase shifts, $\beta = \beta_0 + \beta_2 I_T$, where β_0 contains all intensity-independent phase shifts and β_2 arises from a nonlinear refractive index, $n = n_0 + n_2 I_T$. As it is known that the change of nonlinear refractive index in graphene is nearly proportional to the number of graphene layers, we can expect larger phase shift in bilayer graphene which also leads to a lower switch-on threshold and half maximum output power density compared with the monolayer graphene. It is also noticed that the overshoot for bilayer graphene is also lower than that of monolayer graphene. This is because the monolayer graphene has larger transmittance (lower

132

absorption) compared with bilayer graphene. The Fabry-Perot cavity with monolayer graphene can maintain a higher power inside the cavity, leading to a higher overshoot.
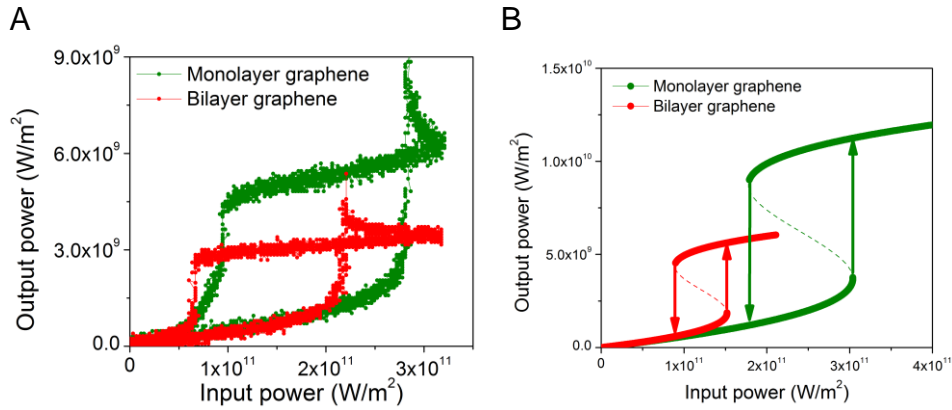
Figure 6. 16. (A) Experimental hysteresis measured from monolayer and bilayer graphene. (B) Calculated optical bistability curves for monolayer and bilayer graphene.

6.4 Conclusions

In conclusion, the exotic optical properties of graphene can lead to strong nonlinear light-matter interaction. The graphene bubbles allow a longer path length for the non-linear dispersive interactions compared to monolayer graphene, which changes the optical phase by π and produces an optical length change ($\lambda/2$). Graphene optical bistable devices appear to be particularly promising because of giant optical nonlinearities and small thickness permitting the construction of miniaturized devices. They may find important applications in optical logic, memories, and analog-to-digital converters in optical signal processing systems. In addition, they can also be used as optical pulse discriminators and optical power limiters.

Bibliograph

1. Q. Bao, H. Zhang, Y. Wang, Z. Ni, Y. Yan, Z. X. Shen, K. P. Loh and D. Y. Tang, "Atomic‑Layer Graphene as a Saturable Absorber for Ultrafast Pulsed Lasers," Advanced Functional Materials 19, 3077-3083 (2009).

2. Z. Sun, T. Hasan, F. Torrisi, D. Popa, G. Privitera, F. Wang, F. Bonaccorso, D. M. Basko and A. C. Ferrari, "Graphene mode-locked ultrafast laser," ACS Nano 4, 803-810 (2010).

3. E. Hendry, P. Hale, J. Moger, A. Savchenko and S. Mikhailov, "Coherent nonlinear optical response of graphene," Phys. Rev. Lett 105, 097401 (2010).

4. H. Zhang, S. Virally, Q. Bao, L. Kian Ping, S. Massar, N. Godbout and P. Kockaert, "Z-scan measurement of the nonlinear refractive index of graphene," Optics Letters 37, 1856-1858 (2012).

5. Novoselov, K.S. et al. "A roadmap for graphene," Nature 490, 192-200 (2012).

6. Bonaccorso, F., Sun, Z., Hasan, T. and Ferrari. A, "Graphene photonics and optoelectronics," Nature Photonics 4, 611-622 (2010).

7. Bao, Q.L. and Loh, K.P, "Graphene Photonics, Plasmonics, and Broadband Optoelectronic Devices," Acs Nano 6, 3677-3694 (2012).

8. Avouris, P, "Graphene: Electronic and Photonic Properties and Devices," Nano Lett. 10, 4285-4294 (2010).

9. Xia, F., Mueller, T., Lin, Y., Valdes-Garcia, A. & Avouris, P. "Ultrafast graphene photodetector," Nature Nanotechnology 4, 839-843 (2009).

10. Liu, M. et al. "A graphene-based broadband optical modulator," Nature 474, 64-67 (2011).

11. Bao, Q. et al. "Broadband graphene polarizer," Nature Photonics 5, 411-415 (2011).

12. Lim, G.-K. et al. "Giant broadband nonlinear optical absorption response in dispersed graphene single sheets," Nature Photonics 5, 554-560 (2011).

13. Loh, K.P., Bao, Q., Eda, G. & Chhowalla, M. "Graphene oxide as a chemically tunable platform for optical applications," Nat. Chem. 2, 1015-1024 (2010).

14. Gu, T. et al. "Regenerative oscillation and four-wave mixing in graphene optoelectronics," Nature Photonics 6, 554-559 (2012).

15. Smith, S. "Lasers, nonlinear optics and optical computers," Nature 316, 319-324 (1985).

16. Abraham, E. and Smith, S.D. "Optical bistability and related devices," Rep. Prog. Phys. 45, 815-885 (1982).

17. Gibbs, H. "Optical bistability: Controlling light with light," Vol. 1. (Academic Press, Inc., Orlando, Florida; 1985).

18. Gibbs, H., McCall, S. and Venkatesan, T. "Differential gain and bistability using a sodium-filled Fabry-Perot interferometer," Phys. Rev. Lett. 36, 1135-1138 (1976).

19. Miller, D., Smith, S. and Johnston, A. "Optical bistability and signal amplification in a semiconductor crystal: applications of new low‐power nonlinear effects in InSb," Appl. Phys. Lett. 35, 658-660 (1979).

20. Gibbs, H.M. et al. "Optical bistability in semiconductors," Appl. Phys. Lett. 35, 451-453 (1979).

21. Gibbs, H.M. et al. "Room-temperature excitonic optical bistability in a GaAs-GaAlAs superlattice etalon," Appl. Phys. Lett. 41, 221-222 (1982).

22. Szoke, A., Daneu, V., Goldhar, J. and Kurnit, N. "Bistable optical element and its applications," Appl. Phys. Lett. 15, 376-379 (1969).

23. Wang, F. et al. "Gate-variable optical transitions in graphene," Science 320, 206-209 (2008).

24. Ferrari, A. C. and D. M. Basko, "Raman spectroscopy as a versatile tool for studying the properties of graphene," Nat. Nanotech. 8, 235 (2013).

25. Ferrari, A. C., J. C. Meyer, et al. "Raman spectrum of graphene and graphene layers," Phys. Rev. Lett. 97, 187401 (2006).

26. Zabel, J., R. R. Nair, et al. "Raman Spectroscopy of Graphene and Bilayer under Biaxial Strain: Bubbles and Balloons," Nano Lett. 12, 617 (2012).

27. Georgiou, T., L. Britnell, et al. "Graphene bubbles with controllable curvature," Appl. Phys. Lett. 99,   (2011).

28. Ferreira, A., N. M. R. Peres, et al. "Graphene-based photodetector with two cavities," Phys. Rev. B 85, 115438 (2012).

29. Lee, S.H. et al. "Switching terahertz waves with gate-controlled active graphene metamaterials," Nature materials 11, 936-941 (2012).

30. Venkatesan, T.N.C., Vol. Ph.D (City University of New York, 1977).

31. George, P.A. et al. "Ultrafast optical-pump terahertz-probe spectroscopy of the carrier relaxation and recombination dynamics in epitaxial graphene," Nano Lett. 8, 4248-4251 (2008).

32. Bao, Q. et al. "Monolayer graphene as a saturable absorber in a mode-locked laser," Nano Research 4, 297-307 (2011).

Chapter 7 Summary and Future Work

7.1 Summary

7.1.1 Defect dynamics and spectral splitting in single crystalline LAO

PL and ultrafast dynamics of LAO crystal has been studied in this thesis. Three defect luminescence levels have been observed in the temperature dependent PL spectrum of the LAO single crystal. The broad spectrum center at 600 nm was likely due to the electronic transition from singly charged oxygen interstitial defect levels to valence band; the two sharp peaks centered at 699 and 726 nm peak were likely due to La interstitial and/or the Al antisite at the La position to the valence band. The PL spectrum showed doublet splitting of roughly 6 nm. An Al displacement of 0.09 Å in a sublattice, which is possible because of twinning, is adequate to explain the spectral splitting.

The femtosecond TA experiments showed two induced absorption peaks. The TA bands at 620 nm under high excitation intensity decay with two different time scales: a fast decay with a time constant of 4 ps followed by a slow decay with time constant over 1 ns. However, the TA band at 760 nm only showed one slow decay component. We think the fast decay is due to the induced excited electron absorption from the higher defect levels to conduction band, while the slow decay process is due to the electron absorption from the lower two defect levels to the upper defect level just below the conduction band.

7.1.2 Fine structure of defect states in STO

Multi-photon room temperature luminescence of STO was observed using 800 nm femtosecond laser irradiation. The power dependent PL showed a slope of

2.7, which suggested that a three photon process contributed to the PL. It was noted that the 350 nm above band gap excitation PL also had the same spectrum as the 800 nm multi-photon excitation, which is consistent with the observation of slow decay process for the 350 nm and 800 nm excitation TA. The PL signal in both cases had the same excited and ground states.

A number of defect levels in STO were resolved by femtosecond TA studies using 400 nm sub-band gap excitation. Five deep defect levels within the band gap showed a short lifetime (< 2 ps), suggested that these defect levels may originate from the same atomic entity. After the fast decay, these energy levels coalesced into two prominent trap levels centered at 1.1 and 1.55 eV above the valence band.

7.1.3 Defect Electron Dynamics in TiO_2

TA of the TiO_2 single crystal, polycrystalline TiO_2 films (with different oxygen vacancy) and epitaxial films of Ta-TiO_2 (with different Ta concentration) have been studied. Only a slow decay process with a lifetime of a few ns was observed in the single crystal TiO_2. The TiO_2 films deposited on the Quartz substrate with different oxygen deposition pressure showed faster single exponential decay of about 300 to 180 ps. It was noted that carrier decay lifetime decreased with oxygen vacancy. Defect level in the Ta doped TiO_2 was studied using the 350 nm femtosecond TA experiment. The TA spectrum arose from the induced excited electron absorption. It was observed that the excited carrier lifetime decreased with Ta concentration. The TA spectrum showed the blue-shift of the induced absorption peak, which was consistent with the UV spectrum in which the band gap increased with the Ta concentration. The Ta substitution led to the reconstruction of the band

structure, which may have helped to increase carrier recombination time. For the long recombination lifetime of the pure anatase film, this may be due to the long lifetime of surface trap states.

Less defect and longer lifetime carriers in the low oxygen vacancy TiO_2 film helped improve the photodegradation efficiency. Both the band-edge and above band gap irradiation showed that low oxygen vacancy TiO_2 films had higher degradation efficiency.

7.1.4 Bistability of graphene

The large nonlinear Kerr effect observed in graphene has great potential for nonlinear optical device applications. In this thesis, we have observed the bistability hysteresis loops of graphene inside a Fabry- Perot interferometer. By tuning the cavity, we have successfully controlled the cavity to the "on" or "off" state. In addition, this bistability had a very fast switching speed of 40 ns. The graphene formed nanobubbles after the high-intensity laser irradiation, which was demonstrated using Raman mapping and AFM imaging. The graphene nano-bubbles increased optical pass length, which helped drive the cavity to the resonance mode match condition, and hence enabled optical bistability in monolayer graphene. This graphene optical bistability may have important applications as optical logic, memories, and analog-to-digital converters in optical signal processing systems.

7.2 Future Works

In this thesis, it was shown that ultrafast spectroscopy is very important for studying the carrier dynamics and nonlinear optical properties of semiconductor oxide materials, as well as the 2D graphene system. Carrier dynamics and the nonlinear optical properties of the materials have been

studied. Although a rich defect and optical nonlinearity picture has evolved further efforts are still required to clearly understand the whole picture. Below are some suggested projects for further investigation:

1. *Temperature dependent carrier dynamics of the LAO.* As shown in our results, broad and sharp PL peaks behaved quite differently with increase in temperature. Broad emission decreased with increases in temperature, and the two sharp emission increased with temperature. At this stage, the mechanism behind this process is still unclear. Temperature-dependent TA may help further investigate the mechanisms behind this interesting behavior.

2. *Temperature dependent multiphoton photoluminescence and carrier dynamics in the STO.* It is known that STO has broad green emission of only 2.4 eV at low temperatures. As shown in Chapter 4 where room temperature multi-photon and one-photon excitation PL had only blue emission centered at 2.8 eV, where the green emission is not observed in our experiment. As temperature was reduced, PL increased and green emission was established, so it would be very interesting to study the behavior of green emission with the multi-photon excitation process. Meanwhile, with the TA spectroscopy the carrier dynamics of the fast decay and the slow decay process could be studied in more detail.

3. *Nonlinear optical properties of Ta substituted TiO_2.* As shown in our results, Ta substitution affected the blue shift of the UV-vis transmission spectrum and the TA spectrum. As the band gap increased to the UV range, it was enlightening to study the nonlinear optical properties, such as multi photon absorption and multi photon excitation PL. It would be interesting

to have wide band gap metallic materials with strong nonlinear optical properties.

4. *Bistability for the doped graphene and other 2D materials (MoS2, WS2, topological insulators).* As the nonlinear optical properties of the graphene can be easily tuned by the doping process, in this case the lower saturable intensity and large nonlinear effect can be obtained to further reduce the light intensity of the bistability threshold. This optical bistability experiment may also apply for other 2D materials, such as MoS_2, WS_2, and topological insulators.